MICROSEISMIC INVERSION FOR ANISOTROPIC VELOCITY MODEL IN UNCONVENTIONAL RESERVOIRS

DISSERTATION

zur Erlangung des Grades eines

DOKTORS DER NATURWISSENSCHAFTEN

am Fachbereich Geowissenschaften
der Freien Universität Berlin

vorgelegt von

Changpeng Yu

Berlin, May 2016

EHRENWÖRTLIHE ERKLÄRUNG:

Ich erkläre hiermit an Eides statt, dass ich die vorliegende Dissertation selbstständig und nur unter Verwendung der angegebenen Quellen und Hilfsmittel angefertigt habe.

Berlin, den 23.05.2013

Referent:	Prof. Dr. Serge A. Shapiro
Korreferent:	Prof. Dr. Marco Bohnhoff
Date of Disputation:	15 July 2016

Freie Universität Berlin
Fachbereich Geowissenschaften
Institut für Geologische Wissenschaften
Malteserstr. 74 - 100
12249 Berlin

Summary

The main objective of this thesis is to develop a practical, geology- and rock physics-oriented approach to constructing anisotropic velocity model for unconventional reservoirs using downhole microseismic datasets. The working procedure of the approach starts by addressing the geological sources of anisotropy. A priori knowledge of anisotropy is obtained by integrating geological information and rock physics studies. The prior knowledge serves as constraint on the microseismic inversion. The anisotropic velocity model obtained by the approach can reflect the heterogeneity of anisotropic parameters and cover the anisotropic symmetries of most importance in seismic exploration and reservoir characterization. The optimal anisotropic velocity model not only minimizes the data misfit, but also is reasonable from the perspectives of geology and rock physics. The results derived from downhole microseismic dataset are comparable with laboratory experiments. This demonstrates that the downhole microseismic monitoring, as a quasi in-situ experiment, has a potential to contribute to a better understanding of subsurface anisotropy beyond the laboratory.

The approach developed in this thesis uses a layered velocity model. This approximation is adequate due to the limited spatial range of microseismic monitoring and the relatively flat sedimentary background of unconventional reservoirs. The transverse isotropy caused by the bedding-parallel fabric is defined by Thomsen parameters in each layer. The lateral heterogeneities within each layer are dismissed, while the vertical gradients of transverse isotropic parameters are kept. The fracture-induced anisotropy is only defined in a specific layer of high brittleness and is characterized by normal and tangential fracture compliance. The approach uses the arrival-time of seismic waves recorded by sensor arrays. An anisotropic ray-tracing algorithm is modified to calculate the synthesized travel-time. Parallel computing is employed to accelerate the ray-tracing program. The inherent singularity problems in the ray-tracing method are fixed by applying numerical strategies. Two nonlinear inversion methods are involved in this approach to determine different components of anisotropy velocity model. The multi-layer TI model is inverted by an iterative gradient-based optimization (the Gauss-Newton method). The fracture-induced anisotropy represented only by two parameters is obtained by a global search method. Besides, as a possible source of uncertainties in the velocity model inversion and event locations, the issues of computing triggering time (T_0) are analyzed theoretically and illustrated with

examples. The approach developed in this study is partially applied to a completed project of downhole microseismic monitoring in a coalbed methane reservoir to verify the capability of iterative gradient-based inversion for anisotropic velocity model and illustrate the T_0 issue in the configuration of limited aperture. Then, the approach is fully applied to a downhole microseismic dataset from Horn River Basin in Canada to investigate the fabric anisotropy and fracture-induced anisotropy of shales.

The fabric anisotropy of shale is caused by the alignment and lamination of the low-aspect-ratio, compliant particles, such as clay minerals and organic matter. The existence of quartz minerals can prevent and interrupt such alignment and lamination and consequently weaken the fabric anisotropy of shale. Laboratory measurements show a strong positive correlation between the degree of fabric anisotropy and the volume contents of clay minerals and kerogen. Thomsen parameters ε and γ of shale samples are well correlated with each other, but not with δ. By integrating the geological information and experimental studies, the fabric anisotropy of Horn River shales is initially estimated. The quartz-rich shale gas reservoir is expected to show much weaker transverse isotropy than the overlying clay-rich shale. An iterative optimization using the gradient-based method is then implemented on this initial model. The results derived from the downhole microseismic dataset are consistent with the laboratory measurements. The optimized VTI model reduces the time misfit by about 65% compared to the originally provided VTI model. The event locations are also significantly improved.

The preferred-oriented fracture set is another important source of shale anisotropy. Mechanical analyses show that the fractures in Horn River shales mainly occur in the quartz-rich formation showing much higher brittleness. According to the core analyses and fracture mechanism, the fracture planes are commonly perpendicular to the bedding plane and the dominant fracture set strikes to NE-SW direction which is parallel to the current maximum horizontal stress. The elastic behaviors of the fracture are effectively described by the normal and tangential fracture compliance (i.e., Z_N, Z_T) regardless of any physical details of fracture. Theoretical modeling and experimental measurements show, the magnitudes of Z_N and Z_T increase with the fracture dimension scale, and the Z_N/Z_T ratio is sensitive to fluid fills and has the value less than or slightly larger than 1. These facts are used as physical constraints in the grid search for the optimal fracture compliance. The magnitudes of Z_N and Z_T define the searching range and the Z_N/Z_T ratio is used as a quality control. The optimal Z_N and Z_T have the same order of magnitude as other measurements in the crosshole and microseismic scale. The Z_N/Z_T ratio corresponds to the extreme cases of dry or gas saturated fractures.

Zusammenfassung

Das Hauptziel dieser Arbeit ist die Entwicklung eines praktischen Verfahrens zur Erstellung anisotroper Geschwindigkeitsmodelle aus mikroseismischen Bohrlochdatensätzen in unkonventionellen Kohlenwasserstofflagerstätten unter Einbindung geologischer und gesteinsphysikalischer Aspekte. Der Arbeitsablauf des Verfahrens beginnt mit der Vorstellung geologischer Ursachen von Anisotropie. Apriorische Kenntnisse über Anisotropie stammen aus der Integration geologischer Informationen und gesteinsphysikalischer Studien, welche als Randbedingungen der mikroseismischen Inversion dienen. Mit dem präsentierten Verfahren gewonnene Geschwindigkeitsmodelle können Heterogenitäten anisotroper Parameter wiedergeben und decken die wichtigsten anisotropen Symmetrien in den Bereichen der seismischen Exploration und Reservoir-Charakterisierung ab. Das optimale anisotrope Geschwindigkeitsmodell verringert dabei nicht nur die Laufzeitresiduen, sondern ermöglicht auch eine bessere Beschreibung der geologischen und gesteinsphysikalischen Vorgaben. Der Vergleich mit Hilfe von Bohrlochdaten erzielter Ergebnisse gegenüber Laboruntersuchungen zeigt, dass direkt im Bohrloch durchgeführte mikroseismischen Beobachtungen als gewissermaßen In-situ-Experiment zu einem besseren Verständnis der Anisotropie im Untergrund genutzt werden können.

Das präsentierte Verfahren nutzt ein geschichtetes Geschwindigkeitsmodell unter Berücksichtigung der Einschränkungen mikroseismischen Bohrloch-Monitorings und des sedimentären Charakters unkonventioneller Lagerstätten. Die durch ein schichtungsparalleles Gefüge verursachte transversale Isotropie (TI) einer jeden Schicht wird durch Thomsen-Parameter beschrieben. Laterale Heterogenitäten innerhalb einzelner Schichten werden vernachlässigt, wohingegen der vertikale Gradient der TI-Parameter erhalten bleibt. Bruchinduzierte Anisotropie wird nur in Schichten mit einer hohen Brüchigkeit definiert und als Kombination aus normalen und tangentialen Nachgiebigkeiten charakterisiert. Das Verfahren basiert auf der Registrierung von Ankunftszeiten seismischer Wellen. Ein durch parallele Berechnungen beschleunigter anisotroper Raytracing-Algorithmus wird zur Bestimmung der synthetischen Laufzeiten verwendet, wobei inhärente Singularitätsprobleme durch die Anwendung numerischer Strategien behoben werden. Im Rahmen dieser Arbeit werden zwei nichtlineare Inversionsmethoden zur Bestimmung der unterschiedlichen Komponenten des anisotropen Geschwindigkeitsmodells genutzt. Das mehrschichtige TI-Modell wird mit

Hilfe des iterativen gradientenbasierten Gauss-Newton-Verfahrens invertiert. Die von nur zwei Parametern beschriebene bruchinduzierte Anisotropie wird durch eine globale Suche bestimmt. Probleme bei der Berechnung von Herdzeiten (T_0) werden theoretisch betrachtet und anhand von Beispielen erklärt, weil die herkömmliche Berechnungsmethode eine mögliche Fehlerquelle für Ungenauigkeiten im Geschwindigkeitsmodell und bei der Mikrobebenlokalisierung darstellt. Das vorgeschlagene Verfahren wird teilweise an einem abgeschlossenen Projekt für mikroseismisches Bohrloch-Monitoring in einer Flözgas-Lagerstätte ausprobiert, um die Möglichkeiten der iterativen gradientenbasierten Inversion zu erörtern und Probleme der Bestimmung von T_0 in limitierten Datenvolumina zu verdeutlichen. Anschließend wird das Verfahren im vollen Umfang an einem mikroseismischen Datensatz einer Schiefergaslagerstätte im Horn-River-Becken getestet, um im Besonderen die Gefügeanisotropie als auch eine durch Brüche induzierte Anisotropie in Schiefergesteinen zu untersuchen.

Gefügeanisotropie in Schiefern wird durch die einheitliche Ausrichtung und Laminierung fester länglicher Partikel wie Tonminerale oder organischen Materials erzeugt. Ein zusätzlicher Quarz-Anteil kann jedoch die Ausrichtung und Laminierung der Partikel beeinträchtigen und somit die Gefügeanisotropie der Schiefer signifikant verringern. Laborexperimente zeigen eine starke positive Korrelation zwischen der Ausprägung der Gefügeanisotropie sowie den Ton- und Kerogen-Anteilen. Außerdem korrelieren die Thomsen-Parameter ε und γ sehr gut untereinander aber nicht mit δ. Die Ausgangswerte der Gefügeanisotropie der Horn-River-Schiefer werden durch Integration geologischer Informationen und experimenteller Studien abgeschätzt. Die quarzreichen gashaltigen Schichten sollten eine deutlich schwächere transversale Isotropie als die tonhaltigen Schiefer im Hangenden zeigen. Die mit Hilfe der iterativen Optimierung aus mikroseismischen Bohrlochdaten bestimmte Gefügeanisotropie entspricht dabei Ergebnissen von Labormessungen. Das optimierte VTI-Modell reduziert die Laufzeitresiduen um rund 65% im Vergleich zum ursprünglichen zur Verfügung gestellten anisotropen Geschwindigkeitsmodell. Zudem konnten die Mikrobeben mit dem optimierten VTI-Modell signifikant besser lokalisiert werden.

Eine weitere wichtige Ursache von Anisotropie in Schiefern stellt ein System von Brüchen bevorzugter Orientierung dar. Mechanische Analysen von Brüchen in Schiefergesteinen aus dem Horn-River-Becken zeigen, dass diese vorwiegend in quartzreichen Formationen mit einer sehr hohen Brüchigkeit auftreten. Anhand der Analyse von Bohrlochkernen und Bruchmechanismen wird angenommen, dass die Bruchfläche normal zur Schichtung des Gefüges der Schiefer orientiert ist. Das dominante System von Brüchen zeigt ein Streichen in NO-SW-Richtung und verläuft somit parallel zur derzeitigen maximalen horizontalen Spannung. Das elastische Verhalten von Brüchen wird durch normale und tangentiale Nachgiebigkeiten (Z_N, Z_T) unabhängig von der genauen Bruchmorphologie beschrieben. Theoretische Modellierungen und Messungen verdeutlichen, dass die Magnituden von Z_N und Z_T mit der Größe der Bruchfläche steigen und dass das Verhältnis zwischen normaler zu tangentialer Nach-

giebigkeit Z_N/Z_T kleiner oder minimal größer 1 ist sowie sensitiv auf Fluidfüllungen reagiert. Zur Bestimmung der optimalen Werte für Z_N und Z_T wird eine Rastersuche durchgeführt, wobei die getätigten Beobachtungen als physikalische Randbedingungen zur Abschätzung der Nachgiebigkeiten genutzt werden, um durch Angaben zur Magnitude den Suchraum einzuschränken und Z_N/Z_T zur Qualitätskontrolle zu nutzen. Die ermittelten Werte für Z_N und Z_T bewegen sich in derselben Größenordnung wie bei anderen mikroseismischen Bohrlochuntersuchungen. Z_N/Z_T entspricht den extremen Fällen trockener oder mit Gas saturierter Brüche.

Contents

Chapter 1

Introduction

1.1 Motivation

This thesis is motivated by the reports in recent years concerning the influences of anisotropy on microseismic data processing and interpretations. An accurate anisotropic velocity model is the key to eliminating these negative influences. However, the conventional approaches to building velocity model for microseismic monitoring are not designed to be sophisticated enough to precisely determine the inhomogeneous anisotropy. Sonic logs are still the primary source from which Vp and Vs can be obtained. Then calibrations by perforation shots are usually performed to correct the overestimation of velocities in sonic frequency range. An isotropic velocity model or roughly estimated background anisotropy is commonly used. The only criterion when assessing the obtained velocity model is the time misfits of seismic arrivals. Geology and rock physics are not extensively integrated into the velocity model building as is commonly done in reflection seismic applications.

This thesis aims to develop a practical, geology- and rock physics-oriented approach to constructing anisotropic velocity model for downhole microseismic monitoring in unconventional reservoirs. The anisotropic velocity model obtained by this approach should be able to reflect the heterogeneity of anisotropic parameters and cover the common anisotropic symmetries of most importance in seismic exploration and reservoir characterization. The model should be defined by parameters which can clearly reflect the seismic responses or mechanisms of anisotropy. Then, the theoretical modeling and experimental measurements of these parameters can be used to constrain the optimization all through the working flow. The optimized anisotropic velocity model should not only minimize the time misfits, but also be reasonable from the point of view of geology and rock physics.

Another thing that is going to be demonstrated in this thesis is the potential contribution of downhole microseismic monitoring to a better understanding of subsurface anisotropy beyond the laboratory. Since downhole microseismic monitoring is usually

carried out close to the source locations, it can be considered a quasi in-situ experiment. The observations are expected to be more reliable compared to surface reflection or surface microseismic dataset which are intensively influenced by path effects such as scattering and attenuation. New insights into subsurface media could be gained by comparing with the results of theoretical and experimental studies.

1.2 Seismic anisotropy

Seismic anisotropy is caused by the preferred-oriented heterogeneity of different scales. Such aligned heterogeneous structures include the bedding-parallel mineral particles and organic matters with low aspect ratio and compliant properties in the crustal rock (Johnston and Christensen, 1995; Vernik and Liu, 1997; Sayers, 2013; Sone and Zoback, 2013a), the natural and induced fractures of different scales in the crust (Hudson, 1981; Schoenberg and Sayers, 1995; Sayers and Kachanov, 1995; Peng and Ben-Zion, 2004), the strain-induced lattice-preferred orientation of olivine in the upper mantle (Nicolas et al., 1973; Zhang and Karato, 1995) and so on. The deformed pore space under the stress in a specific direction can also form aligned structures and cause elastic anisotropy (Shapiro and Kaselow, 2005).

According to the existence of mirror or rotational symmetry, anisotropic symmetries are sorted into different classes, such as triclinic, monoclinic, orthorhombic, transversely isotropic, cubic model and so on. The anisotropic symmetries most commonly used in seismic exploration and reservoir characterization are *Transversely Isotropic* and *Orthorhombic Model* (Grechka, 2009; Mavko et al., 2009). Transversely isotropic (TI) model is associated with a single set of aligned structures that exhibits rotational symmetry, such as the vertical cracks and the horizontal or tilted fabric laminations. According to the direction of symmetry axis, vertical, horizontal and tilted TI models are defined respectively. Vertical transversely isotropic (VTI) model used in this study is characterized by a stiffness matrix with five independent elements in the following form (Tsvankin, 1997)

$$c^{(\mathrm{VTI})} = \begin{pmatrix} c_{11} & c_{11}-2c_{66} & c_{13} & 0 & 0 & 0 \\ c_{11}-2c_{66} & c_{11} & c_{13} & 0 & 0 & 0 \\ c_{13} & c_{13} & c_{33} & 0 & 0 & 0 \\ 0 & 0 & 0 & c_{55} & 0 & 0 \\ 0 & 0 & 0 & 0 & c_{55} & 0 \\ 0 & 0 & 0 & 0 & 0 & c_{66} \end{pmatrix} \tag{1.1}$$

Orthorhombic model usually represents a combination of two or three joint sets of aligned structures with symmetry axes perpendicular to each other, such as vertical fractures embedded in the horizontal layer (see for example Figure 4.4). If the Cartesian coordinate axes are rotated to the directions of three symmetric axes, the orthorhombic stiffness matrix consists of nine independent elements and is written as

(Tsvankin, 1997)

$$c^{(\text{ORT})} = \begin{pmatrix} c_{11} & c_{12} & c_{13} & 0 & 0 & 0 \\ c_{12} & c_{22} & c_{23} & 0 & 0 & 0 \\ c_{13} & c_{23} & c_{33} & 0 & 0 & 0 \\ 0 & 0 & 0 & c_{44} & 0 & 0 \\ 0 & 0 & 0 & 0 & c_{55} & 0 \\ 0 & 0 & 0 & 0 & 0 & c_{66} \end{pmatrix} \tag{1.2}$$

Stiffness coefficients are defined as fundamental parameters only describing the stress-strain relationships, and thus are not commonly used in seismic applications. To connect the anisotropic media directly with seismic signatures or the mechanisms of anisotropy, equivalent manners of representing anisotropic media are introduced, such as Thomsen-style parameters and fracture compliance (see Section 4.3).

The primary kinematic response of seismic anisotropy results from the fact that phase velocities of seismic waves in anisotropic media are direction-dependent (Figure 1.1a). By definition, phase velocity v measures the advance of wavefront along the wavefront normal $\boldsymbol{n}$,

$$v = \frac{\partial \psi(\boldsymbol{x}, t)}{\partial t} \Big/ \left| \frac{\partial \psi(\boldsymbol{x}, t)}{\partial \boldsymbol{x}} \right| \qquad \boldsymbol{n} = \frac{\partial \psi(\boldsymbol{x}, t)}{\partial \boldsymbol{x}} \Big/ \left| \frac{\partial \psi(\boldsymbol{x}, t)}{\partial \boldsymbol{x}} \right| \tag{1.3}$$

where $\psi(\boldsymbol{x}, t)$ is the phase function and $\boldsymbol{n}$ represents the most rapidly phase-propagating direction. In anisotropic media, wavefront normal $\boldsymbol{n}$ usually deviates from the direction of wave energy propagation. Such deviation can be quantitatively described by the relation between phase velocity v and group velocity vector $\boldsymbol{g}$,

$$v = \boldsymbol{g} \cdot \boldsymbol{n} \tag{1.4}$$

where $\boldsymbol{g}$ defines the velocity and direction of wave energy propagation (see Figure 1.1b). Therefore, the wavefront shapes in anisotropic media become more complex than that in isotropic media. Shear waves can split into two components with polarizations lying in different characteristic planes and propagating with different phase velocities (see Figure 3.9, 3.10). In homogenous transversely isotropic media, the wavefront of SH-wave is always an oblate ellipsoid in vertical planes (Helbig, 1983); the wavefront of SV-wave can show triplication at some critical points (Vavryčuk, 2003) (see Figure 1.1b).

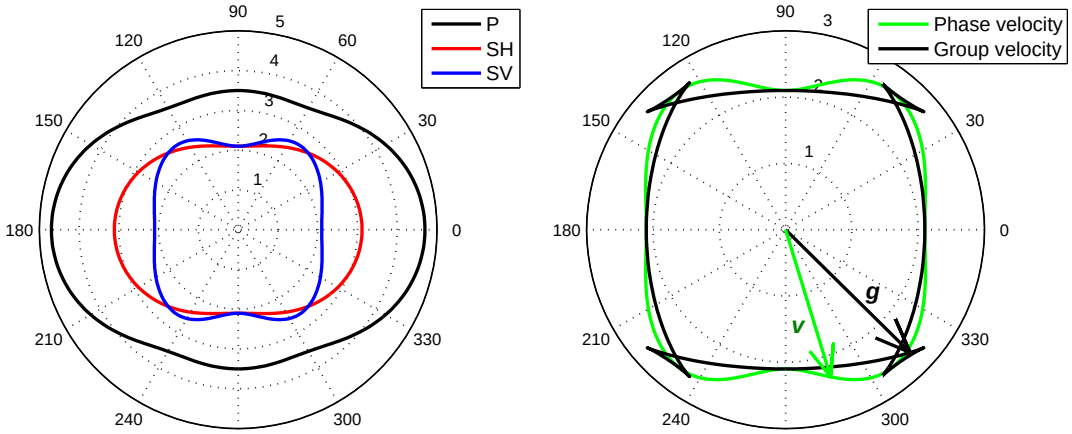

(a) (b)

Figure 1.1: (a) Phase velocities of P-, SH- & SV-waves within a vertical plane in a VTI media with elastic parameters V_P=3.5km/s, V_S=2.1km/s, ϵ=0.4, δ=-0.1, γ=0.6; (b) Phase and group velocities of SV-wave in the same media. $\boldsymbol{v}$ and $\boldsymbol{g}$ are the phase and group velocity vectors corresponding to the same wavefront normal $\boldsymbol{n}$. Triplications of SV-wave are observed in the group velocity surface.

In transversely isotropic media, there is only one symmetric axis around which the rotational symmetry exists. Phase velocities keep the same features in vertical symmetry planes of different azimuth (see Figure 1.1a). In orthorhombic media there are three symmetric axes which are orthogonal to each other. Phase velocities are symmetric with respect to three symmetry planes. An azimuthal anisotropy can be observed in seismic response.

Figure 1.2 shows the phase velocities in a homogenous orthorhombic media consisting of horizontal fabric laminations and a preferred-oriented vertical fracture set (see Figure 4.4). Phase velocities in three symmetry planes show different signatures. In the horizontal symmetry plane (x1-x2), the azimuthal anisotropy caused by the vertical fracture set can be observed. There are more conical points where the phase velocities of two shear waves intersect with each other and the "singularities" occur in the ray-tracing algorithm (see Section 2.3.1). In orthorhombic media, the definitions of "SH-wave" and "SV-wave" which have horizontal and vertical polarizations as in transversely isotropic media exist only within three symmetry planes. The polarizations of two S-waves beyond the symmetry planes are no longer in horizontal or vertical directions. As approaching to the conical points, the deviations from horizontal and vertical planes become larger. However, the orthogonal relationship between the polarizations of two S-waves always exist according to the solutions of Christoffel equations (Eq.2.5).

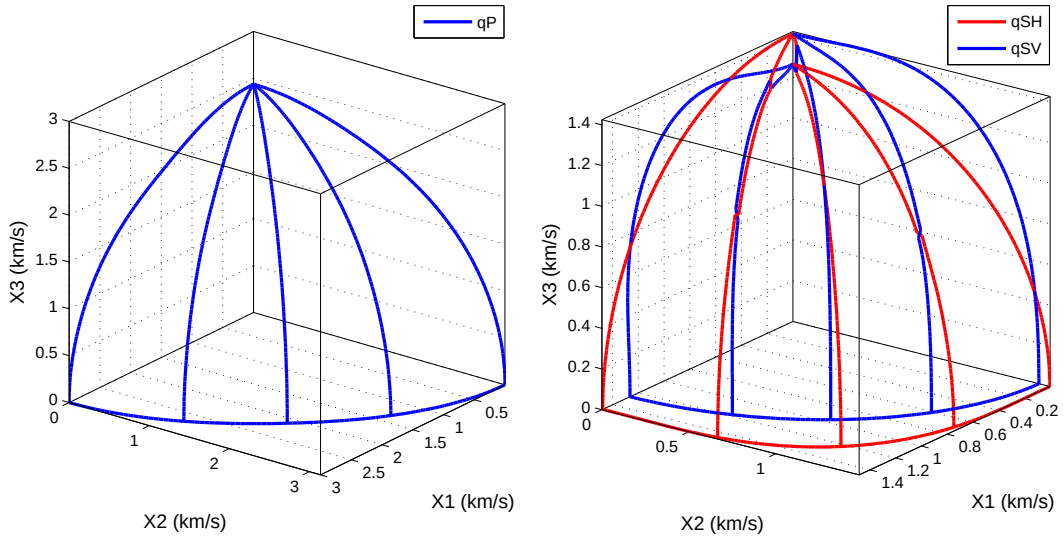

Figure 1.2: Phase velocities in an orthorhombic media with density-normalized elastic parameters (km^2/s^2): a_{11}=9, a_{12}=3.6, a_{13}=2.25, a_{22}=9.84, a_{23}=2.4, a_{33}=5.9375, a_{44}=2, a_{55}=1.6, a_{66}=2.182. The coordinate axes coincide with the symmetric axes.

1.3 Influences of anisotropy on microseismic data processing and interpretation

As the applications of microseismic techniques in monitoring the hydraulic fracturing of unconventional reservoirs have increased rapidly, the influences of anisotropy on microseismic data processing and interpretation have been paid more attention (Vavryčuk et al., 2008; Verdon et al., 2009; Grechka et al., 2011; Li et al., 2013). In shale formations of strong anisotropy, the variation of seismic velocity can be up to 40% (see Chapter 3). Seismic anisotropy can significantly influence the location of microseismic events, the inversion and interpretation of source mechanisms and eventually the estimates of fracture geometry and stimulated volume.

Figure 1.3 shows the ray trajectories and first-arrival times of P-, SH- and SV-waves in an isotropic media and a weakly transversely isotropic media. This is a vertical downhole monitoring system in a shallow coalbed methane reservoir (see details in Section 2.6). Vp_0 and Vs_0 are derived from sonic logs and calibrated by perforation shots. A weakly transversely isotropic model is obtained by optimization (see Section 2.6.2). We can see that the ray trajectories in the anisotropic media deviate significantly from those in the isotropic media, especially for SV-wave. The first-arrival times in the anisotropic media differ greatly from the isotropic media, even for weak anisotropy, which can lead to large errors of event locations.

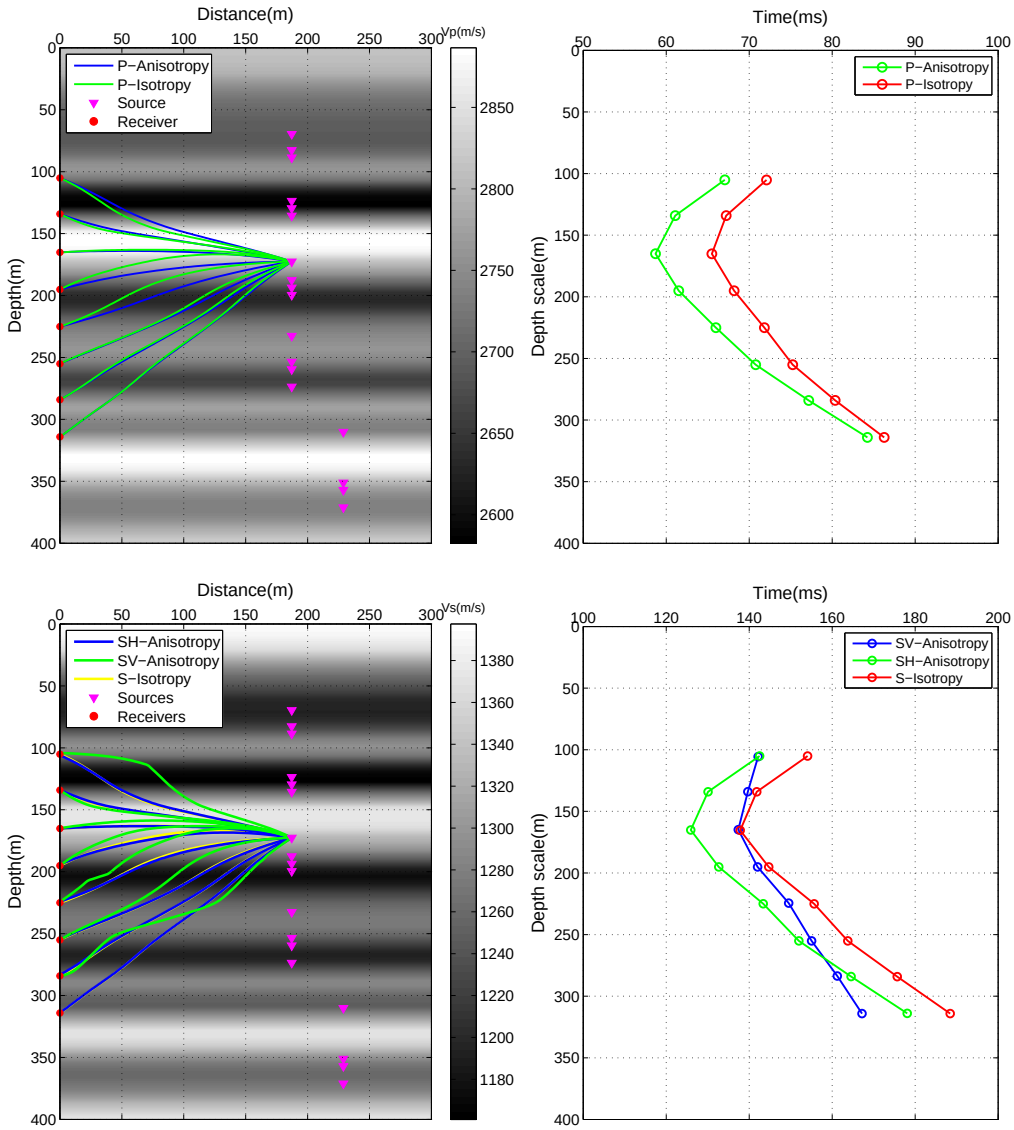

Figure 1.3: Ray trajectories & first-arrival times in weak transversely isotropic media (ϵ=0.023, δ=-0.090, γ=0.100) and isotropic media for a real downhole monitoring system in a coalbed methane reservoir (see details in Section 2.6).

After microseismic events are located correctly, source mechanisms are usually investigated to understand the failure details of the events. Seismic wavefield $\boldsymbol{u}(\boldsymbol{x},t)$ generated by an effective point source is represented as

$$u_n(\boldsymbol{x}, t) = M_{pq} * G_{np,q} \tag{1.5}$$

where $\boldsymbol{M}$ is the moment tensor, $\boldsymbol{G}$ is the Green function and n, p, q are the axis index (Aki and Richards, 2002). Seismograms are projected back to the focal area through the Green function $\boldsymbol{G}$ to yield the moment tensor $\boldsymbol{M}$. Then, the moment tensor is decomposed in different manners into DC, isotropic and CLVD components. The fault plane solution, seismic moment M_0 and volumetric strain are obtained from different components.

However, the general technical procedure may produce poor results due to the influences of anisotropy. First, the wave-propagating paths and the travel-times from the effective source point to the receivers as well as the polarizations and amplitudes differ greatly in an anisotropic media and a isotropic media. Therefore, the anisotropic ray tracing or waveform modeling should be employed to calculate the Green function. Another influential factor that is usually neglected is the anisotropic effect in the focal area. The moment tensor elements in an anisotropic media are expressed as (Aki and Richards, 2002)

$$M_{ij} = uSc_{ijkl}v_k n_l \tag{1.6}$$

where u is the slip distance, S is the area of fault plane, c_{ijkl} is the stiffness coefficients, $\boldsymbol{v}$ and $\boldsymbol{n}$ are the slipping vector and the fault plane normal. Generally, the pure shear fault slip ($\boldsymbol{v} \perp \boldsymbol{n} = 0$) in anisotropic focal area do not produce pure double-couple moment tensor as in isotropic media. Direct decomposition of moment tensor may lead to artificial non-DC components and incorrect fault solutions (Vavryčuk, 2005; Vavryčuk et al., 2008; Chapman and Leaney, 2012).

1.4 Geology and rock physics in microseismic inversion

Integrating geology and rock physics into an inversion problem has been widely acknowledged in reflection seismic applications. However, this approach has not been commonly adopted in microseismic applications. In this study, geological information and rock physics knowledge are deeply integrated into and highlighted in the working flow. They play crucial roles in building the initial model, restricting the search space and interpreting the results.

Hydraulic fracturing operations are usually carried out after detailed borehole geological and geophysical investigations. Thus, large amounts of geological data are

available for microseismic data processing and interpretation. For the anisotropic velocity model inversion in this study, the stratigraphic setting, sonic logs, core data and local stress map are collected from publications and open documents. Stratigraphic setting provides the frame of the velocity model and helps to figure out the layers of different properties. From the sonic logs, one can obtain the elastic parameters in the vertical direction and their gradients within the layers. Mechanical parameters, such as Young's modulus, Poisson's ratio and the Brittleness Index, can also be derived from sonic logs, according to which one can predict the stratigraphic distribution of fractures. Core analyses reveal some fundamental geological information such as mineral compositions, organic content and fracture geometry, which are extremely important for rock physics modeling and interpretations of the results.

In recent decades, there have been many laboratory measurements of anisotropy in rocks followed by dozens of rock physics models addressing the relationships between anisotropy and mineral composition, organic content, stress, fracture distributions (Hornby et al., 1994; Vernik and Liu, 1997; Wang, 2002; Sayers and Kachanov, 1995; Sone and Zoback, 2013a, etc.). Although the laboratory measurements are implemented in ultrasonic frequency and under simulated conditions, the results are still valuable references for the seismic applications. A priori knowledge of subsurface anisotropy can be obtained by integrating the geological information and rock physics results. This knowledge is used in this studies as the constraint on microseismic inversion (see Figure 1.4). Such constraint can refine the search space and make the inversion more stable and reliable. Most importantly, the obtained anisotropic model is physically and geologically reasonable rather than only producing the minimum data residual.

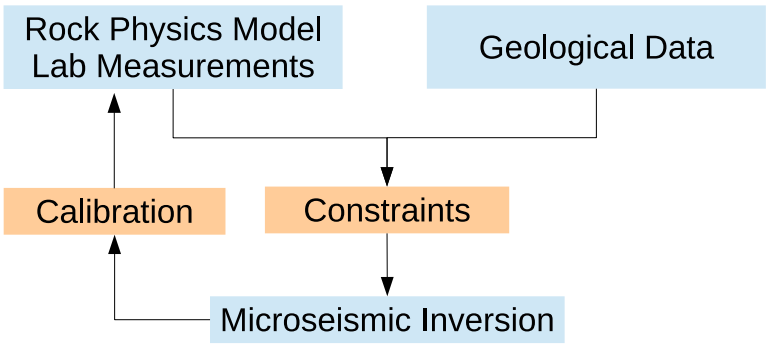

Figure 1.4: The roles of geology and rock physics in microseismic inversion for anisotropic velocity model.

1.5 Downhole microseismic monitoring as quasi in-situ experiments

In addition to the fracture geometry revealed by event locations and source mechanisms, a potential contribution of microseismic monitoring to a better understanding of subsurface media has been noticed in recent years (see for example Verdon and Wuestefeld, 2013). Seismic signals emitted by microseismic events and recorded by sensor arrays can be used to measure the local properties of subsurface media. According to the way of deploying receiver arrays, two alternative monitoring techniques are commonly used: surface and downhole microseismic monitoring.

In surface microseismic monitoring, hundreds or even thousands of geophones are deployed at the surface or buried in a shallow depth above the target reservoir as is routinely done in reflection seismic survey (see Figure 1.5). Broad sampling of wavefield along the surface provides a wide-azimuth observation which allows robust estimations of source mechanism and fracture geometry. However, surface microseismic monitoring surfers from the same negative factors as reflection seismic data. Signal-to-noise ratio is significantly reduced due to the scattering and attenuation in a long-distance propagation and near-surface structures. Since the aperture within the vertical plane is limited, the properties of subsurface media in the lateral direction cannot be well resolved. All the overlying formations contribute to the seismic responses, from which the response of a specific target is hard to be distinguished.

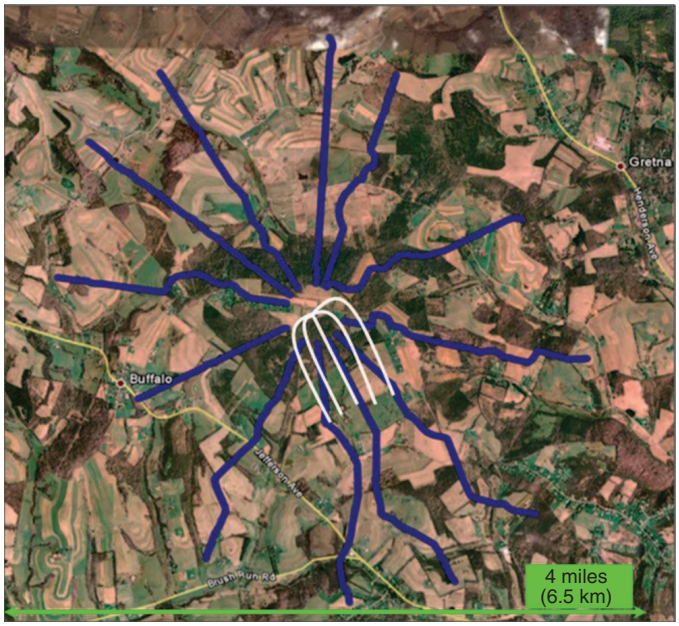

Figure 1.5: Map view of a typical star-shaped surface monitoring system for hydraulic fracturing treatment in a shale gas reservoir (after Duncan and Eisner, 2010). Surface arrays are displayed in blue and the treatment wells are displayed in white.

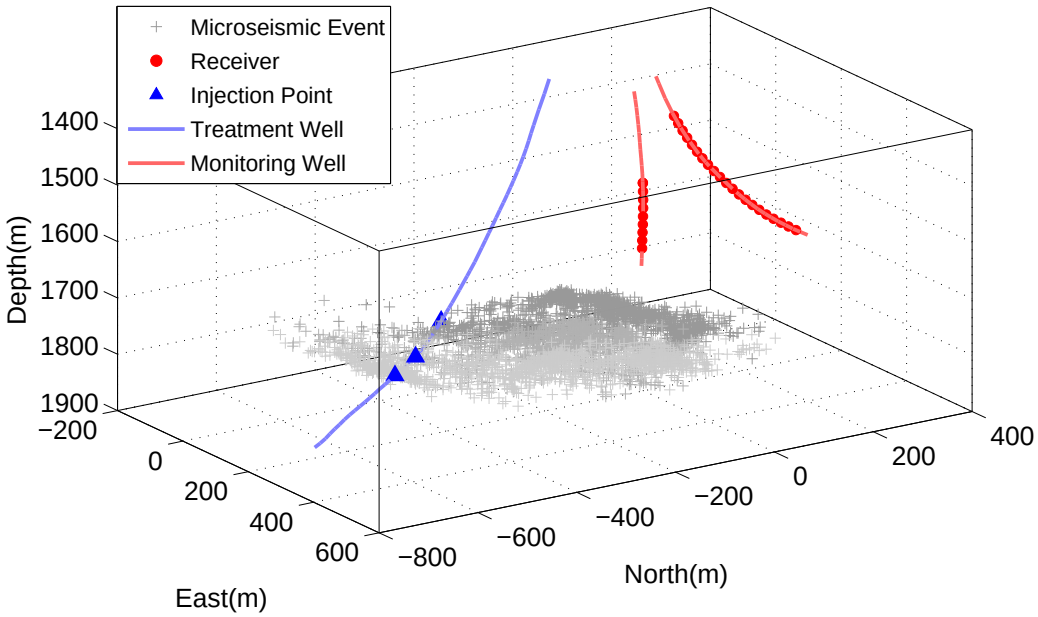

Figure 1.6: A typical downhole monitoring system for hydraulic fracturing treatment in a shale gas reservoir (see details in Chapter 3).

In downhole microseismic system, tens of three-component geophones are deployed in treatment wells or offset wells close to the target reservoir (see Figure 1.6). Attenuation, scattering and other negative effects along the wave-propagating path are minimized due to the short distance from source to receivers, which leads to a high signal-to-noise ratio in seismograms. Seismic signals recorded in downhole arrays particularly reflect the local properties of subsurface media around the target area. Although the spatial sampling of wavefield in downhole monitoring is far less than surface monitoring, a large number of microseismic events widely distributed with respect to the downhole array provide much better aperture than expected and intense ray coverage within a local area. Therefore, downhole microseismic monitoring can serve as a reliable, artificial, quasi in-situ experiment to improve the understanding of subsurface media. The measurements using the downhole microseismic dataset can help us to calibrate the laboratory studies and gain new insights into crustal rocks from the prospective of quasi in-situ experiments in seismic frequency band (see Figure 1.4).

1.6 Shale anisotropy: from transversely isotropic model to orthorhombic model

Shales are composed of much finer grains (mostly <1/256 mm) than sandstone and are distinguished from mudstone by lamination or fissility (Boggs, 2011). The mineral composition of shale is dominated by clay, fine-size quartz and carbonate. A significant amount of organic matter is presented in gas-bearing shales. The total organic

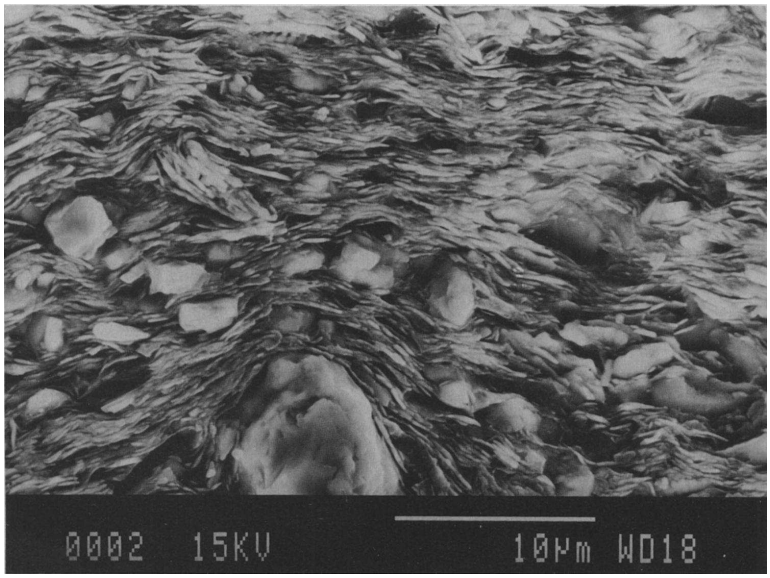

Figure 1.7: Scanning electron micro-photograph of shale sample (after Hornby et al., 1994).

carbon (TOC) of some prospective gas shales are listed as Bakken (4.9%~21%), Barnnet (3%~8%), Marcellus (3%~14%), Eagle Ford (2%~6%) and Horn River (2%~5%) in weight percentage (Vernik and Liu, 1997; Hall, 2000).

Clay minerals have plate-like shapes and more compliant mechanical properties. Therefore, they are rotated more easily by the strain in compaction history and are well aligned in bedding-parallel direction (Curtis et al., 1980) (see for example Figure 1.7). In organic-rich shale, kerogen exhibits as lenticular microlayers dispersed among clay matrix and sporadic laminations in bedding-parallel direction as the petrographic and SEM observations show (Vernik and Nur, 1992; Vernik and Landis, 1996). The alignment and lamination of the low-aspect-ratio, compliant particles, such as clay and kerogen, result in the decrease of effective stiffness in bedding-normal direction and form a transversely isotropic (TI) model which is the so-called fabric anisotropy of shale.

Laboratory experiments show that, at the core scale, the degree of fabric anisotropy depends strongly on the contents of clay and kerogen (Johnston and Christensen, 1995; Vernik and Liu, 1997; Sone and Zoback, 2013a). However, the alignment and lamination of fabric can be prevented and interrupted by the existence of stiffer and non-platy minerals such as quartz (see Figure 1.7). As a result, the fabric anisotropy of shale has a negative correlation with the quartz content (Curtis et al., 1980). In addition, the fabric anisotropy of shale can be further enhanced at low effective stresses by the presence of bedding-parallel microcracks originating from hydrocarbon generation and overpressure (e.g. Vernik and Liu, 1997)

In addition to the clay mineral and organic matter, a preferred-oriented fracture set is another important source of shale anisotropy. The fractures represent the mechanically weak planes in host rock. If they are preferred-aligned in one particular direction, the host rock effectively exhibits elastic anisotropy. As possible fluid channels and mechanically weak areas, fractures play crucial roles in reservoir characterization and hydraulic fracturing (Fisher et al., 2004; Gale et al., 2007; Dahi-Taleghani et al., 2011).

Mechanically, the occurrence of fractures depends on the rock strength under shear or tensile loading. As different mineral compositions of rock constitute mechanically distinct intervals, the fractures usually show a stratigraphic distribution due to mechanical stratigraphy (Laubach et al., 2009; Gale et al., 2014). Shales with high quartz or carbonate fractions exhibit much higher brittle strength, and therefore possess more natural or induced fractures. Systematic core analyses (Gale et al., 2014) and mechanical analyses (Cosgrove, 1998; Crampin and Atkinson, 1985) show that the aligned vertical or sub-vertical natural fractures are the most common and important natural fracture groups in shale. Such natural fractures with a high-dipping angle to the bedding plane are commonly recognized as the product of hydrofracturing process. According to fracture mechanisms, the fracture opens more easily in the direction of minimum horizontal stress and propagates along the maximum horizontal stress. The dominant fracture strikes therefore coincide with the maximum horizontal stress.

Vertical fractures and horizontal fabric laminations in shale combine to form a geologically important subset of orthorhombic media—the vertically fractured TI media (Schoenberg and Helbig, 1997) (see Figure 4.4). The bedding-parallel plane and the vertical fracture-strike and fracture-normal planes serve as the symmetry planes. In this study, the normal and tangential fracture compliances are used to effectively describe the elastic properties of the vertical fracture set embedded in the background TI media.

1.7 Outline of this thesis

The motivation, research background, basic principles and working philosophy of this thesis have been introduced in this chapter. Then, the technical details of microseismic inversion for anisotropic media are presented in Chapter 2. Chapter 3 and Chapter 4 show successful applications of microseismic inversion for estimating the fabric and fracture-induced anisotropy of shales. Chapter 5 concludes this thesis with discussions of the results and the outlook.

Chapter 2 presents the methodology used in this thesis. A layered model is used in the inversion, within which the lateral heterogeneity is dismissed and the vertical gradients of transversely isotropic parameters are taking into account. Synthesized travel-time is computed by an anisotropic ray-tracing program, which is adapted from the ANRAY Software Package. The inherent singularity problems in the ray-tracing method

are analyzed and the solutions are proposed. Two inversion strategies are involved in this study: the Gauss-Newton method (for the fabric anisotropy) and the global searching method (for the fracture-induced anisotropy). The uncertainties introduced by the computation of triggering time (T_0) into the velocity model inversion and event location are also discussed. An application example in a coalbed methane reservoir is present to verify the iterative gradient-based inversion and illustrate the T_0 issue in the configuration with limited aperture.

Chapter 3 focuses on the estimation of the fabric anisotropy of shale using the approach developed in this study. A comprehensive review of the geological background and laboratory measurements of shale fabric anisotropy is presented. A priori knowledge of the fabric anisotropy is obtained by integrating the geological information and rock physics results. This knowledge serves as constraint on microseismic inversion. Then the downhole microseismic dataset used in this study is presented and analyzed. A gradient-based inversion is then implemented to obtain the optimal fabric anisotropy. The results are compared with laboratory measurements. The improvements of time misfits and microseismic event locations before and after the optimization are discussed.

Chapter 4 addresses the additional fracture-induced anisotropy in shale formations of high brittleness. The general characterizations of fractures in shale are reviewed. The fracture distribution, fracture geometry are obtained from the geological and mechanical analyses. Different representations of the fractured media are compared and the fracture compliances are chosen as the parameters in this study. The optimal VTI model obtained in Chapter 3 is used as the background model. Following that, the rock physics constrains on fracture compliance are presented. Then the methodology of obtaining the optimal fracture compliance is introduced and applied to the same dataset as in Chapter 3.

Chapter 5 summarizes the approach developed in this thesis and the findings in the applications to shale gas reservoir. The limitations and possible improvements of this approach are discussed.

Chapter 2

Microseismic inversion for anisotropic velocity model

2.1 Introduction

Hydraulic fracturing treatment is mainly used to enhance the permeability of unconventional reservoirs. Microseismic monitoring is usually employed to map the hydraulic-fracturing operations. Inhomogeneous anisotropy exhibited in unconventional reservoirs has proved an obstacle to the advanced microseismic data processing and interpretation. The conventional approaches to constructing velocity model in microseismic applications are not sophisticated enough to deal with the inhomogeneous anisotropic cases. To address this issue, several studies on extracting anisotropic velocity model from microseismic data have been presented in recent years. Grechka et al. (2011), Grechka and Yaskevich (2013, 2014) extended the passive seismic travel-time tomography (see Thurber, 1993) to estimate the triclinic anisotropy simultaneously with the locations of microseismic events and apply it to Bakken shale reservoir. Li et al. (2013) extended the double-difference tomography to jointly invert microseismic location and VTI model. Michel and Tsvankin (2014, 2015) attempt to use the waveform inversion to derive the VTI model and source mechanisms of microseismic events.

The purpose of this chapter is to present the technical details of the approach proposed in this thesis. The model geometry is defined considering the limited spatial scale of microseismic monitoring and the general sedimentary background of unconventional reservoir as well as the complexity of inversion problem. Two anisotropic symmetries—transversely isotropic model and orthorhombic model—of importance in seismic exploration and reservoir characterization are taking into account. The parameters that can directly reflect seismic response and the mechanisms of anisotropy are chosen to define the anisotropic velocity model. An anisotropic ray-tracing algorithm is used to calculate the synthesized data for the travel-time inversion. Two inversion strategies are involved in this approach to determine different components of anisotropic veloc-

ity model. The issues of computing triggering time (or origin time), which is usually disregarded in microseismic velocity inversion and source location, are analyzed theoretically and illustrated with examples. Finally, an application example of downhole microseismic monitoring in a shallow coalbed methane reservoir is presented to further illustrate the T_0 issue in the configuration of limited aperture and to verify the capability of the iterative gradient-based inversion for anisotropic velocity model.

2.2 Model representation

There are a wide variety of geometric schemes for representing Earth's media, such as layer model, grid-node model, block model and continuous function model (Thurber, 1993). Their abilities of approximating the true subsurface structures and the resulting computational costs are different. Various properties of media are defined in each geometric unit. In this study, a layered model is used considering the limited spatial scale of microseismic monitoring and the general sedimentary background of unconventional reservoir. Transversely isotropic (TI) and orthorhombic models, which are closely associated with a single set and multiple joint sets of aligned structures in subsurface, are defined within the layered model.

2.2.1 Model geometry

A seismic inversion problem consists of the forward modeling part, which calculates the simulated wavefield, and the inversion part, which updates the model by comparing the synthesized and observed data. The model representations used in forward modeling and inversion are not necessarily the same. The forward modeling always prefers more sophisticated model to create more realistic seismic wavefield. The anisotropic ray-tracing algorithm in this study uses a grid-node velocity model which is able to handle the heterogeneities in 3-D space. Elastic parameters between grid nodes are determined by linear or B-spline interpolations. However, from the inverse theory point of view, the model complexity is a critical issue. The model space grows exponentially with the number of model parameters, and therefore the inversion may fail due to the non-uniqueness or an unbearable computational cost. There is a a trade-off between the approximation of subsurface media and the complexity of inversion problem.

For a typical microseismic-monitoring system in unconventional reservoirs, the dimension scale in the horizontal plane is about in the order of 10^2 meters. Considering the limited scale in horizontal directions and the relative flat sedimentary background of unconventional reservoirs such as gas shale or tight gas-sand, the velocity model in microseismic inversion can be defined by layers of constant thickness, within which the lateral heterogeneities can be ignored (see Figure 2.1). Since the change of sedimentary environment in vertical direction is larger than that in horizontal direction, the vertical gradients of elastic parameters within each layer are considered when calculating the synthesized travel-time (see Figure 2.1).

2.2.2 Representation of transverse isotropy

The bedding-parallel fabric or lamination in sedimentary rock can be represented by a transversely isotropic model. Basically, the parameterization of TI model in microseismic inversion can use either five independent stiffness constants [c_{11}, c_{13}, c_{33}, c_{55}, c_{66}] or the isotropic velocities and Thomsen parameters [V_{P0}, V_{S0}, ε, δ, γ]. For instance, the phase velocities of seismic waves in the VTI model can be explicitly expressed in terms of stiffness constants (Grechka, 2009)

$$V_{P,SV}^2(\theta) = \frac{1}{2\rho}\left\{(c_{11}+c_{55})\sin^2\theta + (c_{33}+c_{55})\cos^2\theta \pm\sqrt{\left[(c_{11}-c_{55})\sin^2\theta - (c_{33}-c_{55})\cos^2\theta\right]^2 + 4(c_{13}+c_{55})^2\sin^2\theta\cos^2\theta}\right\} \tag{2.1}$$

$$V_{SH}^2(\theta) = \frac{c_{66}\sin^2\theta + c_{55}\cos^2\theta}{\rho} \tag{2.2}$$

or in terms of V_{P0}, V_{S0} and Thomsen parameters

$$V_{P,SV}^2(\theta) = V_{P0}^2\left[1+\varepsilon\sin^2\theta - \frac{f}{2} \pm\frac{f}{2}\sqrt{1+\frac{4\sin^2\theta}{f^2}(2\delta\cos^2\theta - \varepsilon\cos 2\theta) + \frac{4\varepsilon^2\sin^4\theta}{f}}\right] \tag{2.3}$$

$$V_{SH}^2(\theta) = V_{S0}\sqrt{1+2\gamma\sin^2\theta} \tag{2.4}$$

where θ is the angle between wavefront normal and the vertical symmetry axis, V_{S0} and V_{P0} are the velocities of P- and S-waves in vertical direction, and $f = 1 - V_{S0}^2/V_{P0}^2$.

The first-order derivatives of phase velocities with respect to the stiffness constants and Thomsen parameters can be obtained from Equation 2.1~2.4 (see Figure 2.2). We can see that, for different waves, the dependence of phase velocities on the direction can be controlled by one or two specific Thomsen parameters, such as ε for P-wave, ε and δ for SV-wave and γ for SH-wave. However, it is difficult to distinguish the dominance of an individual stiffness constant for the specific wave. An individual stiffness constant cannot intuitively reflect the velocity signatures in anisotropic media. Thomsen parameters, defined as a combination of stiffness constants (see Equation 3.1), have more intuitive relations with kinematic signatures of seismic wave such as wavefront shapes. In addition, many laboratory or field measurements and theoretical modeling are presented in terms of Thomsen parameters because of its clear physical meaning and direct connections with seismic signatures. These provide the prior knowledge of Thomsen parameters which is important for initiating an optimization and evaluating the results, whereas the prior knowledge of stiffness constant is not convenient to be obtained. Therefore, Thomsen parameters are used to define the transversely isotropic media in this study (see Figure 2.1).

2.2.3 Representation of fracture-induced anisotropy

The presence of fracture sets usually reduces the order of symmetry class. For example, the transversely isotropic media containing one vertical fracture set degenerates into an orthorhombic media, which is described by nine independent stiffness constants instead of five. The inversion for nine stiffness constants is difficult due to the inherent limitation of inversion problem when dealing with multi-parameters. On the other hand, the stiffness constants have no explicit physical connections with the fractures, which makes it difficult to find the physical constraints for the inversion and interpret the obtained results. An alternative way is to decompose the fractured media into background media and fractures based on the linear-slip theory (Schoenberg, 1980; Schoenberg and Sayers, 1995). The effective normal and tangential fracture compliance (i.e., Z_N and Z_T) are used to describe the excess elastic compliance induced by the fracture set and imposed on the background media. With a clear physical meaning, the fracture compliance can be modeled theoretically and measured in laboratory and field, which provide the prior knowledge for the inversion and interpretation (see details in Section 4.3). The fractures only occur when the brittleness of the rock is high enough, and therefore show a distinctly stratigraphic distribution due to the mechanical stratigraphy (see Figure 4.1). Since the seismic resolution is limited, the effective fracture compliance in specified layer is assumed to be homogeneous (see Figure 2.1).

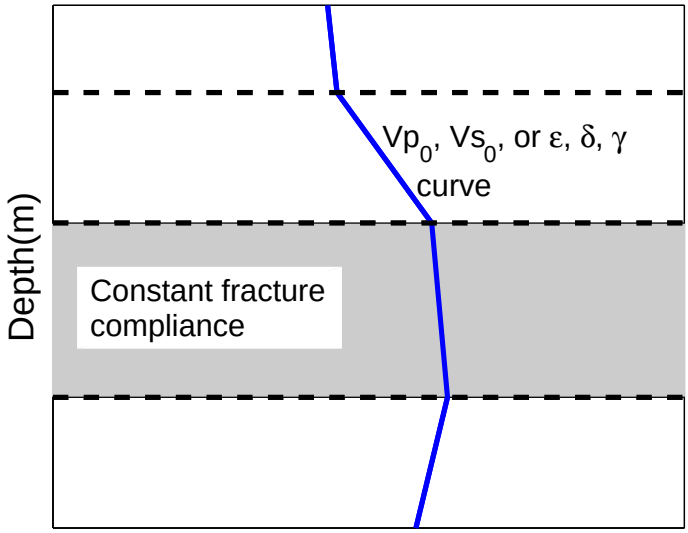

Figure 2.1: Sketch of the layered anisotropic velocity model used in this study. The vertical gradients of V_{P0}, V_{S0} and Thomsen parameters within each layer are taking into account. The effective fracture compliance defined only within specific layers is assumed to be homogeneous.

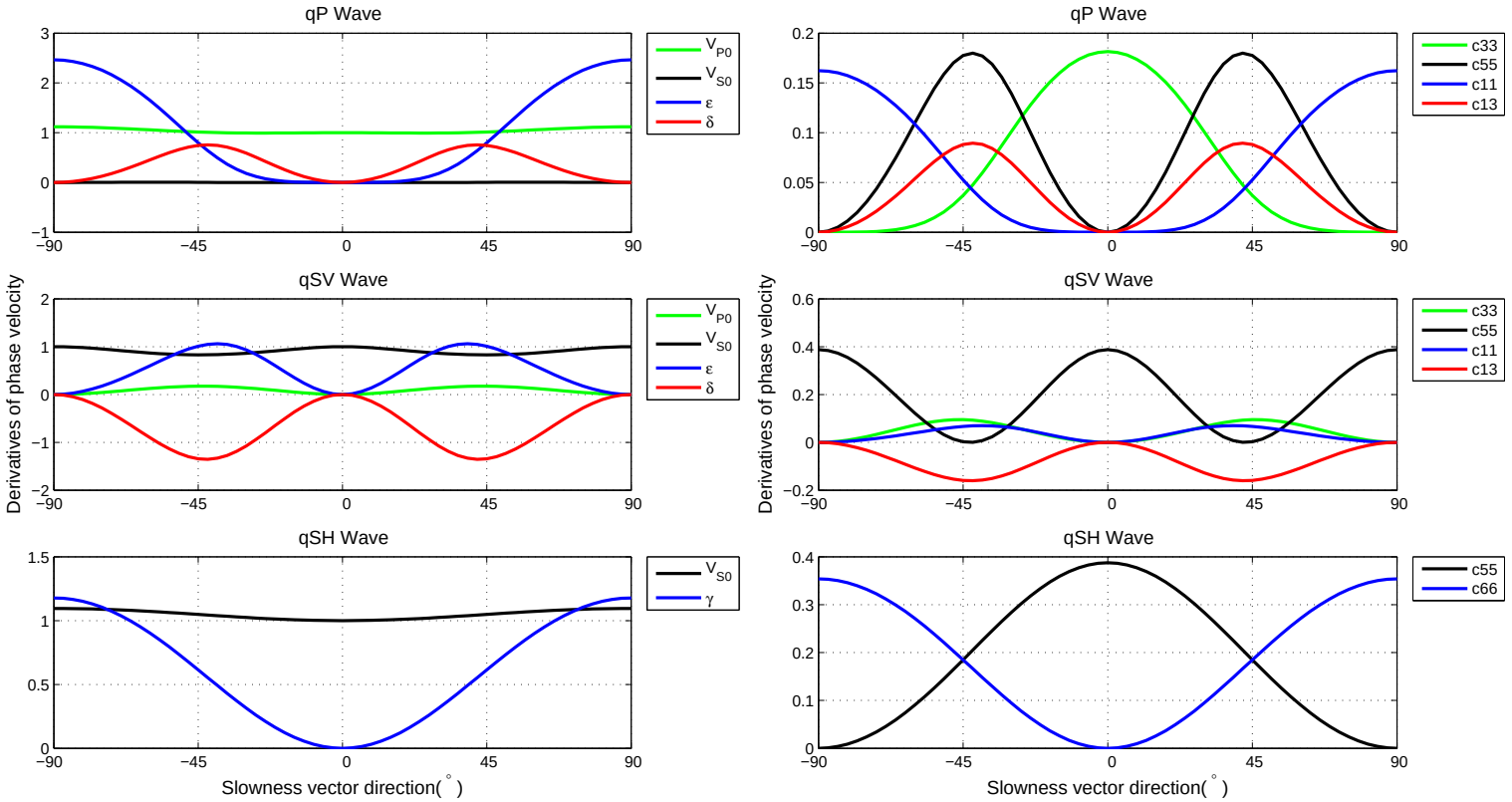

Figure 2.2: The derivatives of phase velocities with respect to Thomsen parameters and elastic-moduli over the angle range $0°\sim180°$ from the vertical direction in homogeneous VTI media (V_P=2.755km/s, V_S=1.290km/s, ϵ=0.125, δ=-0.075, γ=0.100; the equivalent density-normalized stiffness c_{33}=7.59, c_{55}=1.66, c_{11}=9.49, c_{13}=3.66, c_{66}=2.00). The elastic parameters are extracted from the VTI model used in Figure 1.3.

2.3 Anisotropic ray-tracing algorithm

In this thesis, the inversion for anisotropic velocity model and the location of microseismic events are both accomplished by the travel-time based method instead of waveform-based method. The synthesized travel-time is computed by the anisotropic ray-tracing algorithm which is originally developed by Gajewski and Pšencík (1987) and is highly modified in this study for microseismic applications. This algorithm is based on the shooting method (i.e., the initial value ray tracing). The inherent singularity problems in the shooting method are analyzed and the solutions are proposed in this study.

Seismic ray is the high-frequency asymptotic solution of elastodynamic equation, and can be considered the local plane-wave approximations of curved wavefront under the high-frequency assumption (Červený, 2001). Simplifying the elastodynamic equation by substituting the plane wave solution yields the Christoffel equation written as

$$a_{ijkl} n_j n_k U_l = v^2 U_i \tag{2.5}$$

where a_{ijkl} is the density-normalized stiffness tensor, n_i is the component of wavefront normal $\boldsymbol{n}$ and U_i is the component of polarization vector. Equation 2.5 can be further transformed into Hamiltonian form as

$$\mathcal{H}(\boldsymbol{x},\boldsymbol{p}) = a_{ijkl}(\boldsymbol{x}) p_j p_k U_i(\boldsymbol{x},\boldsymbol{p}) U_l(\boldsymbol{x},\boldsymbol{p}) - 1 = 0 \tag{2.6}$$

which is exactly the eikonal equation for anisotropic media. According to the way of solving this equation, ray tracing can be accomplished by three approaches, *wavefront construction*, *shooting method* and *bending method*. For the velocity model inversion and the event location in anisotropic media, only travel-times and ray trajectories of three waves are needed. The shooting method is a suitable option due to a relative low computational cost and the ability of handling multi-arrivals.

2.3.1 Shooting method

The eikonal equation for anisotropic media (Eq. 2.6) is a first-order nonlinear differential equation of travel-time t, where $\nabla t = \boldsymbol{p}$. It can be resolved by the characteristic method as presented in Bleistein (1984). The derived ray-tracing system consists of two groups of equations expressed following the notations of Grechka (2009) as

$$\frac{dx_m}{dt} = a_{ijml} U_i p_j U_l \tag{2.7}$$

$$\frac{dp_m}{dt} = -\frac{1}{2} \frac{\partial a_{ijkl}}{\partial x_m} U_i p_j p_k U_l \tag{2.8}$$

where m = 1, 2, 3. The shooting of a ray is initiated by specifying the source point $\boldsymbol{x}_0$ and radiating direction $\boldsymbol{n}_0$. Then, the initial slowness vector $\boldsymbol{p}_0$ can be derived from

Christoffel equation (2.5). With the initial condition ($\boldsymbol{x}_0$, $\boldsymbol{p}_0$), Equation 2.7~2.8 are iteratively solved by the Runge-Kutta method step by step with constant time interval dt, and then the ray trajectory $\boldsymbol{x}$ and the travel-time t along it are obtained. The computational cost of shooting method depends on the complexity of velocity model, the number of time steps and the density of radiated rays. Since the shooting method numerically simulates the proceeding of wave energy along particular directions, the multi-arrivals resulting from inhomogeneous velocity model can be handled properly.

In anisotropic media, the shooting method does not work properly in some "singular regions" where two qS-waves propagate with nearly the same phase velocities (Gajewski and Pšencík, 1987). The ***singularity problem*** arises when the slowness (or phase velocities) surfaces of two qS-waves touch or intersect for a particular wavefront normal direction $\boldsymbol{n}_s$ (see Figure 2.3). When solving the ray-tracing system (Eq. 2.7~2.8) for a new step, the polarization terms $U_i U_l$ in the right-hand-side of equations should be determined firstly. Polarizations $\boldsymbol{U}$ and phase velocities v corresponding to P-, SH- and SV-waves are the three eigenvectors and eigenvalues of Christoffel matrix $a_{ijkl}n_j n_k$. Beyond the "singular regions", $a_{ijkl}n_j n_k$ has three different eigenvalues, and therefore $\boldsymbol{U}$ can be derived uniquely from Christoffel equation for a given phase velocity v and specified direction $\boldsymbol{n}$. However, at the singular point, SH- and SV-wave have the same phase velocities v_s for the wavefront normal $\boldsymbol{n}_s$, which means a non-unique polarization $\boldsymbol{U}$ for the given phase velocity (see Figure 2.3). Additional rules are necessary for picking the correct polarization $\boldsymbol{U}$ at the singular point. Otherwise,

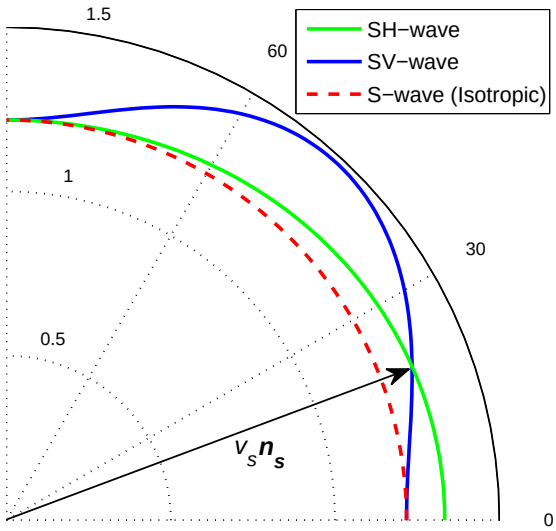

Figure 2.3: A singular point in the transversely isotropic media when the phase velocity surfaces of SH- and SV-wave intersect in the direction of wavefront normal $\boldsymbol{n}_s$. The elastic parameters are extracted from the VTI model used in Figure 1.3 (V_P=2.698km/s, V_S=1.218km/s, ϵ=0.125, δ=-0.075, γ=0.100).

the numerical solution of qS_1-wave may use the polarization of qS_2-wave when the ray stepping out of the "singular regions". As a result, the ray trajectory of qS_1-wave deviates from the correct direction and the polarization switches to qS_2-wave (see Figure 2.4). To overcome this inherent limit in the shooting method, numerical strategies are proposed in the frame of ANRAY software package and are presented in next section. Vavryčuk (2001) also reported the similar analyses of singularity problem and proposed the solutions. This study is carried out independently without using Vavryčuk (2001).

2.3.2 ANRAY software package

ANRAY package is designed for the computation of rays, travel-times, ray amplitudes and ray synthetic seismograms in 3-D laterally heterogeneous isotropic and/or anisotropic media. It is developed originally by Gajewski and Pšencík in 1980s and has been extended and improved in the last decades (`http://seis.karlov.mff.cuni.cz/software/sw3dcd19/anray/anray.htm`). The kernel algorithm is based on the shooting method (i.e., initial value ray tracing) (Gajewski and Pšencík, 1987; Červený, 2001). In this study, ANRAY program is highly modified for microseismic applications and is use as the engine of anisotropic ray tracing.

In microseismic inversion, we need to compute seismic rays and travel-times from a source to the specified receivers. Although ANRAY is based on the shooting method, it can perform an efficient 3-D two-point ray tracing. A fan of rays with sparsely sampled azimuths and declinations are initially radiated. Then, an iterative search for the rays terminating at the specified receivers is carried out. As it uses the paraxial ray approximation in searching procedure, the target can be achieved fast with only a few trials. In downhole microseismic-monitoring, the sources and receivers usually scatter irregularly in 3-D space (see Figure 1.6). The source-receiver configuration in ANRAY is modified for irregular geometry. To accelerate the computation, the program is parallelized for multi-CPU machine. Each source emitting rays is distributed to one thread which works independently in one CPU unit.

The anisotropic ray-tracing algorithm in ANRAY uses a slightly different ray-tracing equations (see Equation 3.6.15 in Červený (2001)) which is equivalent to Equation 2.7~2.8 in this thesis. It does not explicitly calculate polarizations $\boldsymbol{U}$ by solving Christoffel equation but by replacing the term $U_i U_l$ in Equation 2.7~2.8 with an implicit form D_{il}/D (see Equation 3.6.12~3.6.15 in Červený (2001)). This manner of calculating D_{il}/D is a bit faster than decomposing Christoffel matrix, but results in a new ***singularity problem***. When the points constituting the ray trajectory coincide with the singular points, the phase velocities of two qS-waves become the same, which results in the denominator $D = 0$ and $D_{il}/D \to \infty$ and then a breakdown of the iterative ray-tracing computation. Although the probability of coinciding with singular points in 3-D space is low, it is highly probable that seismic rays travel through the

vicinities of singular points ("singular regions") where the phase velocities of two qS-waves are quite close and the denominator term D become near zero. This can introduce significant numerical error into the iteratively solving of ray-tracing equations. To fix this problem, the original program is modified by replacing D_{il}/D with U_iU_l when the possible "singular regions" ahead the rays are detected. A threshold value of D is set as the indications of "singular regions" within which the polarization $\boldsymbol{U}$ is explicitly derived by decomposing the Christoffel matrix.

As discussed in the previous section, the shooting method, no matter using D_{il}/D or U_iU_l, may fail for qS-waves in anisotropic media due to the non-unique polarizations at the ***singular points***. ANRAY program picks the polarization terms by comparing the values of phase velocities. qS_1-wave is always assumed to be the faster wave. For the intersection singularity as shown in Figure 2.3, the faster wave can switch between qS_1- and qS_2-waves when the rays cross the singular point. This leads to incorrect ray trajectories and polarizations (see Figure 2.4). A numerical strategy of picking the correct polarizations using the history information of ray tracing is used in this study. Before the rays stepping into the "singular regions", the polarizations pertaining to the points just beyond the "singular regions" are recorded. The polarizations around the singular points are picked according to the rule that, the plane defined by polarization vector and ray axis should be consistent with the previous ray point (e.g. in TI media) or smoothly rotated (e.g. in orthorhombic media). This strategy prevents the polarization of qS_1-wave switching to qS_2-wave when stepping out the "singular regions" and produces correct ray solutions (see Figure 2.5).

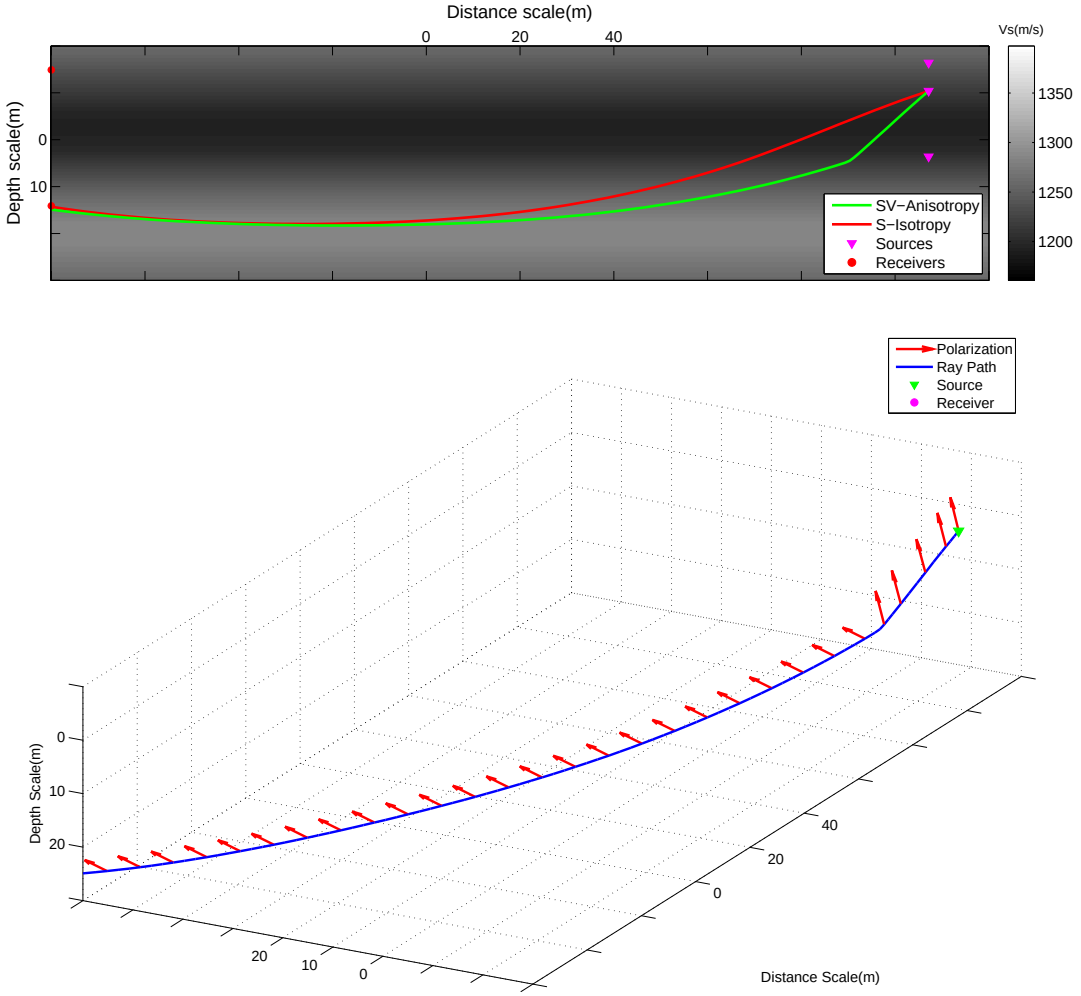

Figure 2.4: Ray trajectories of SV-wave being deviated by the singular point as indicated in Figure 2.3 and the polarizations switching between SV- and SH-wave. The VTI model and source-receiver geometry are the same as used in Figure 1.3 and 2.3.

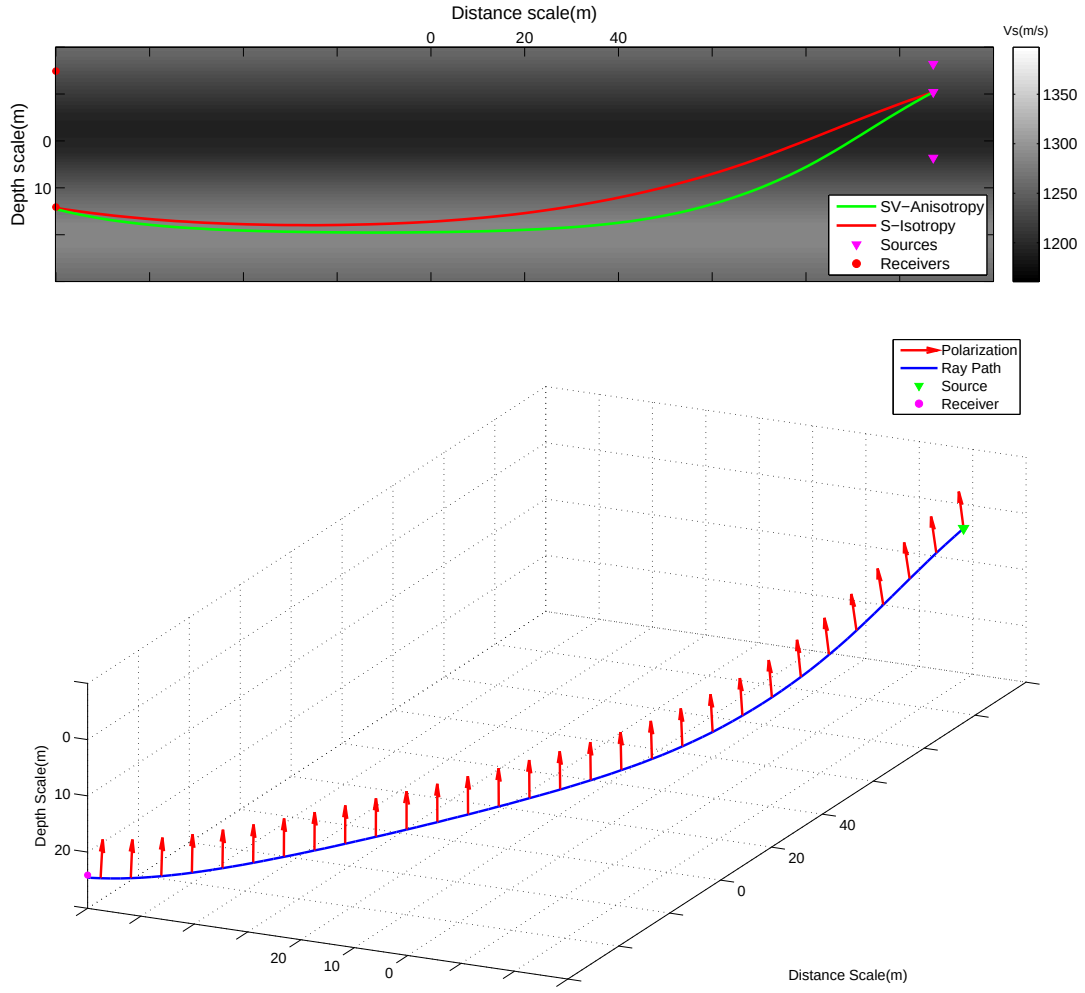

Figure 2.5: Ray trajectories and polarizations of SV-wave after fixing the singularity problems (in comparison with Figure 2.4).

2.4 Inversion strategy

In section 2.2, we have defined a layered anisotropic velocity model that consists of transverse isotropy and the additional fracture-induced anisotropy. Such model representation allows us to estimate these two components of anisotropic velocity model separately. The background TI media is heterogeneous in vertical direction and v_{P0}, v_{S0}, ε, δ, γ are defined in each layer. As a typical multi-parameters inversion, an iterative gradient-based method (the Gauss-Newton method) is used to solve this problem. The fracture-induced anisotropy exists only within the layer of high brittleness. Only two parameters (i.e., Z_N and Z_T) are needed to describe it. If the number of layers showing fracture-induced anisotropy is limited, a global search for the optimal Z_N and Z_T is possible.

2.4.1 Gauss-Newton method

The travel-time inversion for anisotropic velocity model can be expressed as a nonlinear least-square problem. The objective function is numerically defined as

$$C(\mathbf{m}) = \frac{1}{2}\left[\mathbf{d}_{cal}(\mathbf{m}) - \mathbf{d}_{obs}\right]^t \left[\mathbf{d}_{cal}(\mathbf{m}) - \mathbf{d}_{obs}\right] \tag{2.9}$$

where $\mathbf{d}_{obs}$ is the observed data, $\mathbf{d}_{cal}$ is the synthesized data, $\mathbf{m}$ is the model vector. $C(\mathbf{m})$ has no analytical form, but can be written in quadratic approximation by the truncated Taylor Series,

$$C(\mathbf{m}_0 + \Delta\mathbf{m}) \approx C(\mathbf{m}_0) + \nabla C_i(\mathbf{m}_0)\Delta\mathbf{m}_i + \frac{1}{2}\nabla^2 C_{ij}(\mathbf{m}_0)\Delta\mathbf{m}_i\Delta\mathbf{m}_j \tag{2.10}$$

where $\Delta\mathbf{m}$ is the small perturbation of model vector. To find the minimum of $C(\mathbf{m})$ around $\mathbf{m}_0$, the partial derivative of equation 2.10 with respect to $\Delta\mathbf{m}$ equaling zero yields the solution corresponding to the *Newton's method*,

$$\Delta\mathbf{m}_j = -\nabla^2 C_{ij}(\mathbf{m}_0)^{-1}\nabla C_i(\mathbf{m}_0) = -H_{ij}^{-1}\nabla C_i(\mathbf{m}_0) \tag{2.11}$$

where $\nabla C(\mathbf{m})$ is the first-order derivative (or Fréchet derivative) of $C(\mathbf{m})$, and $\mathbf{H}$ usually called the Hessian matrix is the second order derivative of $C(\mathbf{m})$. If $\mathbf{H}$ is replaced by the identity matrix, the Newton's method degenerates into the *steepest descent method*. The problem now is turned into the determination of $\nabla C(\mathbf{m})$ and $\mathbf{H}$. By the numerical definition of $C(\mathbf{m})$ (equation 2.9), it is convenient to obtain the expressions

$$\nabla C(\mathbf{m}) = \left(\frac{\partial \mathbf{d}_{cal}}{\partial \mathbf{m}}\right)^t (\mathbf{d}_{cal} - \mathbf{d}_{obs}) = \mathbf{J}^t (\mathbf{d}_{cal} - \mathbf{d}_{obs}) \tag{2.12}$$

$$\mathbf{H} = \mathbf{J}^t\mathbf{J} + \mathbf{R} = \mathbf{H}_a + \mathbf{R} \tag{2.13}$$

where **J** is the Jacobian matrix of $C(\mathbf{m})$. Since the second term **R** of Hessian matrix is difficult to be obtained, the approximated Hessian matrix $\mathbf{H}_a$ is used instead, to give the solution corresponding to the *Quasi-Newton method*,

$$\Delta\mathbf{m} \approx -\mathbf{H}_a^{-1}\nabla C(\mathbf{m}_0) = -\left(\mathbf{J}^t\mathbf{J}\right)^{-1}\mathbf{J}^t\left(\mathbf{d}_{cal}-\mathbf{d}_{obs}\right) \tag{2.14}$$

A damping factor λ is further introduced into Equation 2.14 to balance the contribution of the approximated Hessian matrix (Marquardt, 1963), and then the solution corresponding to the *Gauss-Newton method* is expressed as

$$\Delta\mathbf{m} = -\left[\mathbf{H}_a+\lambda\,\mathrm{diag}(\mathbf{H}_a)\right]^{-1}\nabla C(\mathbf{m}_0) = -\left(\mathbf{J}^t\mathbf{J}+\lambda\,\mathrm{diag}(\mathbf{J}^t\mathbf{J})\right)^{-1}\mathbf{J}^t\left(\mathbf{d}_{cal}-\mathbf{d}_{obs}\right) \tag{2.15}$$

where $\mathrm{diag}(\mathbf{H}_a)$ represents the diagonal matrix consisting of the diagonal elements of $\mathbf{H}_a$. From this equation, we can see that the computation of Jacobian matrix **J** is the key to the Gauss-Newton method. In comparison with other gradient based methods, such as the steepest descent or the conjugate gradient methods, the Gauss-Newton method uses the term $\left[\mathbf{H}_a+\lambda\,\mathrm{diag}(\mathbf{H}_a)\right]^{-1}$ to precondition the searching direction in model space, which cannot only accelerate the convergence of misfit function significantly, but also balance the contributions of different model parameters.

In microseismic travel-time inversion, data vectors $\mathbf{d}_{obs}$ and $\mathbf{d}_{cal}$ turn to $\mathbf{T}_{obs}$ and $\mathbf{T}_{cal}$, and the objective equation 2.9 is re-written as Equation 3.2. Jacobian matrix **J** defined in Equation 2.12 is the partial derivative of synthesized arrival-time with respect to different model parameters,

$$\mathbf{J} = \frac{\partial\mathbf{d}_{cal}}{\partial\mathbf{m}} = \frac{\partial\mathbf{T}_{cal}}{\partial\mathbf{m}} \tag{2.16}$$

The synthesized arrival-time $\mathbf{T}_{cal}$ is calculated by ray tracing and can be theoretically expressed as a path integral from source to receiver,

$$T_{cal}(\mathbf{m}) = T_0 + \int_S^R \frac{1}{g(\mathbf{m})}ds, \tag{2.17}$$

where g is the group velocity, s is the ray path, T_0 is the triggering time of microseismic events. Taking the partial derivative of Equation 2.17 with respect to the l-th model parameter gives

$$\frac{\partial T_{cal}}{\partial m_l} = \frac{\partial T_{cal}}{\partial g}\frac{\partial g}{\partial m_l} = -\frac{1}{g^2}\frac{\partial g}{\partial m_l}ds \tag{2.18}$$

By recalling Equation 1.4, the relation between phase velocity v and group velocity g can be re-written as

$$\frac{g}{v}\,\boldsymbol{r}\cdot\boldsymbol{n} = 1 \tag{2.19}$$

where ***r*** is the ray vector that indicates the direction of group velocity, ***n*** is the wavefront normal vector that indicates the direction of phase velocity. Taking the partial derivative of Equation 2.19 with respect to the l-th model parameter yields

$$\frac{\partial g}{\partial m_l} = \frac{g}{v}\frac{\partial v}{\partial m_l} \tag{2.20}$$

By substituting Equation 2.20 into Equation 2.18, the elements of Jacobian matrix can be expressed as

$$\frac{\partial T_{cal}}{\partial m_l} = -\frac{1}{vg}\frac{\partial v}{\partial m_l}ds \tag{2.21}$$

For the layered transversely isotropic model used in this study (see Figure 2.1), the model parameter in each layer can be v_{p0}, v_{s0}, ε, δ, γ or c_{11}, c_{33}, c_{13}, c_{55}, c_{66}. The derivatives $\partial v/\partial m_l$ in Equation 2.21 can be directly derived from the analytical forms of phase velocity as shown by Equation 2.1~2.4 (see Appendix A). The phase velocity v and the group velocity g along the ray path, and the length of ray segments ds within each layer are computed by the ray-tracing algorithm. The dimensions of Jacobian matrix are determined by the number of microseismic records including P-, SH- and SV-waves and the total model parameters of all the layers.

Since the Gauss-Newton method is based on the quadratic approximation of non-linear problem, the model vector needs to be updated iteratively to make the objective function reaching the minimum point,

$$\mathbf{m}_{n+1} = \mathbf{m}_n + \Delta\mathbf{m} \tag{2.22}$$

The flow chart of Gauss-Newton based travel-time inversion used in this study is shown in Figure 2.6. The application of this method is presented in Chapter 3.

2.4.2 Global searching method

In this study, the fracture-induced anisotropy is represented by the normal and tangential fracture compliance Z_N and Z_T, and is assumed to be homogeneous within the fracture-bearing layers. Because the fractures mainly occur within the formation of high brittleness, the number of fracture-bearing layers is usually limited in microseismic application. Therefore, it is possible to make a global search for the optimal Z_N and Z_T which produce the minimum travel-time misfits for microseismic events.

Since the model space is very limited in this study, we do not use the advanced Mont-Carlo searching methods, such as genetic algorithm or simulated annealing algorithm, but a simple grid searching method. Although a global search for Z_N and Z_T in this approach is not computationally expensive, the physical constraints on the searching range are necessary. Solutions without physical meaning are dismissed even though they produce much less data residual. Laboratory measurements and theoretical modeling of fracture compliance provide rock physics constraints on the global search. The application example of this method is presented in Chapter 4.

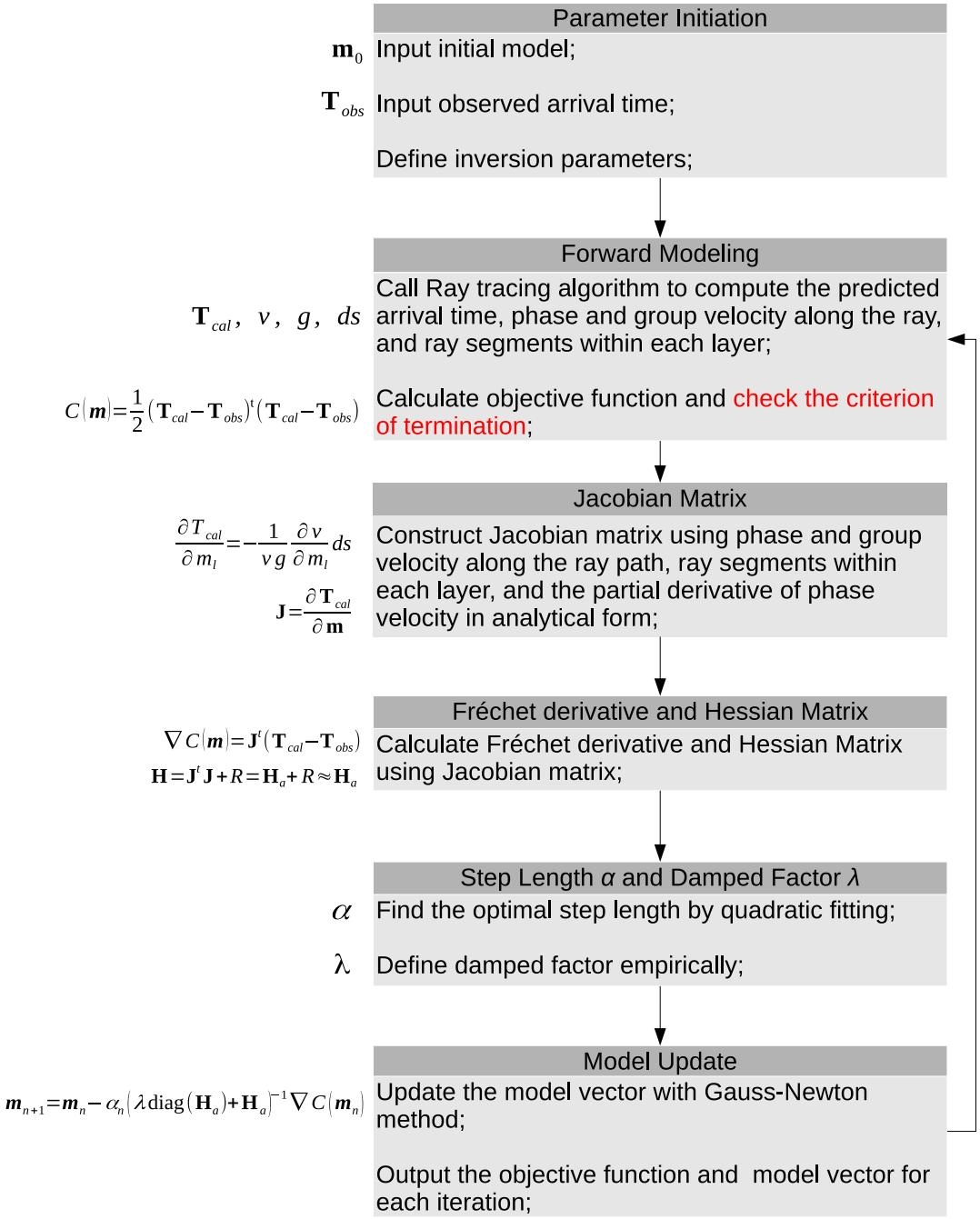

Figure 2.6: The flow chart of Gauss-Newton based travel-time inversion used in this study.

2.5 T_0 issues in microseismic inversion

T_0 is the triggering time of microseismic event and is also known as the origin time. When optimizing the velocity model and locating the seismic events, T_0 is needed to calculate the synthesized arrival-time (Eq. 2.17) and then to obtain the objective function (Eq. 3.2). If the accurate event location $\mathbf{S}$ and velocity model $\mathbf{m}$ are available, the true T_0 can be readily derived from the observed arrival-time T^{obs} and the calculated travel-time t^{cal} from source to receivers,

$$T_0^{(True)} = T^{obs} - t^{cal}(\mathbf{S}, \mathbf{m}) = T^{obs} - \int_{\mathbf{S}}^{R} \frac{1}{g(\mathbf{m})} ds \tag{2.23}$$

where t^{cal} is expressed using ray theory as a path integral. However, since the uncertainties in source locations and velocity model (i.e., $\Delta\mathbf{S}$ and $\Delta\mathbf{m}$) always exist either before or after the optimization, T_0 is commonly estimated by averaging the results obtained from all the arrivals of one event as

$$\begin{aligned} T_0^{(Average)} &= \frac{1}{N}\sum_{i=1}^{N}\left[T_i^{obs} - t_i^{cal}\left(\mathbf{S}+\Delta\mathbf{S}, \mathbf{m}+\Delta\mathbf{m}\right)\right] \\ &= \frac{1}{N}\sum_{i=1}^{N}\left[T_i^{obs} - \left(\int_{\mathbf{S}+\Delta\mathbf{S}}^{R} \frac{1}{g(\mathbf{m}+\Delta\mathbf{m})} ds\right)_i\right] \end{aligned} \tag{2.24}$$

where N is the number of all recorded arrivals of one event, $g(\mathbf{m})$ is the group velocity as a function of velocity model $\mathbf{m}$. By substituting the theoretical expression of T^{cal} (Eq. 2.17), the time residual ΔT expressed as a function of the perturbations of event location and velocity model can be written as

$$\begin{aligned} \Delta T_i(\Delta\mathbf{S}, \Delta\mathbf{m}) &= T_i^{cal}\left(\mathbf{S}+\Delta\mathbf{S}, \mathbf{m}+\Delta\mathbf{m}\right) - T_i^{obs} \\ &= T_0^{(Average)} + \left(\int_{\mathbf{S}+\Delta\mathbf{S}}^{R} \frac{1}{g(\mathbf{m}+\Delta\mathbf{m})} ds\right)_i - T_i^{obs} \end{aligned} \tag{2.25}$$

We can see that T_0 affects the time residual in a linear fashion, rather than in non-linear fashions as source location and velocity model do through the ray-path integral. The possible error introduced by the manner of computing T_0 (Eq. 2.24) can be straightly imposed on the time residual and bias the velocity model inversion and event location.

By expanding the term $t_i^{cal}\left(\mathbf{S}+\Delta\mathbf{S}, \mathbf{m}+\Delta\mathbf{m}\right)$ and recalling the definition of T_0 in Equation 2.23, Equation 2.24 can be re-written as

$$\begin{aligned} T_0^{(Average)} &= \frac{1}{N}\sum_{i=1}^{N}\left[T_i^{obs} - t_i^{cal}(\mathbf{S}, \mathbf{m}) - \Delta t_i^{cal}(\Delta\mathbf{S}, \Delta\mathbf{m})\right] \\ &= \frac{1}{N}\sum_{i=1}^{N}\left[T_0^{(True)} - \Delta t_i^{cal}\left(\Delta\mathbf{S}, \Delta\mathbf{m}\right)\right] \\ &= T_0^{(True)} + \Delta T_0\left(\Delta\mathbf{S}, \Delta\mathbf{m}\right) \end{aligned} \tag{2.26}$$

where

$$\Delta T_0\left(\Delta\mathbf{S},\Delta\mathbf{m}\right)=-\frac{1}{N}\sum_{i=1}^{N}\Delta t_i^{cal}\left(\Delta\mathbf{S},\Delta\mathbf{m}\right) \tag{2.27}$$

We can see that, the error ΔT_0 is controlled by the perturbations of source location $\mathbf{S}$ and velocity model $\mathbf{m}$. In the similar way, by integrating Equation 2.23 and 2.26, Equation 2.25 is simplified as

$$\begin{aligned}\Delta T_i(\Delta\mathbf{S},\Delta\mathbf{m}) &= T_0^{(Average)}+t_i^{cal}\left(\mathbf{S}+\Delta\mathbf{S},\mathbf{m}+\Delta\mathbf{m}\right)-T_i^{obs} \\ &= T_0^{(True)}+\Delta T_0\left(\Delta\mathbf{S},\Delta\mathbf{m}\right)+t_i^{cal}\left(\mathbf{S},\mathbf{m}\right)+\Delta t_i^{cal}\left(\Delta\mathbf{S},\Delta\mathbf{m}\right)-T_i^{obs} \\ &= \Delta T_0\left(\Delta\mathbf{S},\Delta\mathbf{m}\right)+\Delta t_i^{cal}\left(\Delta\mathbf{S},\Delta\mathbf{m}\right)\end{aligned} \tag{2.28}$$

The error ΔT_0 which is introduced by the manner of computing T_0 (Eq. 2.24) is imposed on the time residual in a straight manner. When searching the optimal velocity model or event location by minimizing the time residual, the coupling between ΔT_0 and $\Delta\mathbf{S}$, $\Delta\mathbf{m}$ as shown in Equation 2.27 can lead to a minimum time misfit for an incorrect velocity model and event locations (see for example Figure 2.10).

The validity of the conventional computation of T_0 (Eq. 2.24) is based on the assumption that $\Delta T_0\left(\Delta\mathbf{S},\Delta\mathbf{m}\right)$ tends to be zero,

$$-\frac{1}{N}\sum_{i=1}^{N}\Delta t_i^{cal}\left(\Delta\mathbf{S},\Delta\mathbf{m}\right)\rightarrow 0 \tag{2.29}$$

It means that, the errors of calculated travel-times from source to different receivers, which result from the small perturbations of event location and local velocity model (i.e., $\Delta\mathbf{S}$ and $\Delta\mathbf{m}$), should be uniformly distributed around zero. To satisfy this condition, the receivers should be uniformly scattered around the possible source locations in 3-D space. Receivers closely clustered in a particular direction can introduce significant errors of T_0 and ruin the velocity model inversion and event location. In microseismic applications (especially downhole microseismic monitoring), the receivers are usually deployed along the borehole and thus the aperture of observation is limited. T_0 issue in microseismic monitoring system with limited aperture is illustrated with an example in next section.

Another issue raised by the computation of T_0 happens when multi-waves are used in the velocity model inversion. Considering only P- and S-wave, the computation of T_0 (Eq. 2.24) is re-written as

$$
\begin{aligned}
T_0^{(Average)} =& \frac{1}{N_P + N_S}\left[\sum_{i=1}^{Np}\left(Tp_0\right)_i + \sum_{i=1}^{Ns}\left(Ts_0\right)_i\right] \\
=& \frac{1}{N_P + N_S}\left[\sum_{i=1}^{Np}\left(Tp_i^{obs} - tp_i^{cal}\right) + \sum_{i=1}^{Ns}\left(Ts_i^{obs} - ts_i^{cal}\right)\right] \\
=& \frac{1}{N_P + N_S}\left[\sum_{i=1}^{Np}\left(Tp_i^{obs} - \int_{\mathbf{S}+\Delta\mathbf{S}}^{R}\frac{1}{g(\mathbf{v}_p + \Delta\mathbf{v}_p)}ds\right)\right. \\
&\left. + \sum_{i=1}^{Ns}\left(Ts_i^{obs} - \int_{\mathbf{S}+\Delta\mathbf{S}}^{R}\frac{1}{g(\mathbf{v}_s + \Delta\mathbf{v}_s)}ds\right)\right]
\end{aligned}
\tag{2.30}
$$

where Tp^{obs} and Ts^{obs} are the observed arrival-times of P- and S-waves, tp^{cal} and ts^{cal} are the synthesized travel-times, N_P and N_S are the numbers of P- and S-wave arrivals, $\Delta\mathbf{S}$, $\Delta\mathbf{v}_p$ and $\Delta\mathbf{v}_s$ are the perturbations of source location and velocity model. We can see that, the possible errors of Tp_0 and Ts_0 in Equation 2.30 are controlled by the same source perturbation $\Delta\mathbf{S}$, but different velocity perturbations $\Delta\mathbf{v}_p$ and $\Delta\mathbf{v}_s$. The same source perturbation simultaneously affects the synthesized travel-time of P- and S-wave through ray-path integral, and the resulting errors of Tp_0 and Ts_0 are considered to be similar. However, different groups of parameters independently controlling the propagation of different waves, for example in TI media v_p, ε, δ controlling P-wave and v_s, γ controlling SH-wave, can be of different uncertainties, which may produce different errors of Tp_0 and Ts_0. Simply averaging the T_0 derived from different waves as in Equation 2.30 gives a trade-off between the data errors which result from the higher or lower uncertainties in different velocity parameters. In other words, the large time residual of S-wave caused by incorrect v_s can be transmitted to P-wave data through the computation of T_0 and then disrupt the inversion for v_p.

Figure 2.7 illustrates the influences of T_0 derived from different waves on the fitting of arrival-times. The event is from the microseismic dataset presented in Chapter 3. The synthesized travel-time is calculated using the same VTI model and the event location is fixed. The synthesized arrival-time in Figure 2.7(a) is obtained using the average T_0 of all three waves, while in Figure 2.7(b) using T_0 only from P-wave. We can see that, the shapes of branches consisting of synthesized P-wave arrivals match the time picks better than SH-wave, which means that the velocity parameters related to P-wave may have lower uncertainties than that related to SH-wave. However, as shown in Figure 2.7(a), a trade-off between T_0 that are derived from different waves shifts all the synthesized arrivals up, which enlarges the P-wave time misfit and reduces the SH-wave time misfit. The extra time misfit of SH-wave is transmitted to P-wave and will contaminate the inversion for the parameters controlling P-wave such as ε and δ. Therefore, the triggering time T_0 should be calculated using the data of minimal uncertainties, for instance only using P-wave data, rather than averaging the data with

the same weighting factor.

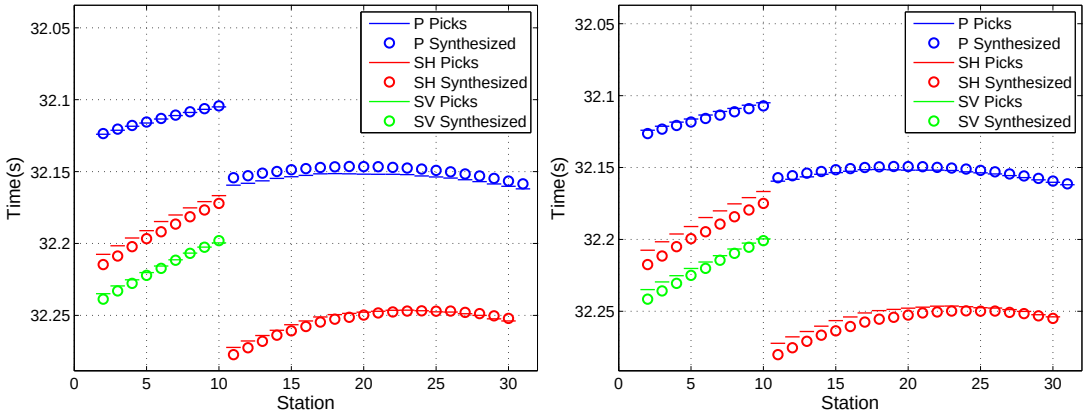

(a) T_0 derived from P-, SH- and SV-wave

(b) T_0 derived only from P-wave

Figure 2.7: The influence of triggering time T_0 computed in different manners.

2.6 Application example in coalbed methane reservoir

To verify the capability of the iterative gradient-based inversion for anisotropic velocity model and illustrate the T_0 issue in the configuration with limited aperture, an application example in a shallow coalbed methane reservoir is presented in this section (see Figure 2.8). Hydraulic-fracturing treatments are performed in two neighboring vertical wells. A single vertical well in about 200m away is equipped with eight three-component sensors to monitor the induced microseismic events. 18 perforation shots in two treatment wells are provided for calibrating velocity model. The data processing and interpretations of this project have been comprehensively presented in Hummel and Shapiro (2012), Reshetnikov et al. (2012a,b). This section only focuses on the estimation of transverse isotropy using the iterative gradient-based inversion and compares the results with the previous study which uses a grid searching optimization (see Reshetnikov et al., 2012b).

For the purpose of confidentiality, the location and geological background of the operating site are not provided by the operator, except the engineering data and sonic logs. Vp and Vs are derived from sonic logs and calibrated by perforation shots (see Figure 2.9). To test the isotropic velocity model, 18 perforation shots are relocated and the results are compared with the true locations (see Figure 2.10a). Large deviations from the true locations are observed which implies that seismic anisotropy should be taken into account in the velocity model. Weak transverse isotropy is demonstrated to be the factor resulting in the significant location misfit.

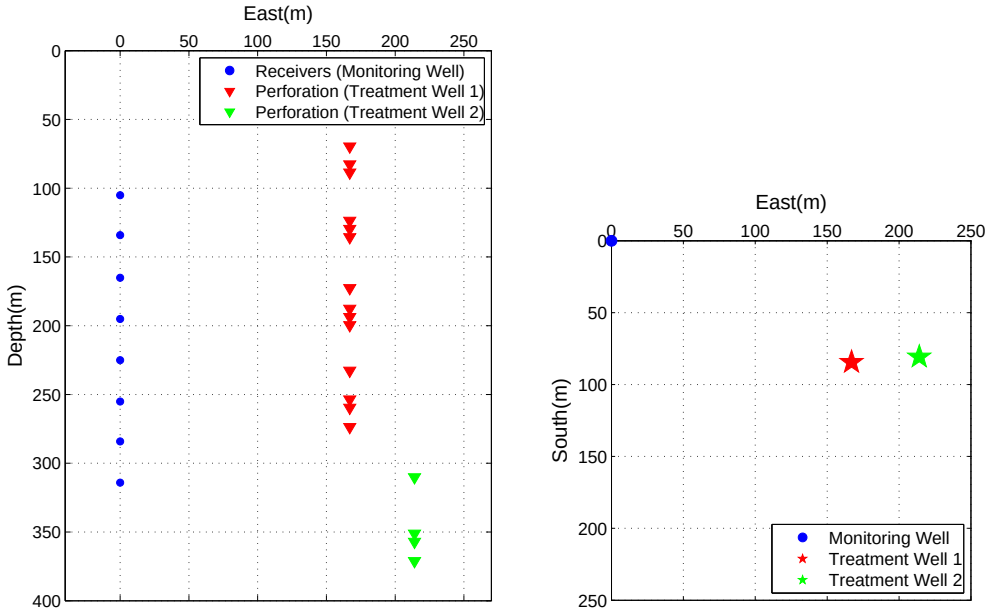

Figure 2.8: The configuration of downhole monitoring system in a shallow coal methane reservoir (left- section view, right- top view).

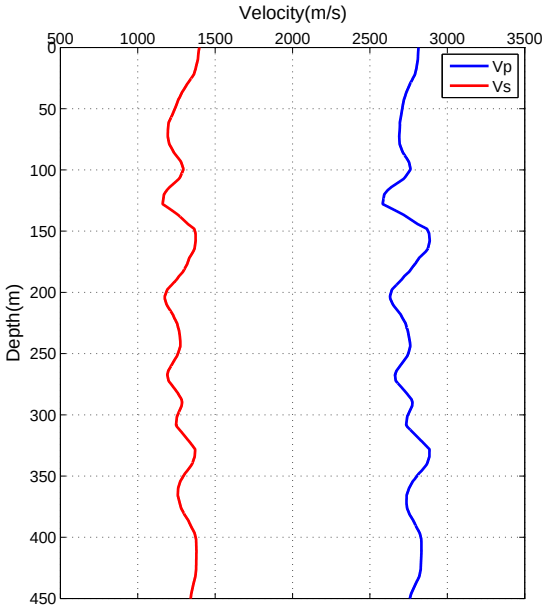

Figure 2.9: Vp and Vs derived from sonic logs and calibrated by perforation shots.

2.6.1 Illustration of T_0 issue in the configuration with limited aperture

As there is only a single vertical borehole array at a distance of about 200m from the treatment wells, the aperture of the observing system is very limited. T_0 issue could be an obstacle to the velocity model inversion and the source location in this

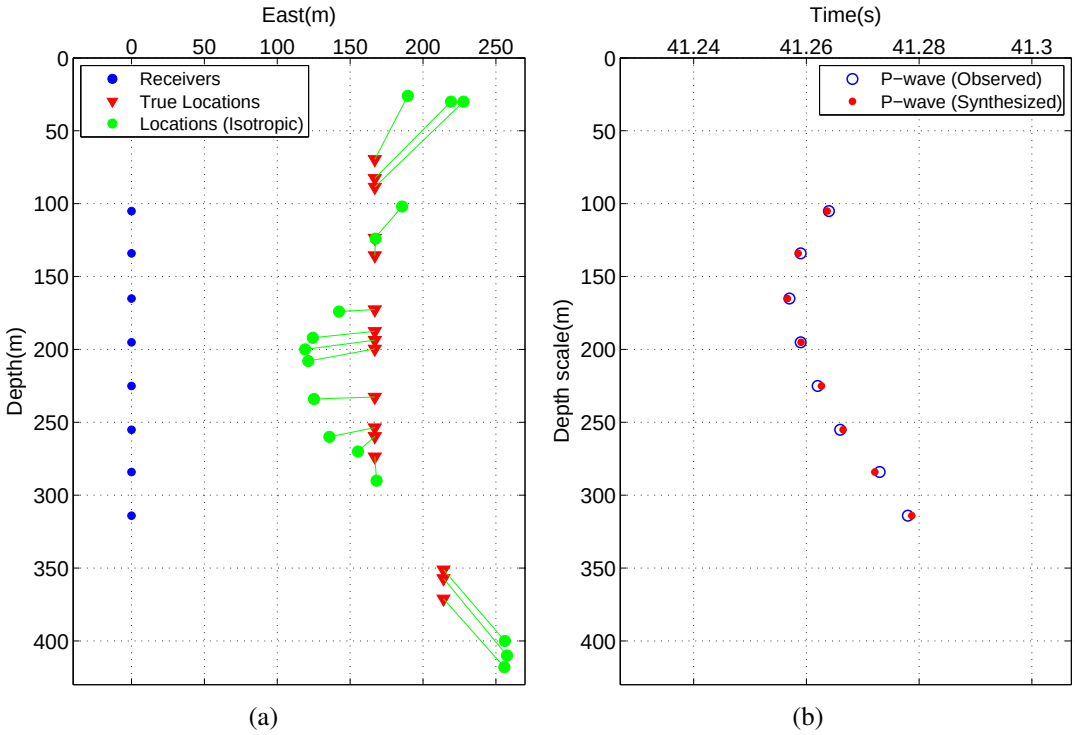

Figure 2.10: (a) Perforation shots relocated using the isotropic velocity model as shown in Figure 2.9; (b) The fitting between the observed and synthesized arrival-times for one mislocated perforation shots in Figure 2.10a.

case. As shown in Figure 2.10a, isotropic velocity model leads to poor locations duo to the absence of anisotropy. However, inaccurate velocity model and source locations do not produce significant time residual as expected in general cases. Figure 2.10b shows the fitting between the observed and synthesized arrival-times for one mislocated perforation shot in Figure 2.10a, in which we can see that the time misfits are not obvious at all. The strong coupling between ΔT_0 and $\Delta\mathbf{S}$, $\Delta\mathbf{m}$ revealed by Equation 2.27 in the configuration with limited aperture leads to a poorly estimated T_0, which can narrow the gap between the observed and synthesized arrival-times and reduce the time residual caused by the perturbations of velocity model and source locations. It is difficult to retrieve the optimal velocity model and the correct source locations using such biased time residual.

The definition of T_0 error in Equation 2.27 for one particular event can be expressed in differential form as

$$\Delta T_0\left(\Delta\mathbf{S},\Delta\mathbf{m}\right)=-\frac{1}{N}\sum_{i=1}^{N}\left(\frac{\partial t_i^{cal}}{\partial\mathbf{S}}\Delta\mathbf{S}+\frac{\partial t_i^{cal}}{\partial\mathbf{m}}\Delta\mathbf{m}\right) \tag{2.31}$$

where N is the number of all the recorded arrivals of this event. Given that the travel-time t^{cal} for the i_{th} arrival pertaining to this event can be expressed using ray theory

as a path integral,

$$t_i^{cal}(\mathbf{S}, \mathbf{m}) = \left(\int_{\mathbf{S}}^{R} \frac{1}{g(\mathbf{m})} ds \right)_i \tag{2.32}$$

taking the partial derivative of t_i^{cal} with respect to the source location **S** and the velocity model **m** yields

$$\frac{\partial t_i^{cal}}{\partial \mathbf{S}} = \frac{1}{g_s} = \textbf{Constant} \tag{2.33}$$

$$\frac{\partial t_i^{cal}}{\partial \mathbf{m}} = -\frac{1}{v_i g_i} \frac{\partial v_i}{\partial \mathbf{m}} ds_i \tag{2.34}$$

where g_s is the group velocity at the source point, v_i, g_i and ds_i are the phase velocity, group velocity and ray segment corresponding to the i_{th} arrival of the event, and Equation 2.34 is equivalent to Equation 2.21. We can see in Equation 2.31 that the perturbation of source location $\Delta\mathbf{S}$ contributes to the T_0 error through all the arrivals in the same linear way with a constant gradient, while the velocity perturbation $\Delta\mathbf{m}$ contributes in different nonlinear way for different arrivals. Therefore, the coupling between ΔT_0 and $\Delta\mathbf{S}$ are much stronger than that between ΔT_0 and $\Delta\mathbf{m}$. The uncertainties in source locations can result in significant T_0 error and bias the time misfit function of velocity model inversion.

To minimize the influence of T_0 in such configuration with limited aperture, microseismic events are not use in the inversion for anisotropic velocity model considering the strong coupling between T_0 error and the uncertainties in source locations. Only the perforation shots are used to implement a cross-well-style tomography.

2.6.2 Cross-well tomography of Thomsen parameters

Since the geological background of the operating sit is unknown, one cannot distinct different layers for velocity model inversion according to the stratigraphic and lithological information. Besides, considering another fact that the perturbations of Vp and Vs are both small and within narrow ranges (see Figure 2.9), Thomsen parameters are assumed to be homogeneous in the velocity model. As there are no S-wave arrivals recognized in perforation shot data, only Thomsen parameters ε and δ can be derived from P-wave information.

Two approaches using different criteria and different searching techniques are used to estimate Thomsen parameters ε and δ. Reshetnikov et al. (2012b) implement a grid searching optimization of Thomsen parameters by minimizing the location misfits of perforation shots which are shown in Figure 2.12a. The location misfits are color-coded and the coordinates of darkest area indicate the optimal ε and δ. In this study, an iterative Gauss-Newton based inversion is performed by minimizing the time residual of perforation shots which are fixed at the true locations (see Figure 2.11). The

optimized ε and δ lie exactly within the area of minimum location misfit (see Figure 2.12a). To compare with Figure 2.10a, the perforation shots are relocated using the optimal anisotropic velocity model and the retrieved locations are close to the true locations (see Figure 2.12b).

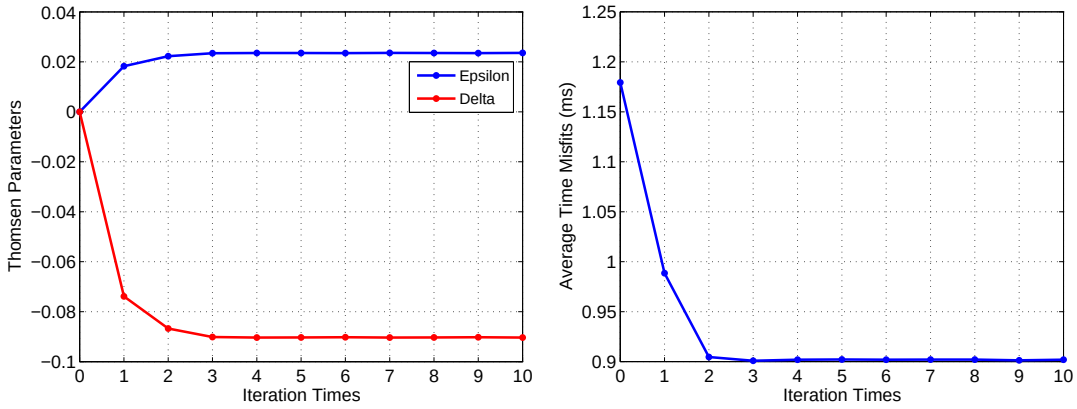

Figure 2.11: An iterative optimization of Thomsen parameter ε and δ by minimizing the time residual of perforation shots which are fixed at the true locations.

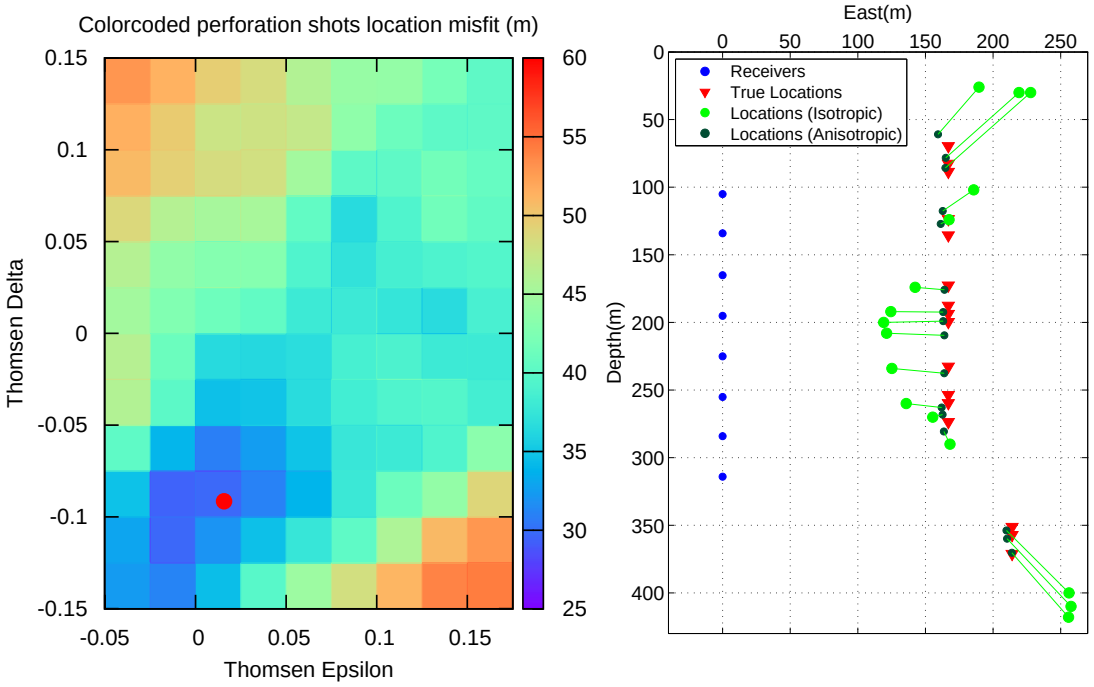

(a) (b)

Figure 2.12: (a) Comparison between the optimal Thomsen parameters obtained in this study (red dot) and the results of Reshetnikov et al. (2012b) (colored map); (b) The perforation shots relocated using the optimal anisotropic velocity model in comparison with that using the isotropic velocity model.

2.7 Discussion

This chapter presents the model definition, the forward modeling algorithm and the inversion strategies used to build the anisotropic velocity model using the downhole microseismic dataset. The singularity problem in the anisotropic ray-tracing algorithm and the issue of conventional computation of triggering time are analyzed and illustrated. An application example in a shallow coalbed methane reservoir is presented to verify the capability of the iterative gradient-based inversion and to further illustrate the T_0 issue in the configuration with limited aperture. The methods developed in this chapter are applied to a downhole microseismic dataset from Horn River shale gas reservoir to investigate the transverse isotropy caused by shale fabric and the fracture-induced anisotropy.

In the approach developed in this study, the model geometry is defined considering the limited spatial scale of downhole microseismic monitoring and the sedimentary background of unconventional reservoirs such as shale gas reservoirs. A layered model is used, within which the lateral heterogeneities are dismissed and the vertical gradients of elastic parameters are taking into account. For microseismic monitoring in complex geological setting, such as in Enhanced Geothermal System, the tilted layers or the presences of faults are possible, and then the lateral heterogeneity can be very strong. A blocked model or grid-node model should be the best options for that cases.

In this study, an anisotropic ray-tracing algorithm is employed to calculate the synthesized travel-time. This algorithm is based on the shooting method, which does not work properly in the vicinity of singular point. The singularity problem arises when the phase velocities of two shear-waves coincide at the singular points. This problem is more serous in heterogeneous anisotropic media or anisotropic media of lower symmetry class such as orthorhombic media. The proposed numerical strategies using the ray history can prevent the occurrences of singularity problem.

Based on Schoenberg's theory, the orthorhombic media is decomposed into the background TI media and the additional fracture set. This makes it possible to estimate the transverse isotropy and the fracture-induced anisotropy separately using different inversion methods. The multi-layer TI media is obtained by an iterative gradient-based method (the Gauss-Newton method). The Gauss-Newton method uses the damping factor and the approximated Hessian matrix to precondition the searching direction in model space, and can significantly accelerate the convergence of misfit function and stabilize the multi-parameter inversion. Fracture-induced anisotropy existing in a specific layer of high brittleness is described only by two parameters and therefore can be obtained by a global searching method.

The conventional manner of computing the triggering time (T_0) is based on the assumption of widely distributed receivers, which is usually not satisfied in realistic microseismic monitoring. The error of triggering time (ΔT_0) is controlled by the un-

certainties in source locations and velocity model. When the aperture of observation system is limited, a significant ΔT_0 is introduced and the time misfit functions of velocity model inversion and source location are then biased. The coupling between ΔT_0 and $\Delta \mathbf{S}$ are much stronger than that between ΔT_0 and $\Delta \mathbf{m}$. Besides the issue caused by poor configurations, when multi-waves are used in the velocity inversion, the conventional computation of triggering time can redistribute the time residual of different waves and bias the inversion for different velocity parameters.

Chapter 3

Estimation of shale anisotropy using downhole microseismic dataset: fabric anisotropy

3.1 Introduction

Microseismic technology has been rapidly developed along with the increase of production from shale gas reservoir. The basic application of microseismic monitoring is to map the spatial and temporal distributions and the mechanisms of hydraulically induce events. Shale usually exhibits transverse isotropy and azimuthal anisotropy due to the bedding-parallel fabric and the preferred-oriented fracture set. Shale anisotropy has strong impacts on microseismic data processing and interpretation, which can influence the locations of microseismic events, the inversion and interpretation of source mechanism and further affect the estimates of fracture geometry and stimulated volume. This chapter focus on estimating the fabric anisotropy (i.e., the intrinsic anisotropy) of shale using a downhole microseismic dataset from Horn River Basin, Canada. The fracture-induced anisotropy of shale will be addressed in the next chapter.

Although working with anisotropy has been widely acknowledged by microseismic community, there are only a few studies on extracting the velocity anisotropy from microseismic dataset. Grechka et al. (2011), Grechka and Yaskevich (2013, 2014) extended passive seismic tomography to estimate the triclinic anisotropy simultaneously with locations of microseismic events and applied this method to Bakken shale case. Li et al. (2013) extended the double-difference tomography to jointly invert microseismic location and VTI model. Verdon et al. (2009), Verdon and Kendall (2011), Wuestefeld et al. (2011) developed an approach to imaging the sedimentary fabric and fracture characteristics using shear-wave splitting in microseismic observations. Michel and Tsvankin (2014, 2015) attempt to use waveform inversion to derive the VTI model and the source parameters of microseismic event. These approaches are

mainly adapted from the techniques developed for the regional seismic monitoring or reflection seismic survey. In microseismic applications, the spatial scale of the target area is relatively small and the detailed geological and geophysical investigations around the target have usually been carried out. Large amounts of geological data are available for the estimation of anisotropy using microseismic dataset. However, the geological data have not been fully used in previous studies.

The fabric anisotropy of shale is usually characterized by transversely isotropic model and has the strongest impact on seismic applications. In recent decades, there have been many laboratory measurements of the fabric anisotropy of shales and rock physics studies on the relationships between the fabric anisotropy and the mineral compositions or organic matter in shale. At the core scale, the fabric anisotropy of shale is caused by the alignment and lamination of softer and platy clay minerals and kerogen (Johnston and Christensen, 1995; Vernik and Liu, 1997; Sone and Zoback, 2013a). In contrast, the stiffer and non-platy quartz grains can prevent the fabric alignment and significantly weaken the fabric anisotropy of shale (Curtis et al., 1980). However, these rock physics studies on the fabric anisotropy of shale have not been extensively integrated into the velocity model building in microseismic applications as is commonly done in reflection seismic cases.

In this chapter, the geology- and rock physics-oriented approach of constructing anisotropic velocity model developed in previous chapters are applied to a downhole microseismic dataset acquired in a shale gas reservoir. The geological analyses and experimental studies are deeply involved and highlighted in this working flow. They play crucial roles in building the initial model, minimizing the uncertainties and evaluating the results. Besides, the fabric anisotropy of shale obtained from downhole microseismic dataset is compared with laboratory measurements, to show the possible contributions of downhole microseismic monitoring as a quasi in-situ experiment to the understanding of subsurface anisotropy.

This chapter is initiated by a comprehensive review of geological background and laboratory measurements of shale anisotropy. An initial model for further optimization is obtained by integrating the geological analyses and experimental studies. Then an overview of the dataset used in this study is presented. After shortly introducing the methodology, the optimized fabric anisotropy of Horn River shales is shown and the results are compare with laboratory measurements of other shale samples. The improvements of the time misfits and event locations before and after the optimization are also discussed.

3.2 Geological analyses

Since the hydraulic fracturing are usually carried out after borehole geological and geophysical investigations, a full package of geological data are available for micro-

seismic data processing and interpretation. Geological analyses of Horn River shales help to define a reasonable initial model of fabric anisotropy for further optimization. Stratigraphic setting separates the layers of different properties and provides the frame of model geometry. Sonic logs give the elastic parameters in vertical direction. Core analyses reveal the fundamental information such as mineral compositions and organic content which are extremely important for the rock physics modeling and interpretation of the results. Unfortunately, the first-hand geological data from the operator is not available to us. Most of the contents in this section are based on the information collected from the publications and open documents.

3.2.1 Stratigraphic setting

The microseismic dataset under consideration is acquired during the hydraulic-fracturing operation carried out in Horn River Basin, Northeastern British Columbia, Canada. The targets of fracturing operation are the organic-rich shale formations (Muskwa, Otter Park and Evie) with TOC (Total Organic Carbon) up to 6 wt.% (Ness et al., 2010; Chalmers et al., 2012). The fractured reservoirs are overlain by about 800m thick clay-rich and organic-lean shales of Fort Simpson Formation (BC Ministry of Energy and Mines, 2005), where exactly the receiver arrays are deployed (see Figure 3.1). All the formations are near-horizontal within the spatial scale of downhole microseismic monitoring. For the three-stage microseismic dataset provided by the operator, the event clouds are mainly restricted within the Muskwa and upper-middle Otter Park formations. The overlying Fort Simpson shale and underlying lower Otter Park shale with higher clay content as well as a thin carbonate layer serve as fracture barriers (see Figure 3.1).

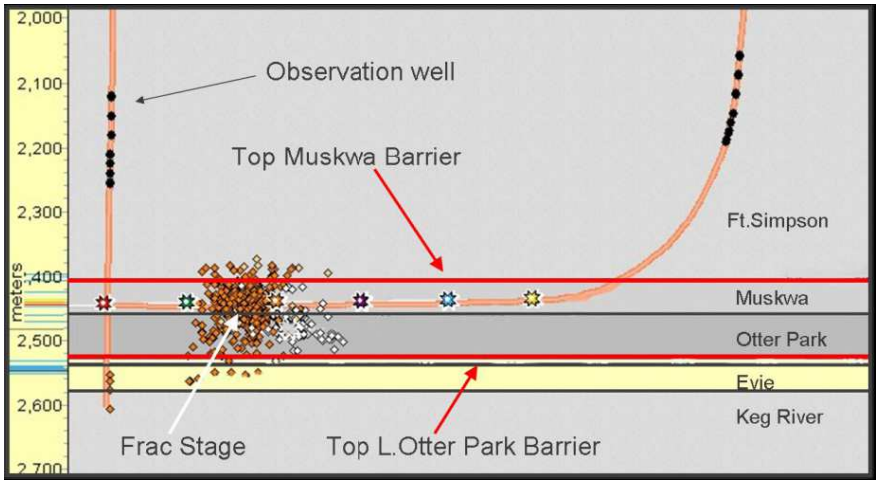

Figure 3.1: Stratigraphic setting and sketch of microseismic monitoring system in Horn River shales (after Dunphy and Campagna, 2011).

3.2.2 Sonic logs

Figure 3.2 shows the sonic logs from a nearby well in study area. To illustrate the elastic properties of different layers, the receiver arrays and event clouds are projected on the depth axis. We can see that, the shale gas reservoir is characterized by high Vp and Vs, low Vp/Vs ratio and low density, which is completely opposite to the upper and lower shale formations serving as fracture barriers. The overlying thick clay-rich formation within which the receiver arrays are deployed shows near-constant Vp, Vs and density, which imply that it is relatively homogeneous in depth compared to underlying formations. The wide range variations of elastic properties are closely related to mineral composition of shale. By integrating the stratigraphic setting, the basic frame of velocity model can be constructed.

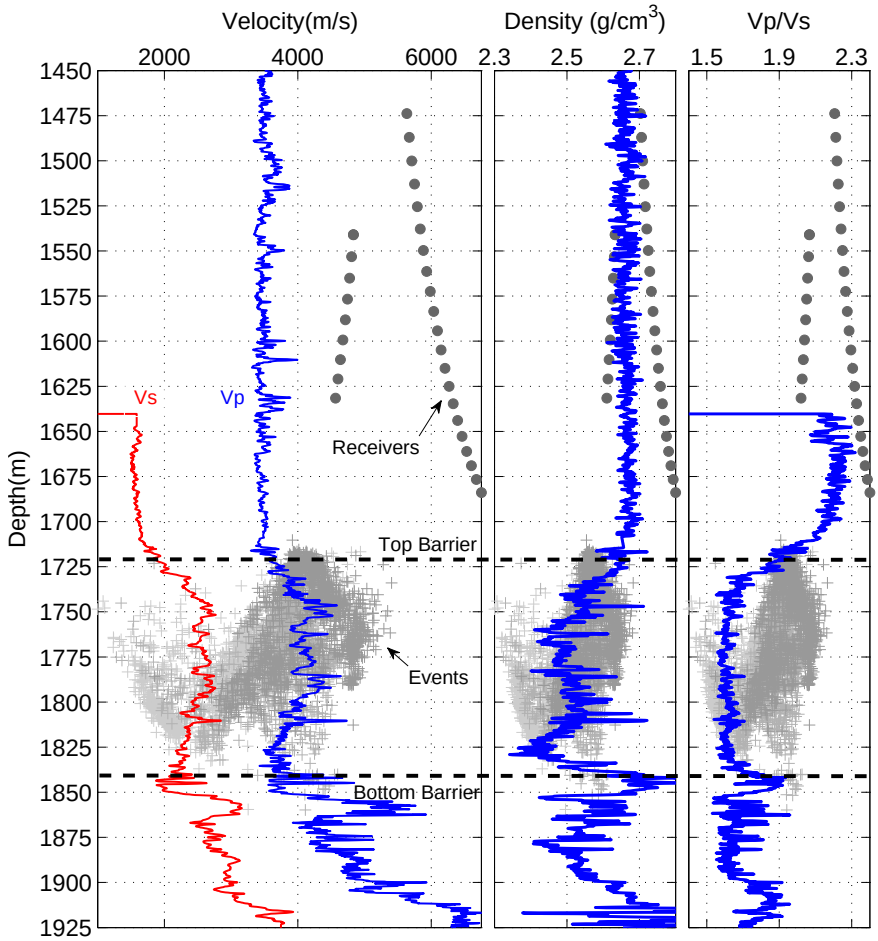

Figure 3.2: Sonic logs of Horn River shales from an offset well in study area. Receiver arrays and event clouds are projected on the depth axis with compressed lateral scale.

3.2.3 Core analysis

Core analyses provide the fundamental information of shale such as mineral compositions and organic content. Clay, quartz and carbonate are three major minerals of shale, of which the relative contents vary greatly for different shale samples. Since the core data of our target wells is unavailable, we collect the published core data of Horn River shale samples from different surveys and make a ternary plot of clay, quartz and carbonate contents (Figure 3.3). The most distinct points that can be noticed are the dominant clay content in Fort Simpson shale (average 70%) and the quartz content in Muskwa shale (up to 87%), and the extremely low carbonate content for both formations. The upper Otter Park shale is slightly more argillaceous and the lower Otter Park shale contains even more clay and less quartz (Ness et al., 2010). The underlying Evie shale is more calcareous than the other two formations. Mineral composition is the geological source of the distinct elastic properties and can be used to predict elastic parameters via experimental studies and rock physics models.

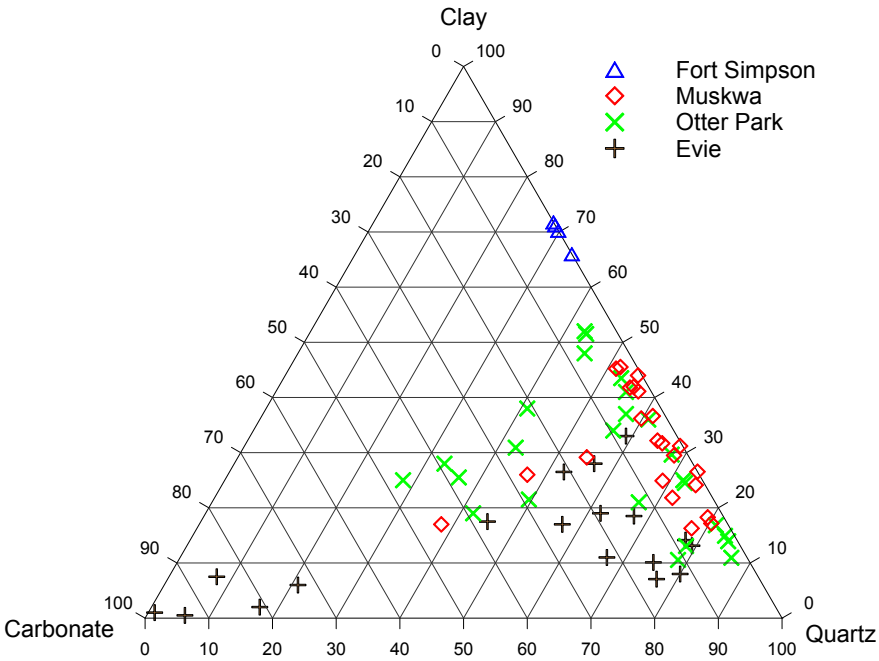

Figure 3.3: Ternary plot of clay, quartz and carbonate contents for Horn River shales (Data from Ross and Bustin, 2008; Chalmers et al., 2012; Harris and Dong, 2013).

3.2.4 Summary

The geological information of Horn River shales is summarized in table 3.1 for clarity and further applications. This information provides important guidance for the definition of anisotropic velocity model. Considering the wide range variations of elastic

properties as observed in well logs, a piecewise continuous model is used (see Figure 3.11), within which the vertical gradients of elastic parameters are kept, rather than a stair model with constant elastic properties in each layer. The thick clay-rich shale formation which serves as the upper fracture barrier is assumed to be a homogeneous layer because of the near-constant elastic properties as shown in sonic logs (see Figure 3.2). The mineral compositions directly controlling the fabric anisotropy of shale play a crucial role when building the initial model and evaluating the results of optimization.

Table 3.1: Summary of the geological information about Horn River shales. The values of mineral contents and TOC are the weight fractions.

	Formation	Clay	Quartz	TOC	Velocity	Vp/Vs	Density
Upper Fracture Barrier	Fort Simpson	70%	28%	<1%	low	high	high
Fractured Reservoir	Muskwa	25%	70%	5%	high	low	low
	Upper Otter Park	30%	60%	4%	media	low	low
Lower Fracture Barrier	Lower Otter Park	40%	50%	2%	low	media	high
	Thin Carbonate	/	/	/	high	media	high

3.3 Fabric anisotropy of shale

The primary source of shale anisotropy are the bedding-parallel alignments of clay mineral as well as kerogen particles in organic-rich shales, which usually cause the fabric anisotropy (i.e., the intrinsic anisotropy) of shale. Another important source of shale anisotropy are the preferred-oriented fractures at the scales much larger than grains or pores. These fractures are generally induced by the local stress field and mainly result in azimuthal anisotropy. Fine scale lamination of shales with different stiffness can also introduce a layering anisotropy, which is much weaker than the first two types of anisotropy. This chapter only focuses the fabric anisotropy of shale, which is usually represented by transverse isotropic (TI) model and has the strongest impact on microseismic applications. Laboratory measurements of the fabric anisotropy and its relationship with mineral compositions of shale are reviewed in this section. The experimental knowledge is used to build the initial model, constrain the inversion and evaluate the results.

3.3.1 Fabric anisotropy VS clay and kerogen

Clay minerals can be well organized by the strain-induced rotation during compaction because of the low aspect ratio (Curtis et al., 1980). It has been quantitatively demonstrated by X-ray diffraction techniques that a strong positive correlation exists between the degree of clay mineral alignment and the fabric anisotropy of shale (see Figure 3.4a). The electron and optical microscope image of shale fabric also support this point in a qualitative manner (Johnston and Christensen, 1995; Sone and Zoback, 2013a). Under the condition of similar compaction history, the fabric anisotropy of shale increases with the relative content of clay minerals.

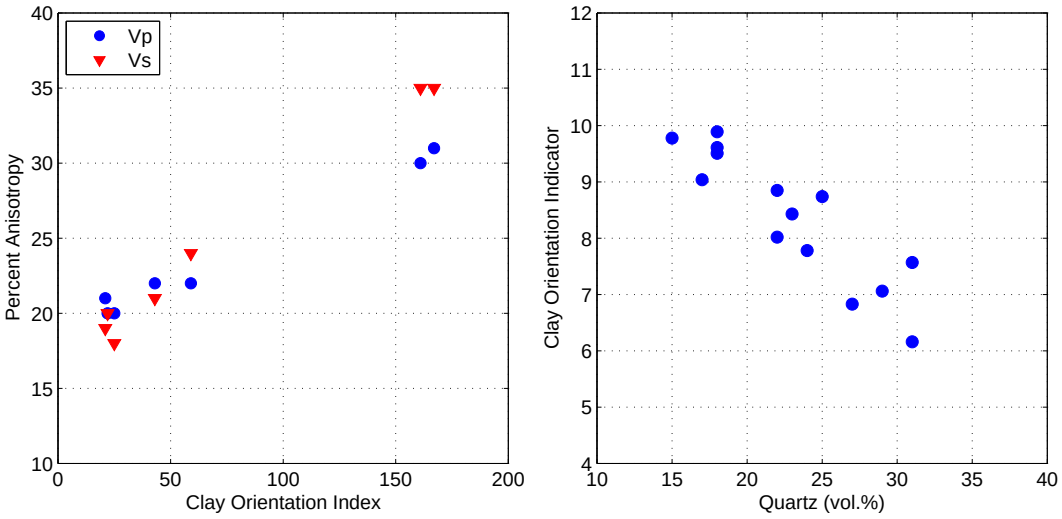

(a) (b)

Figure 3.4: The influences of clay alignment and quartz content on the fabric anisotropy of shale. Data from (a) Johnston and Christensen (1995) and (b) Curtis et al. (1980).

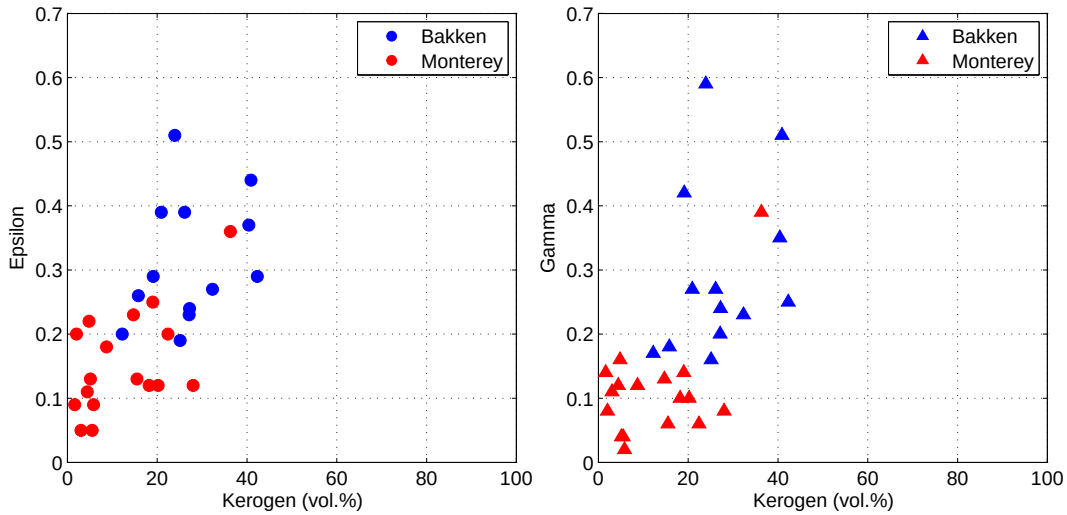

Figure 3.5: Relationships between the fabric anisotropy of shale and kerogen content. Data from Vernik and Liu (1997).

Studies by Vernik and Nur (1992), Vernik and Liu (1997) and Sondergeld et al. (2000) suggest a strong correlation between the elastic anisotropy of shale and organic richness (see Figure 3.5). In organic-rich shale, kerogen exhibits as lenticular microlayers dispersed among clay matrix and sporadic lamination in bedding-parallel direction as the petrographic and SEM observations show (Vernik and Nur, 1992; Vernik and Landis, 1996). The extremely compliant elastic properties of kerogen result in much larger decrease of seismic velocity in the bedding-normal direction than in the

bedding-parallel direction, and thus cause strong transversely isotropy. In addition, the hydrocarbon-generation induced microcracks further enhance the velocity anisotropy of organic-rich shales (Vernik, 1994).

As summarized by Hall (2000), most of North America's prospective gas shales as well as some non-source shales do not have so high TOC content and low clay content as Bakken shale samples (TOC 4.9%∼21%, Clay ∼5%) presented in Vernik and Nur (1992) and Vernik and Liu (1997). In the general cases, both clay mineral and organic matters contribute to the fabric anisotropy of shale and it is difficult to distinguish their influences. An alternative way is to investigate the correlations between velocity anisotropy and soft components of shale. As shown in Figure 3.6, the anisotropy of P- and S-waves are strongly correlated with the sum of clay and kerogen contents.

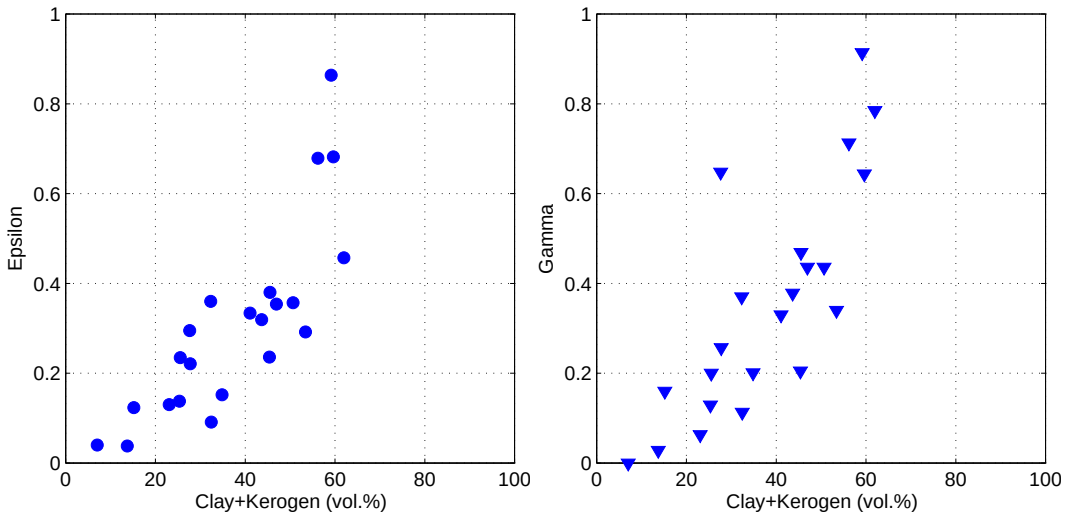

Figure 3.6: Relationships between the fabric anisotropy of shale and clay+kerogen contents. Data from Sone and Zoback (2013a).

3.3.2 Fabric anisotropy VS quartz

Curtis et al. (1980) measured the degree of clay mineral alignments in fine-grained sediments by X-ray techniques and found that it had a strong negative correlation with quartz content (Figure 3.4b). Observations of thin section images also find that the preferred clay orientation vanishes when clay content is too low (Sone and Zoback, 2013a). It can be interpreted that the quartz minerals with much stiffer and non-platy grains prevent the fabric alignment and disrupt the spatial continuity of compliant components (see Figure 1.7), and ultimately weaken the fabric anisotropy of shale. Therefore, the shale gas reservoir with high quartz content in Horn River Basin is expected to show much weaker fabric anisotropy.

3.3.3 Thomsen parameters of shale

The fabric anisotropy of shale is usually represented by the transversely isotropic model which is described by Thomsen parameters defined as,

$$\varepsilon = \frac{c_{11} - c_{33}}{2c_{33}} \qquad \gamma = \frac{c_{66} - c_{55}}{2c_{55}} \qquad \delta = \frac{(c_{13} + c_{55})^2 - (c_{33} - c_{55})^2}{2c_{33}(c_{33} - c_{55})} \tag{3.1}$$

Thomsen parameters ε and γ reflect the differences of elastic parameters in horizontal and vertical directions. ε controls the P-wave response and γ controls the SH-wave response. The similarities between ε and γ in mathematical form and physical means imply a possible correlation between them. Thomsen parameter δ with complex mathematical form has no clear physical meaning. It dominates the near-vertical P wave response in weak anisotropy case and controls the complexity of the wavefronts of P- and SV-waves, such as the cusps or triplications in the wavefront of SV-wave (Thomsen, 1986). Laboratory measurements of the fabric anisotropy of shale show that Thomsen parameters ε and γ are almost always positive and have a correlation with each other, while δ can be either positive or small negative and scatter in a narrow limit with no correlations with ε and γ (Figure 3.7). Vernik and Liu (1997) and Sayers (2005) try to attribute the sign variation of δ to the inter-particle microcracks or the degree of disorder in the orientations of clay minerals.

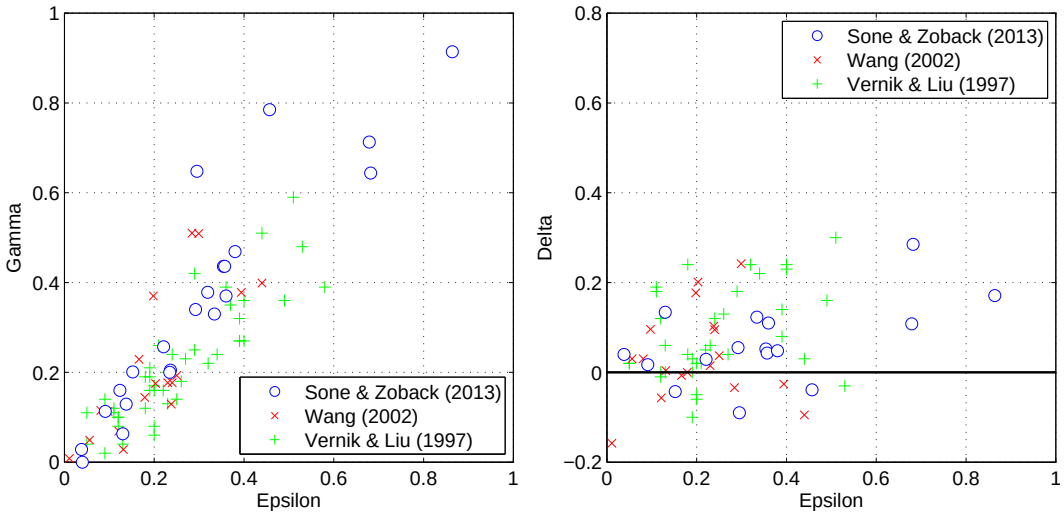

(a) (b)

Figure 3.7: Correlations between Thomsen parameters. Data from Vernik and Liu (1997), Wang (2002) and Sone and Zoback (2013a).

3.3.4 Initial estimate of fabric anisotropy in shale

Based on the geological analyses, Horn River shales have relatively simple mineral compositions which are dominated by clay and quartz minerals, and with minor car-

bonate. This makes it possible to predict the fabric anisotropy according to the experimental and theoretical studies. Shale gas reservoirs (Muskwa, Upper Otter Park) with extremely high quartz content and low clay content are expected to exhibit much weaker fabric anisotropy than the overlying and underline clay-rich fracture barriers. The core analyses also support this point with observations that Horn River gas-bearing shales are weakly laminated in core scale (Ness et al., 2010; Chalmers et al., 2012).

According to the semi-quantitative relationships between the fabric anisotropy of shale and clay+kerogen contents revealed by laboratory studies (Figure 3.6), we can preliminarily estimate the Thomsen parameters of Horn River Shales only based on the volume fraction of clay+kerogen (Table 3.2). This preliminary model completely derived from the geological and experimental analyses is used as the initial model in further optimization.

Table 3.2: Initial estimates of Thomsen parameters for Horn River shales. Note: The values of clay+kerogen volume fraction are not measured in core samples, but approximately calculated according to Table 3.1.

	Formation	Clay+Kerogen	ε	γ
Upper Fracture Barrier	Fort Simpson	65 vol.%	0.4	0.5
Fractured Reservoir	Muskwa & Upper Otter Park	35 vol.%	0.2	0.2
Lower Fracture Barrier	Lower Otter Park	45 vol.%	0.3	0.3

3.4 Data and methodology

3.4.1 Microseismic dataset

The microseismic dataset originates from a 143-stage, 8-well hydraulic fracturing project, among which three stages are provided for this studies (see Figure 3.8). Two downhole receiver arrays with 10 and 21 geophones are deployed above the fractured reservoir. A total number of 3646 events are located for the three-stage treatment. Additionally three perforation shots are provided for calibrating the velocity model. The configuration of this monitoring system is not perfect as the azimuth aperture of receiver arrays being a bit narrow. To minimize the uncertainties, we do not take all the events as the input of inversion. In addition to three perforation shots, 13 events of high signal-to-noise ratio are selected manually from 10% events with largest moment magnitude as the candidates for anisotropic velocity inversion.

All the 13 events present extremely clear first-arrivals which are picked manually in seismograms. Due to the strong anisotropy of shale, shear wave splitting is clearly observed in seismograms (see Figure 3.9). The polarizations of P-, SH- and SV-waves

are analyzed using the method proposed by Jurkevics (1988). Figure 3.10 shows the polarizations and hodograms of three traces marked in Figure 3.9. The dominant polarizations of SH-wave are within a near-horizontal plane, while the polarizations of P- and SV-waves are within a near-vertical plane. Polarizations of the three waves are nearly orthogonal to each other. According to the seismic responses of transversely isotropic media and orthorhombic media described in Section 1.2, these features imply that seismic responses in the monitoring system of this study are dominated by the vertical transverse isotropy resulting from the horizontal fabric alignments, rather than by the fracture-induced anisotropy.

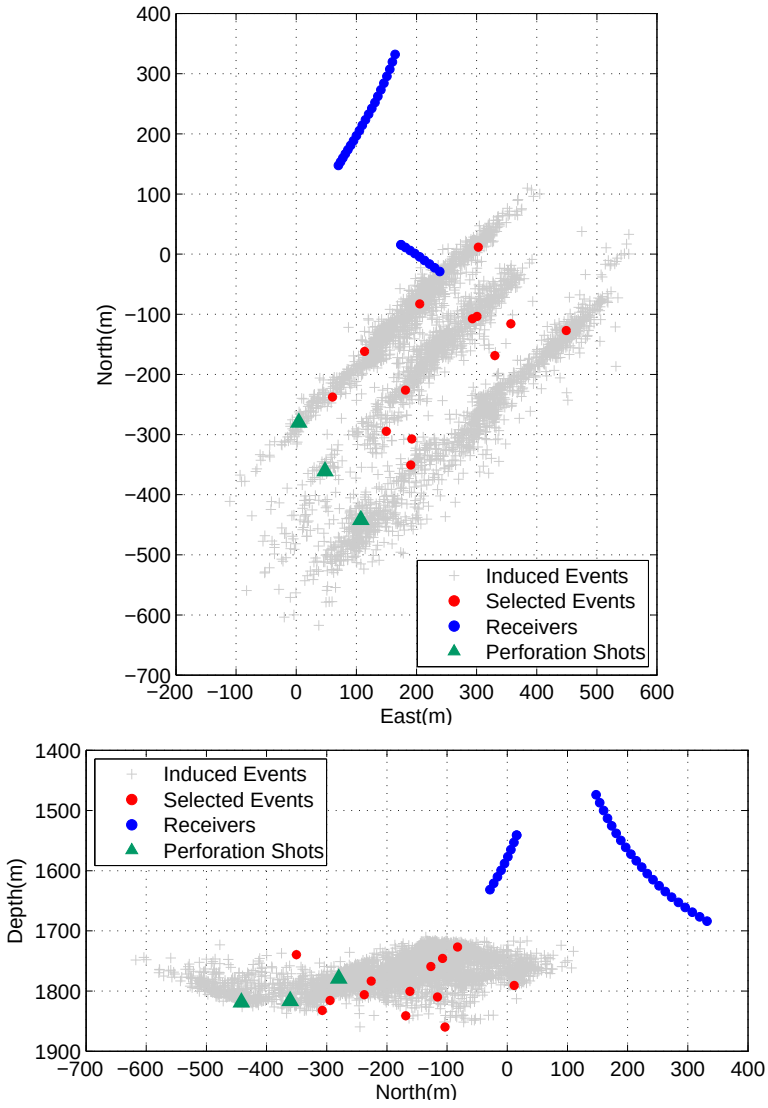

Figure 3.8: The monitoring system and microseismic events originally located by the data provider.

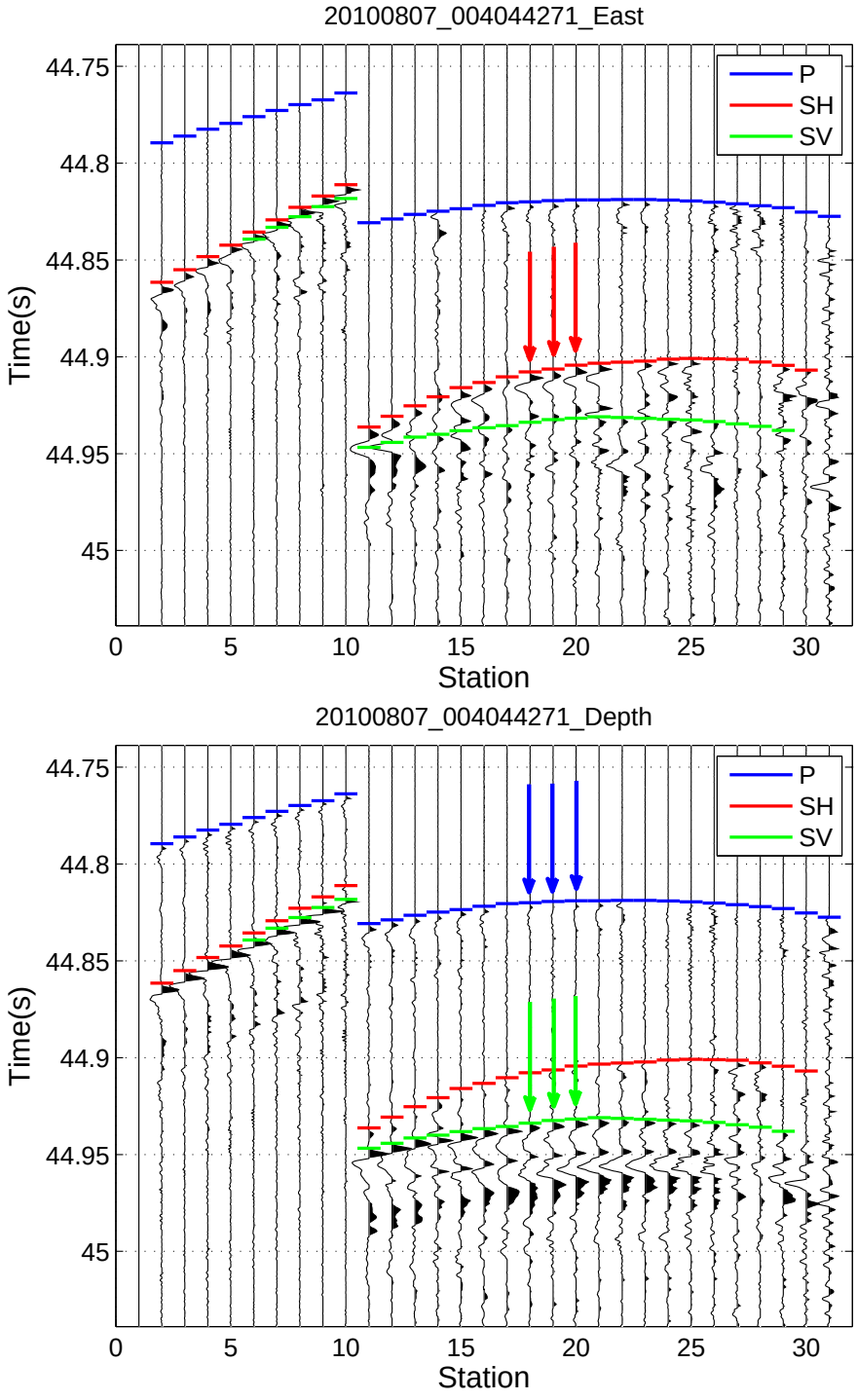

Figure 3.9: Seismogram of a selected microseismic event (top - east component; below - depth component).

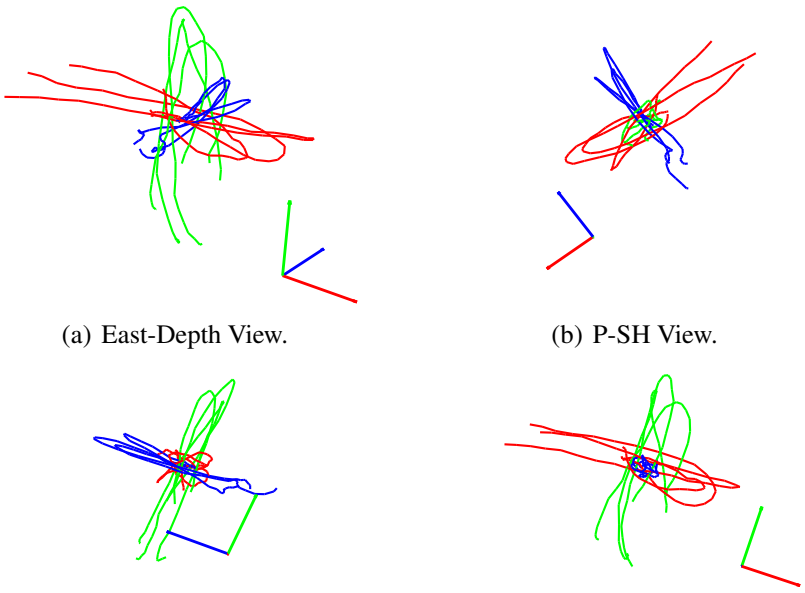

(a) East-Depth View. (b) P-SH View.

(c) P-SV View. (d) SH-SV View.

Figure 3.10: Polarization vectors and hodograms of P- (blue), SH- (red) and SV-waves (green) for the three traces marked in Figure 3.9. (a) is the section view from South to North direction;(b), (c), (d) correspond to the views from the polarization vectors of SV-, SH- and P-waves.

3.4.2 Methodology

Microseismic inversion for anisotropic velocity model is expressed as a nonlinear least-square problem with the misfit function

$$C(\mathbf{m}) = \frac{1}{2}\sum_{i=1}^{N}\left(T_i^{cal}(\mathbf{m}) - T_i^{obs}\right)^2 \tag{3.2}$$

where T^{obs} is the observed arrival-times, T^{cal} is the synthesized arrival-times and N is the number of recorded arrivals. Synthesized travel-time is calculated by an anisotropic ray-tracing algorithm which is highly modified from Gajewski and Pšencík (1987) (see Section 2.3). The inversion problem is solved by the Gauss-Newton method (see Section 2.4.1). The model vector $\mathbf{m}$ is updated iteratively by

$$\mathbf{m}_{n+1} = \mathbf{m}_n - \alpha(\lambda\,\mathrm{diag}(\mathbf{H}_a) + \mathbf{H}_a)^{-1}\nabla C(\mathbf{m}_n), \tag{3.3}$$

where λ is the damping factor, $\mathbf{H}_a$ is the approximated Hessian matrix, $\nabla C(\mathbf{m}_n)$ is the first order derivative (or Fréchet derivative) of the misfit function, α is the step length along the updating direction. The approximated Hessian matrix $\mathbf{H}_a$ and the damping factor λ are used to precondition the searching direction, which remarkably accelerate

the convergence of the misfit function and make the multi-parameter inversion more stable. The damping factor λ is empirically derived by trials and the step length α is determined by a parabolic searching procedure.
A 1D VTI model is used considering the limited spatial scale of downhole microseismic system and the sedimentary background of shale gas reservoir. The lateral heterogeneities within the layers are dismissed, while the vertical gradients of transverse isotropic parameters are kept when calculating the synthesized travel-time. The originally provided isotropic velocities v_{p0} and v_{s0} are derived from VSP survey and fit the sonic logs very well. To minimize the complexity of the inversion problem, v_{p0} and v_{s0} are not optimized further in the inversion, but fixed as given parameters. The model vector being updated iteratively consists only of Thomsen parameters of each layer [$\varepsilon^{(l)}$, $\delta^{(l)}$, $\gamma^{(l)}$]. Considering the coupling between hypocenter parameters and the velocity model in Equation 2.17, the source location (x, y, z) and the triggering time T_0 are not inverted simultaneously with Thomsen parameters, but updated at the beginning of each iterative step using the new velocity model.

Since there are two arrays with total 31 receivers in two inclined wells, the T_0 issue discussed in Section 2.5 due to the limited observing aperture is expected not to exist. Nevertheless, as all three waves are used in the velocity model inversion, the conventional computation of T_0 (Eq. 2.30) can result in a redistribution of time residuals between different waves as shown in Figure 2.7. Considering the relatively higher uncertainties in the velocity parameters related to S-waves, T_0 is calculated only using P-wave data in this study.

3.5 Optimization of fabric anisotropy

Figure 3.11 shows the process of optimizing Thomsen parameters, from the originally provided model to the finally optimized model. Firstly, the original model is assessed according to the experimental knowledge of the fabric anisotropy in shale as discussed in Section 3.3. In the original model, Thomsen parameters ε seems too small compared with δ, especially in the upper clay-rich shale formation which is expected to express strong fabric anisotropy. As the experimental studies show, Thomsen parameter δ scatter within a narrow range around zero and are generally smaller than ε especially in strong anisotropy range (e.g. in Figure 3.7b). In addition, there is a sharp increase of γ within a narrow depth interval, but no increase of ε, which is not physically reasonable considering the correlation between ε and γ (e.g. in Figure 3.7a).

Then, the initial model is constructed for further optimization according to the semi-quantitative relationships between the fabric anisotropy of shale and clay+kerogen contents revealed by experimental studies (see Table 3.2). With the geological and physical constraints, the unreasonable aspects in the originally provided model do not

exist in the initial model. An accurate initial model is essential to the nonlinear seismic inversion problem.

Finally, an iterative gradient-based inversion is implemented to obtain the optimal Thomsen parameters. As expected, the optimized model shows a large contrast of fabric anisotropy between clay-rich and quartz-rich shales. High fraction of clay mineral results in strong fabric anisotropy in the upper shale formation, whereas the quartz-rich shale gas reservoirs show much weaker fabric anisotropy. Thomsen parameter γ in the overlying shale formation seems to be a bit overestimated. The percentage of velocity anisotropy in Horn River shales can be up to 40%.

The optimization can also be illustrated by the decrease of time misfit between the observed and synthesized arrival-times (Figure 3.12). The originally provided model leads to the poorest match of first arrivals compared with the initial and optimal models, especially the mismatch of SV and SH arrivals due to the large δ and the unreasonable perturbation in γ curve (Figure 3.12a, b, c). With the geological and physical constraints, the initial model remarkably reduces the time misfit even without further optimization (Figure 3.12d). The optimal velocity model produces a good match of first arrivals and reduces the time misfit totally by about 65% compared to the original model.

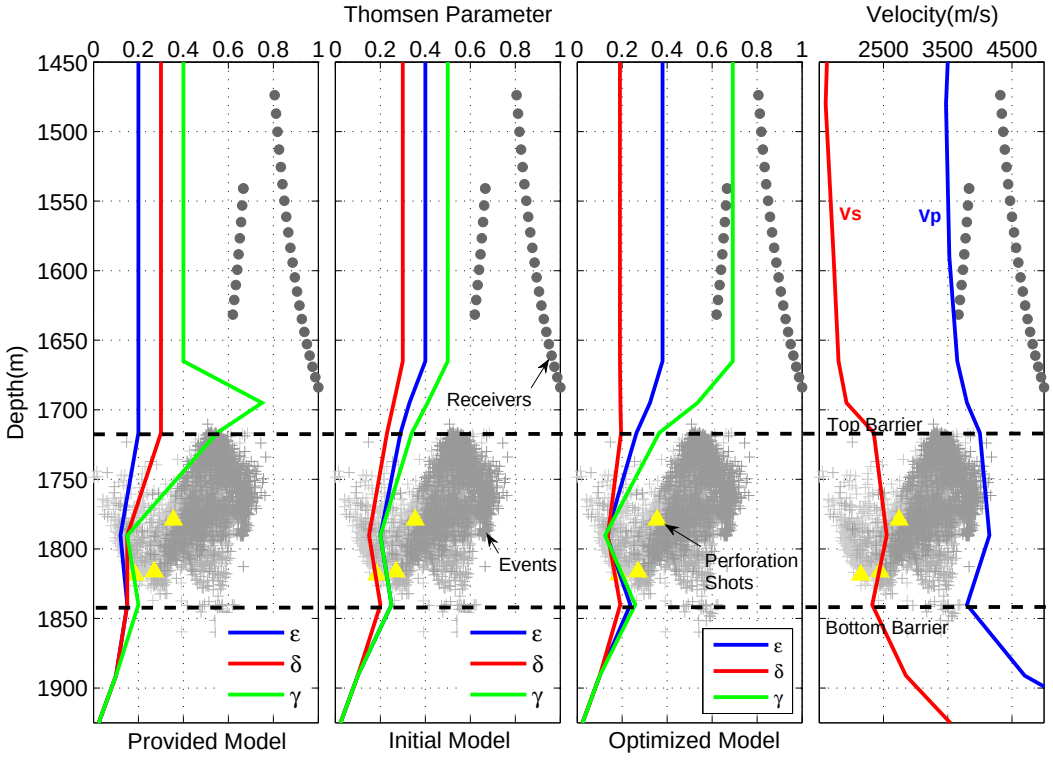

Figure 3.11: Originally provided transversely isotropic model (left), initial transversely isotropic model (middle) and optimized transversely isotropic model (right). Vp and Vs are fixed in the inversion.

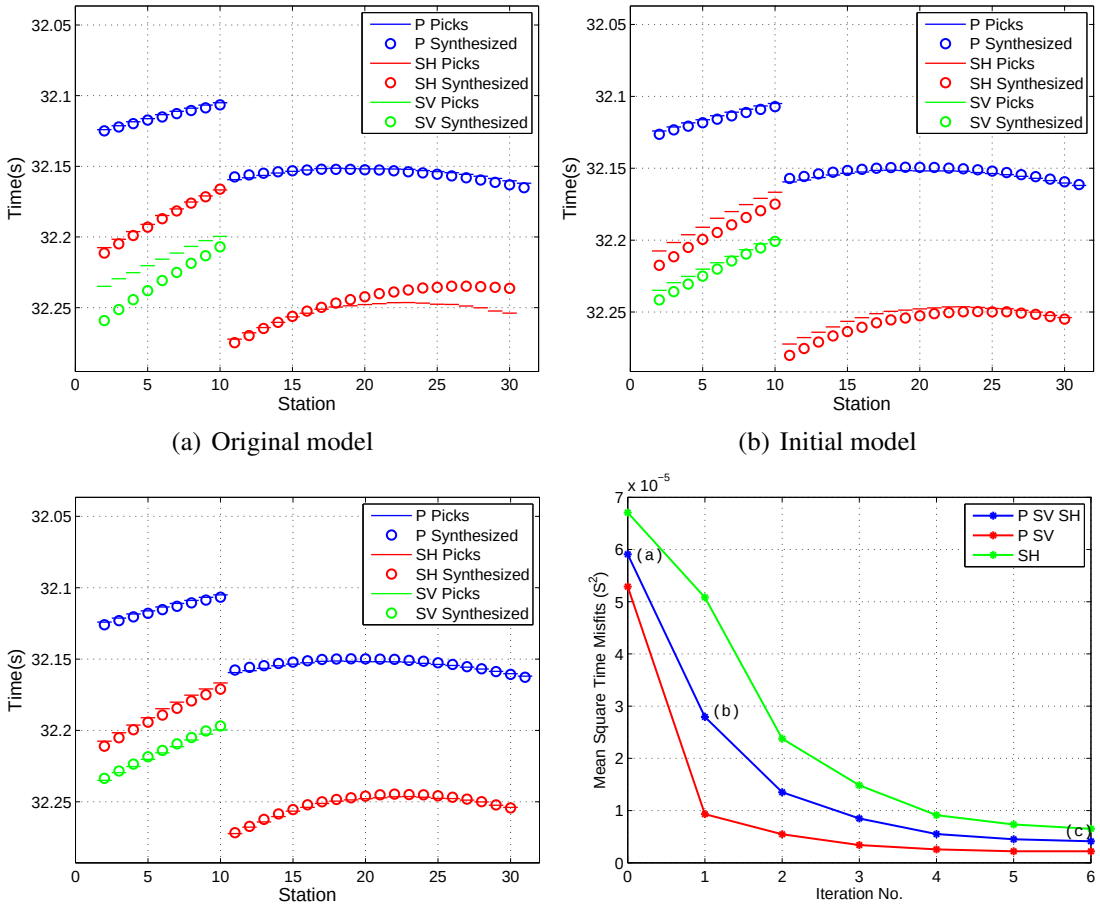

(a) Original model

(b) Initial model

(c) optimal model

(d) Time misfits VS Iteration

Figure 3.12: Time misfits of (a) original, (b) initial and (c) optimal anisotropic velocity models. Marked points a, b, c in (d) corresponding to the mean square time misfits of the three models.

3.6 Discussion

3.6.1 Time and location misfits

To evaluate the optimized fabric anisotropy of Horn River shales, microseismic events of one stage is located by the grid searching method. Figure 3.14 and 3.15 show the event locations corresponding to the initial model and the optimized model. The perforation shot is also relocated, to see how it fits the true location. In the map view, the event cloud shows a typical long-narrow shape with the perforation shot located at one end. In the section view, the events are sorted into two layers probably due to the mechanical stratigraphy (see Section 4.2.1). When the initial model is used, the relocated perforation shot deviates greatly from the true location either in horizontal or depth directions. After optimization, the relocated perforation shot is shifted much closer to the correct position especially in the depth direction, which means a significant improvement of the event locations.

Statistic distributions of time misfits also prove the improvements of event locations (see Figure 3.13). The average time misfit of event clouds is reduced by about 0.4ms after the optimization. The time misfits corresponding to the optimal model clearly show a more reasonable log-normal distribution which means time errors are randomly distributed around the average value.

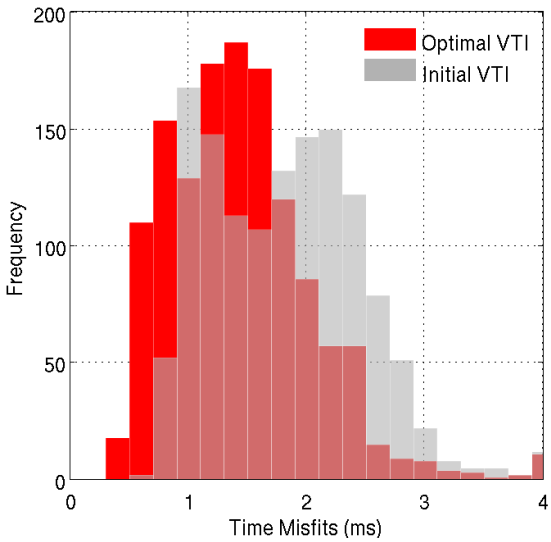

Figure 3.13: Time misfits of microseismic events corresponding to the initial and optimal VTI model in Figure 3.11.

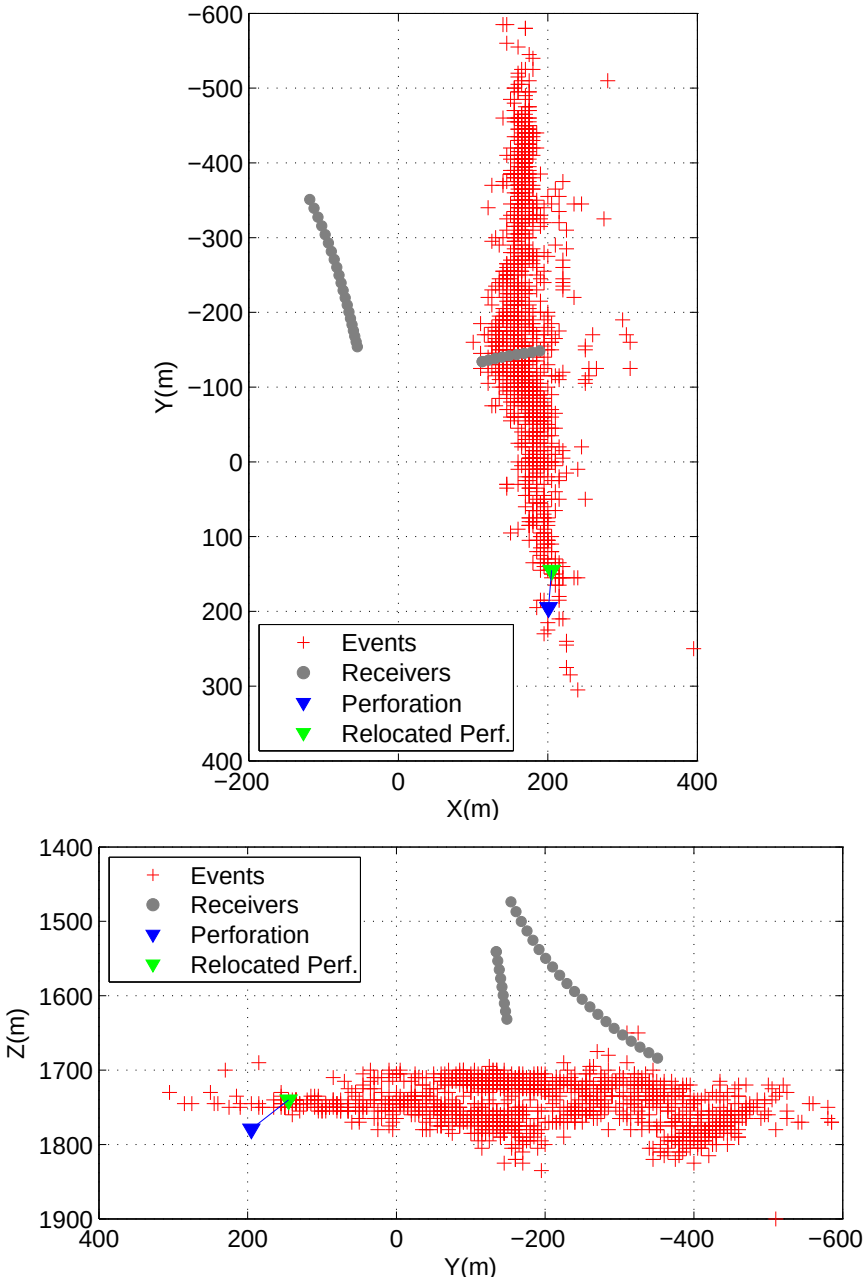

Figure 3.14: Event locations corresponding to the initial VTI model.

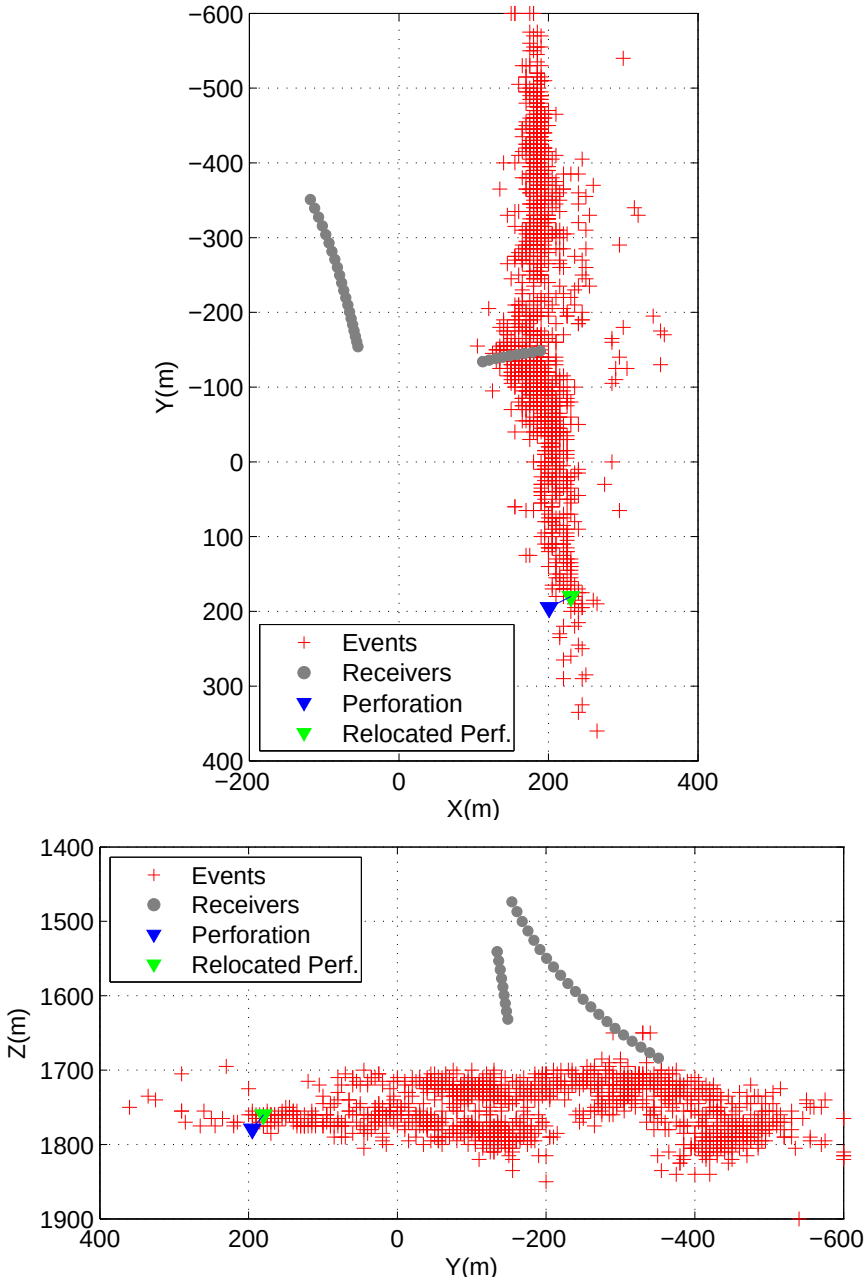

Figure 3.15: Event locations corresponding to the optimized VTI model.

3.6.2 Comparison with laboratory measurements

Since we do not have core samples of Horn River shale to perform a laboratory measurement, the fabric anisotropy derived from the downhole microseismic dataset in this study is compared with laboratory measurements of other shale samples (see Figure 3.16, 3.17). Being consistent with other shale samples, Thomsen parameter ε and γ of Horn River shales also show a strong positive correlation. The values are exactly within the narrow fan-shape area that is outlined by the experimental data, except the γ of the overlying shale formation which seems to be slightly overestimated. Thomsen parameter δ of Horn River shales are all positive and have no correlations with ε and γ. The values of δ scatter within a narrow range defined by experimental data and are generally smaller than ε especially in strong anisotropy range.

As observed in laboratory measurements, the degree of the fabric anisotropy in Horn River shales strongly depends on the clay+kerogen volume content. Although the value of clay+kerogen contents are approximately estimated from the published data (see Table 3.2), the positive correlations between ε, γ and clay+kerogen content are surprisingly consistent with the experimental measurements (see Figure 3.17).

3.7 Conclusion

In this chapter, the geology- and rock physics-oriented approach of constructing anisotropic velocity model developed in previous chapters are applied to the downhole microseismic dataset acquired in Horn River shale gas reservoir to investigate the fabric anisotropy of shale. The investigation is started from the geological analyses and experimental studies on the fabric anisotropy of shale, which play crucial roles in building the initial model, minimizing the uncertainties and evaluating the results. As in downhole microseismic system the receivers are deployed deeply within the formations and close to the sources, downhole microseismic monitoring can be considered a quasi in-situ measurement and provide reliable information of shale anisotropy. The fabric anisotropy of shale obtained from the downhole microseismic dataset is comparable with laboratory measurements. This demonstrates that the downhole microseismic monitoring, as a quasi in-situ experiment, has a potential to contribute to a better understanding of subsurface anisotropy beyond the laboratory.

Shale intrinsically exhibits transverse isotropy due to the bedding-parallel fabric, which has the strongest impact on the processing and interpretation of microseismic data. The fabric anisotropy of shale is usually represented by the transversely isotropic model and expressed in terms of Thomsen parameters. Laboratory measurements show that the degree of fabric anisotropy strongly depends on the fraction of softer components in shale, e.g. clay mineral and organic matter. The existence of quartz can prevent and interrupt the alignment and lamination of fabric and consequently weaken the fabric anisotropy of shale. Thomsen parameters ε and γ of shale

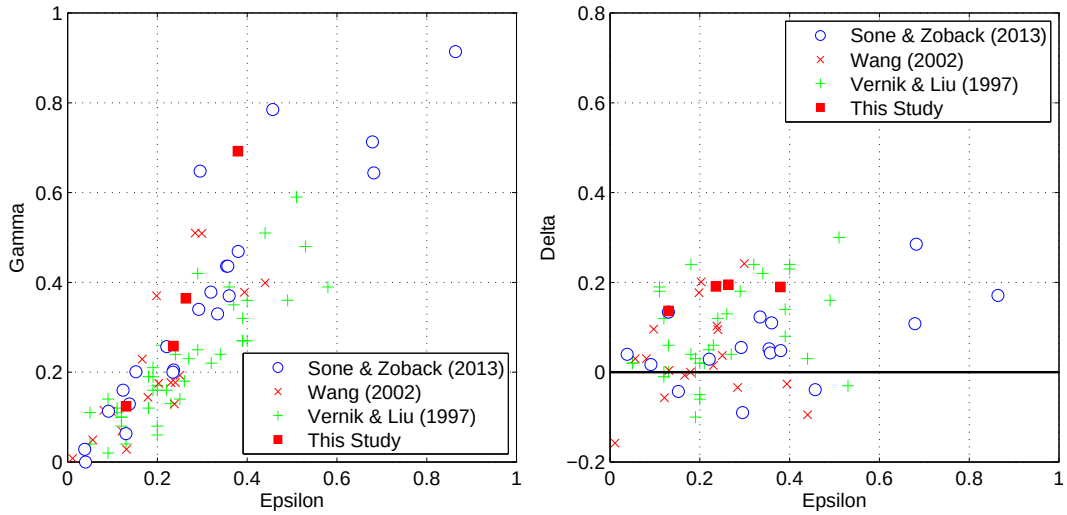

Figure 3.16: Correlations between Thomsen parameters of Horn River shales and other shale samples from different prospective plays. The solid squares correspond to the Thomsen parameters of the grid points at the depth of 1665m, 1717m, 1790m, 1840m in the optimized model (Figure 3.11).

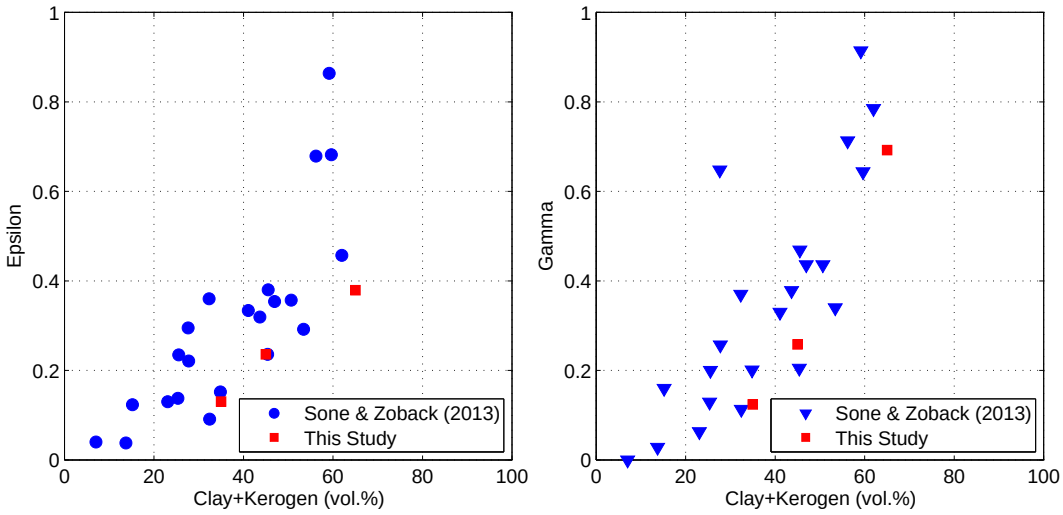

Figure 3.17: The influence clay+kerogen contents on the fabric anisotropy of Horn River shales and other shale samples from different prospective plays. The red squares correspond to the Thomsen parameters of the grid points at the depth of 1665m, 1790m, 1840m in the optimized model (Figure 3.11).

are always positive, and have a correlation with each other. Thomsen parameter δ scatter within a narrow range around zero and are generally smaller than ε and γ. In Horn River basin, the geological analyses show that, the mineral compositions of gas-bearing shales are dominated by the quartz content (up to 87%), while the overlying

shale serving as the fracture barrier is clay-rich (average 70%). By integrating the geological information and experimental studies, the fabric anisotropy can be initially estimated for Horn River shale. This preliminary model is used as the initial model in further gradient-based optimization.

The optimized model shows the expected large contrast of the fabric anisotropy between clay-rich and quartz-rich shales. High fraction of clay mineral results in strong fabric anisotropy in the upper Fort Simpson shale, whereas the quartz-rich shale gas reservoirs (Muskwa and Otter Park shales) show much weaker fabric anisotropy. The percentage of velocity anisotropy in Horn River shales can be up to 40%. The optimized VTI model remarkably reduces the time misfit by about 65% compared to the originally provided VTI model. Time misfits corresponding to the optimal model clearly show a more reasonable log-normal distribution which means randomly distributed errors. The event locations are significantly improved as the relocated perforation shot indicates. The fabric anisotropy of Horn River shales derived from the downhole microseismic dataset in this study is consistent with laboratory measurements of other shale samples.

Chapter 4

Estimation of shale anisotropy using downhole microseismic dataset: fracture-induced anisotropy

4.1 Introduction

As the primary technology to map the hydraulic fracturing in the development of shale gas, microseismic monitoring can delineate the spatial and temporal distributions of hydraulically induced events and determine the geometry of fracture-network. In additional, the downhole microseismic monitoring can provide more insights into the local properties of subsurface as a quasi in-site experiment. The previous chapter has shown how to obtain the fabric anisotropy of shale from a downhole microseismic dataset with the constraints of rock physics and geological analyses. Following the same philosophy, this chapter presents the estimation of the anisotropy induced by a preferred-oriented fracture set in shale using the same downhole microseismic dataset from Horn River Basin, Canada.

Natural fractures in shale are of different scales and most of them are sealed in the burial status (Gale et al., 2007, 2014). In hydraulic fracturing treatment, natural fractures can be reactivated and interact with the induced fractures, and thereby enhance the connectivity of fractured volume and significantly improving the efficacy of hydraulic fracturing (Fisher et al., 2004; Gale et al., 2007; Dahi-Taleghani et al., 2011). Whether sealed or not, the fracture represents a planar discontinuity in the host rock filled with fluid or cements, which exhibits mechanical compliance and reduces the velocity of seismic waves crossing it. If the fractures are aligned in a particular direction, the host rock can effectively display anisotropic properties. A preferred-oriented fracture set is another important source of shale anisotropy in addition to the clay minerals and organic matter. A common seismic response of the aligned fractures is the azimuthal anisotropy.

The occurrence of fractures is controlled by the mechanical strength of the rock which strongly depends on the mineral compositions. Thus, the fractures usually show a stratigraphic distribution due to the mechanical stratigraphy (Laubach et al., 2009; Gale et al., 2014). In shales, the fractures mainly occur within the quartz-rich or carbonate-rich formations of high brittleness rather than the clay-rich formations of high ductility (Sone and Zoback, 2013b). According to an extensive observations of cores and outcrops from different shale plays, the aligned vertical or sub-vertical fractures are most commonly presented in shale (Gale et al., 2014). Such fractures with high angle to the bedding plane are commonly recognized as the product of hydrofracturing process (Crampin and Atkinson, 1985; Cosgrove, 1998). A fracture opens more easily in the direction of minimum horizontal stress and the fracture strike is usually parallel to the maximum horizontal stress. Based on these characteristics of fracture distribution and fracture geometry in shale, a vertically fractured TI (VFTI) model is used to represent the combination of horizontally aligned fabric and a preferred-oriented vertical fracture set (Schoenberg and Helbig, 1997).

As a subset of orthorhombic model, the VFTI model can be described by nine independent stiffness coefficients. For the convenience of seismic applications or rock physics studies, several equivalent ways of describing orthorhombic media or fractured media have been introduced in recent decades from the point of view of effective media or seismic response (Hudson, 1981; Tsvankin, 1997). Under the assumption of linear-slip condition, the elastic behaviors of a fracture can be characterized by the compliance in the normal and tangential directions to the fracture plane without considering the physical details of fracture (Schoenberg, 1980; Schoenberg and Sayers, 1995). Then the effective stiffness of VFTI media can be conveniently obtained by imposing the excess compliance induced by vertical fractures on the stiffness of the background TI media. With clear physical meaning and physical dimension, the fracture compliance can be explicitly expressed in terms of physical parameters for different fracture models (e.g. Liu et al., 2000; Sayers and Kachanov, 1995), and also can be measured directly in laboratory and field (e.g. Lubbe et al., 2008; Hobday and Worthington, 2012). Theoretical modeling and experimental measurements provide the prior knowledge and physical constrains for the estimation of fracture compliance.

In the previous chapter, the background TI media representing the fabric anisotropy of shale has been obtained by a geology- and rock physics-oriented approach. The location and time misfits of microseismic events have been significantly improved. In this chapter, a similar approach is applied to the same microseismic dataset to extract the additional fracture-induced anisotropy from the remaining data residual. Geological analyses and rock physics are deeply involved in the working flow, which help to define the model, reduce the number of unknowns, narrow the searching space and interpret the results.

4.2 Characteristics of fractures in shale

Without considering the physical details, fractures can be simply represented as planar discontinuities in the rock. Most of natural fractures are sealed by mineral cements, in shale mostly by calcite (Gale et al., 2007, 2014). Such discontinuity is not bonded as closely as the intact rock and show more compliant properties which can result in elastic anisotropy. As the pre-existing planes of weakness and the possible fluid conduit, natural fractures in shale tend to be reactivated in hydraulic fracturing treatment and interact with the induced fractures to form a network (Fisher et al., 2004; Gale et al., 2007; Dahi-Taleghani et al., 2011). Fractures are generated independently or in combination by several mechanisms, including differential compaction, local and regional stress changes associated with tectonic events, strain accommodation around large structures, catagenesis of kerogens, or artificial fluid injection (Gale et al., 2014).

Characterizations of fracture distribution and fracture geometry are mostly based on sonic logs, cores, outcrops, image logs and local stress data. Mechanical parameters, such as Young's modulus, Poisson's ratio and Brittleness Index, can be derived from sonic logs, according to which one can predict the vertical distribution of fractures. The fracture geometry can be directly observed in cores, outcrops and image logs, even though the spatial sampling of such observations is limited. Local stress status when the fractures occur is the main controlling factor of fracture geometry.

As most of the first-hand data is not available, the analyses in this section are mainly based on the information collected from the published investigations and open documents. The characteristics of the fracture in Horn River shale is obtained by the geological and mechanical analyses. Based on these characteristics, an orthorhombic model is defined to simultaneously represent the fabric anisotropy and the fracture-induced anisotropy in shale.

4.2.1 Fracture stratigraphy

Mechanically, the fracability of rock depends on its strength under the shear or tensile loading. Different mineral compositions of rock may constitute mechanically distinct intervals. Thus, natural or induced fractures usually show a stratigraphic distribution due to the mechanical stratigraphy (Laubach et al., 2009; Gale et al., 2014). High fraction of clay mineral can increase the ductile creep of shale and reduce the brittle strength with regarding to shear and tensile failure (Sone and Zoback, 2013b), while in contrast quartz- and carbonate-rich shales have much higher brittle strength.

As described in the previous chapter, the shale gas reservoir (Muskwa and Upper Otter Park formations) in Horn River basin has extremely high fraction of quartz (up to 87%) and low clay content, whereas the neighboring shale formations (Fort Simpson and Lower Otter Park formations) are characterized by high clay content (average 70%), low quartz content and minor carbonate (see Figure 3.3). Figure 4.1 shows the sonic

logs and the calculated Young's modulus, Poisson's ratio and brittleness index of Horn River shale. We can see that the mineral compositions, especially different portions of softer and stiffer components, have strong impact on the mechanical properties of shale. The mechanical stratigraphy revealed by well logs can remarkably influence the occurrence of natural fractures and hydraulically induced fractures. As expected, the upper and lower clay-rich shale formations exhibit much lower brittle strength and higher ductile properties. The quartz-rich shale formation show much higher Young's modulus and brittleness index, which means a high possibility of fracture occurrence.

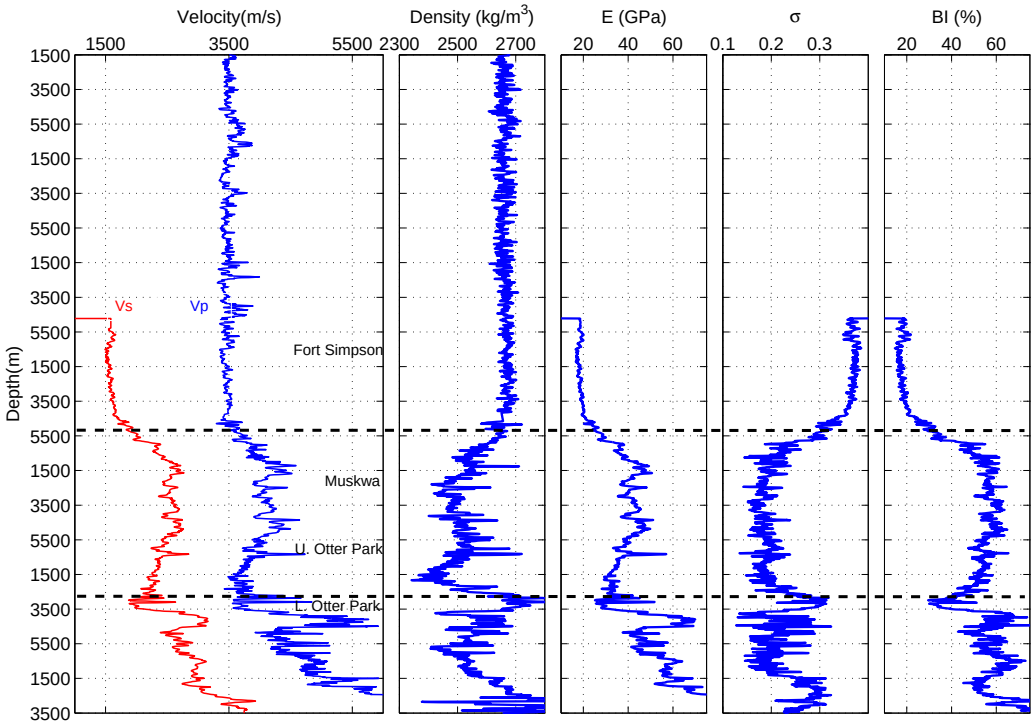

Figure 4.1: Sonic logs and the calculated Young's modulus, Poisson's ratio and Brittleness Index of Horn River shales.

4.2.2 Fracture geometry

Fracture geometry is usually described by fracture orientation, dipping-angle, fracture length, fracture height, spatial arrangement (fracture density) and so on. The knowledge of fracture geometry mostly comes from the observations of outcrops, cores and image logs. Since the subsurface sampling in borehole is inherently limited in space, cores and image logs can only capture the fractures of small scales and a few larger ones intersecting the borehole. The natural fractures of meter scale which are most important for reservoir characterization and mechanical modeling can only be measured in outcrops as the analogs for subsurface fractures. As a result, the site-specific mea-

surements of fracture geometry are inadequate, especially for fracture length, fracture height and fracture density. However, the orientations and dipping angles of fractures which are less scale-dependent can be accurately determined.

Gale et al. (2014) show that the aligned vertical or sub-vertical natural fractures are all observed in the cores and outcrops of shale from 18 shale plays, and state that they are the most important and common natural fracture groups in shale. Such fractures with high angle to bedding are commonly recognized as the product of hydrofracturing process. When the fluid pressure in pore space, either exerted by fluid injection or the internal fluid production, exceeds the confining stress plus the tensile strength of rock, an extensional or shear failure occurs (Cosgrove, 1998). If the failure occurs at a relatively shallow depth in the crust where the stress condition satisfying $(\sigma_1 - \sigma_3) < 4T$, the vertical extensional fractures open against the minimum horizontal stress σ_3 (Figure 4.2a); if the failure occurs at a larger depth where $(\sigma_1 - \sigma_3) > 4T$, shear failure occurs (Figure 4.2b). Here T is the tensile strength of the rock. As Crampin and Atkinson (1985) suggest, such aligned vertical natural fractures are widespread in hydrocarbon reservoirs. Based on the extensive investigations of different shale samples and the general mechanical analysis, the fractures in Horn River shale are assumed to have vertical planes perpendicular to the bedding-parallel fabric.

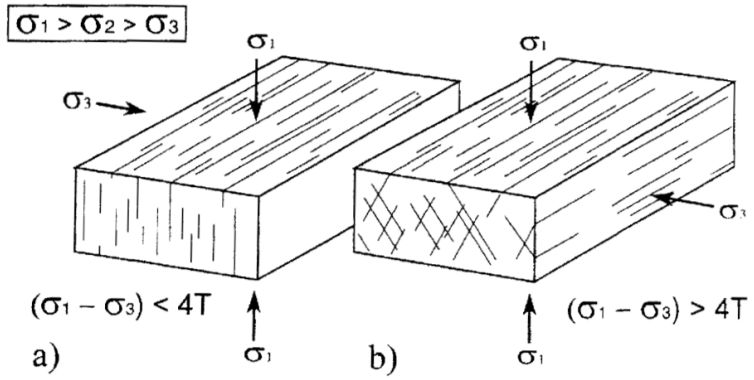

Figure 4.2: Fracture patterns and the corresponding stress conditions in hydrofracturing process (After Cosgrove, 1998).

According to the fracture mechanisms expressed earlier, a fracture opens more easily in the direction of minimum horizontal stress and propagates along the maximum horizontal stress. In the current world stress map, we can see that the average direction of maximum horizontal stress in Horn River Basin strikes NE to SW direction (see Figure 4.3), which is also the perforation direction in hydraulic fracturing treatment. The core and image logs data from a neighboring survey also indicate that the dominant fracture set is NE-SW trending, which is aligned with the current maximum horizontal stress (Rogers et al., 2010). However, one should be aware that the orientation of dominant fracture set does not necessarily coincide with the current maximum horizontal stress because the regional stress may have been rotated after the fracture occurrence.

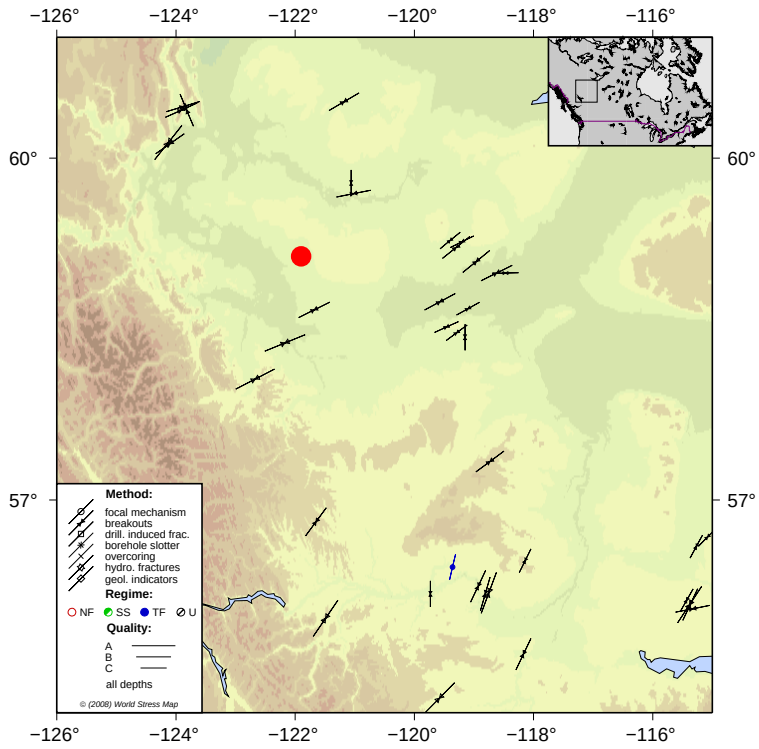

Figure 4.3: The current maximum horizontal stress map in the area of Horn River Basin (Heidbach et al., 2008). Red dot represents the approximate location of the operating site.

4.2.3 Vertically fractured TI model

Although the core data and image logs are not available to us, the characteristics of the fractures in Horn River shale are obtained from the geological and mechanical analyses. The fractures in Horn River shale mainly exist within the quartz-rich shale formation rather than the neighboring clay-rich shale formations. The fracture planes are assumed to be perpendicular to the bedding-parallel fabric. The dominant fracture set strikes NE to SW and is parallel to the current maximum horizontal stress. Based on these characteristics, a subset of orthorhombic model, which is so-called vertically fractured TI (VFTI) model, is introduced to describe the combination of vertical fractures and horizontal fabric laminations in shale (Schoenberg and Helbig, 1997) (see Figure 4.4). The VFTI model simultaneously represents the fabric anisotropy and the fracture-induced anisotropy of shale, the former of which has been obtained in the previous chapter. The phase velocities of P-, S1- and S2-waves in a homogeneous VFTI model are illustrated in Figure 1.2. We can see that the seismic signatures are symmetric for each octant in the 3-D coordinate system. An azimuthal anisotropy can be observed in the seismic response.

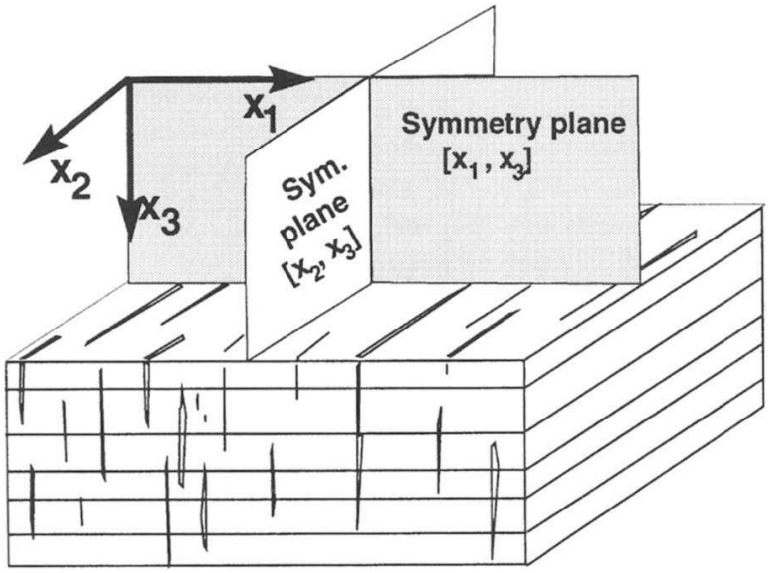

Figure 4.4: Sketch of the vertically fractured TI model (After Rüger, 1998).

4.3 Parameterization of vertically fractured TI media

Vertically fractured TI media is an important subset of orthorhombic media because it is associated with two most common structures in subsurface (i.e., the horizontal laminations and the vertical fractures). As a general orthorhombic media, the VFTI media is described by nine independent stiffness coefficients. Since the stiffness coefficient is defined as a fundamental parameter only describing the stress-strain relationships, it cannot directly reflect the physical details or the seismic responses of subsurface media. Several equivalent manners of representing orthorhombic media or fractured media have been introduced in recent decades from the point of view of effective media or seismic response. In this section, three manners are compared from the perspectives of seismic inversion and the one based on Schoenberg's theory is used in this study.

To simulate the real fractured media, a physically sophisticated effective model is proposed by Hudson (1981). The effective model is composed of matrix material and distributed cracks, and is described by parameters of clear physical meaning, including the background elasticity, crack density, crack radius and aspect ratio, fluid inclusions and so on. This makes it possible to compute the velocity anisotropy, attenuation and other wave behaviors in a particularly defined fractured media. However, some of the parameters needed in this model are difficult to be measured in realistic rocks or be detectable in seismic frequency band. Furthermore, the large number of parameters is an almost insurmountable obstacle in seismic inversion. Therefore, Hudson's model is mainly used in the theoretical and physical modeling in laboratory.

To connect the orthorhombic media directly with seismic signatures, Tsvankin (1997) introduces a Thomsen-style notation for orthorhombic media, which consists of seven extended Thomsen parameters and two vertical velocities of P- and S-wave,

$$\begin{array}{cccc} V_{P0} & V_{S0} & & \\ \varepsilon^{(1)} & \delta^{(1)} & \gamma^{(1)} & \\ \varepsilon^{(2)} & \delta^{(2)} & \gamma^{(2)} & \delta^{(3)} \end{array}$$

Like the original Thomsen parameters, the extended Thomsen parameters reflect the variations of phase velocities in different symmetry planes. Kinematic signatures of a specific wave can be simply expressed by the individual or a combination of extended Thomsen parameters. However, Thomsen-style parameters are dimensionless and have no physical meanings which can explicitly describe the mechanisms of elastic anisotropy. When more than one mechanisms of elastic anisotropy are involved like in the VFTI model, it is difficult to represent a specific mechanism intuitively by these parameters. Additionally, since the extended Thomsen parameters are not commonly used in theoretical modeling and experimental measurements of fractured media, the prior knowledge of these parameters is not convenient to be obtained.

In most seismic applications, it is not necessary to know the physical details of fracture, but the effective parameters reflecting the overall properties of the fractured media. Under the assumption of linear-slip condition, Schoenberg (1980) proposed to use the normal and tangential compliance to describe the effective elastic properties of fractures. The stiffness of the fractured media is then obtained by imposing the excess compliance induced by fractures on the background media (Schoenberg and Sayers, 1995). In such manner, only two more parameters for one fracture set are needed to compute the elastic properties of the effective media without considering any physical details of fractures. Thus, the elastic stiffness of VFTI model as shown in Figure 4.4 can be expressed as (Schoenberg and Helbig, 1997)

$$\mathbf{C}_{\text{VFTI}}^{-1} = \mathbf{C}_{\text{TI}}^{-1} + \mathbf{C}_{\text{VF}}^{-1} \tag{4.1}$$

where $\mathbf{C}_{\text{TI}}$ is the stiffness matrix of the background TI media, and $\mathbf{C}_{\text{VF}}$ is the stiffness matrix pertaining to the extra fracture set. By rotating the fracture orientation to the normal of x_1 axis in Figure 4.4, $\mathbf{C}_{\text{VF}}^{-1}$ has the form as

$$\begin{pmatrix} Z_N & 0 & 0 & 0 & 0 & 0 \\ 0 & 0 & 0 & 0 & 0 & 0 \\ 0 & 0 & 0 & 0 & 0 & 0 \\ 0 & 0 & 0 & 0 & 0 & 0 \\ 0 & 0 & 0 & 0 & Z_V & 0 \\ 0 & 0 & 0 & 0 & 0 & Z_H \end{pmatrix} \tag{4.2}$$

where Z_N is the normal compliance, Z_V and Z_H are the tangential compliance in horizontal and vertical directions. Z_H and Z_V are usually assumed to be equal with each

other and both are expressed as Z_T. Therefore, only seven independent parameters, five of which are the background TI moduli and two are the effective fracture compliance, are needed to describe the VFTI model defined in our study. Using this method, the VFTI media can be decomposed into the background TI media and the vertical fracture set, which makes it possible to independently estimate the background transverse isotropy and the fracture-induced anisotropy using different inversion strategies. Furthermore, the fracture compliance has clear physical meaning and can be modeled theoretically and measured in field or laboratory, which provide the prior knowledge and physical constrains for the estimation of fracture compliance.

4.4 Rock physics constraints on Z_N and Z_T

In theory, the fracture compliance can be expressed explicitly in terms of physical parameters for different fracture models (e.g. Liu et al., 2000; Sayers and Kachanov, 1995). It can also be measured directly in laboratory and field with the same facility as for stiffness (e.g. Sayers, 1999; Lubbe et al., 2008; Hobday and Worthington, 2012; Verdon and Wuestefeld, 2013), although the field measurements are sparse. Theoretical modeling and experimental measurements provide physical constraints for the estimation of fracture compliance. One of the constraints is the normal to tangential fracture compliance ratio (Z_N/Z_T). The Z_N/Z_T ratio is sensitive to the fluid fill and is also influenced by the elasticity of host rock and the internal architecture of the fracture. Another physical constraint on Z_N and Z_T is the magnitude of fracture compliance, which in principle depends on the fracture scales.

4.4.1 Normal to tangential fracture compliance ratio

Theoretical modeling and experimental measurements show that fractures filled with fluid have much lower Z_N/Z_T than the dry or gas-saturated fractures. Considering the fracture fills, there are two extreme cases: (a) completely dry or gas-saturated fracture; (b) hydraulically isolated fractures filled with incompressible fluid.

For the dry fractures embedded in the isotropic media, Sayers and Kachanov (1995) present the expressions of Z_N/Z_T for the open penny-shaped crack model (Hudson's model, see Hudson, 1981) and the partially contacted fracture model (White's model, see White, 1983) as

$$\frac{Z_N}{Z_T} = 1 - \frac{v}{2} \tag{4.3}$$

$$\frac{Z_N}{Z_T} = \frac{1 - v}{1 - v/2} \tag{4.4}$$

where v is the Poisson's ratio of host rock. The different expressions of Z_N/Z_T for these two models imply the influences of different internal architectures of fracture.

Since the Poisson's ratio approximately ranges from 0.1 to 0.25 for typical rocks (see Worthington, 2008), it can be anticipated that

$$\frac{Z_N}{Z_T} \approx 1 \tag{4.5}$$

for both Hudson's and White's fracture models.

For the hydraulically isolated fractures filled with incompressible fluid, a qualitative analysis can be conducted based on the general mechanical principles. The bulk modulus across the fracture is not reduced because the fluid is incompressible, which means that the excess normal fracture compliance is zero ($Z_N = 0$). If the viscosity of fluid is disregarded, the tangential fracture compliance tends to be unchanged in comparison with dry fracture given that there is no shear resistance in fluid. Therefore,

$$\frac{Z_N}{Z_T} \to 0 \tag{4.6}$$

is anticipated for this extreme case. Quantitative analysis is also conducted by Liu et al. (2000) for Hudson's and White's fracture models, which shows that Z_N/Z_T decreases as the bulk modulus of fracture infill (λ_f) increasing and tends to be zero in the rate of λ_f^{-1}.

For the general cases, the fracture is usually saturated or partially saturated with compressible or viscous fluid, and the internal surfaces of fracture are rough and partially contacted. Then, the Z_N/Z_T should be within the range defined by two extreme cases,

$$0 < \frac{Z_N}{Z_T} \leq D \approx 1 \tag{4.7}$$

where D represents the limit of Z_N/Z_T for the dry or gas saturated fractures.

Compared with other elastic properties, the measurements of fracture compliance in macroscopic scale are scarce. Figure 4.5 and Table 4.1 list the typical published laboratory and field measurements of Z_N/Z_T. Except a few measurements of fracture compliance in macroscopic scale (see Lubbe et al., 2008; Hobday and Worthington, 2012; Verdon and Wuestefeld, 2013, etc), most measurements only determine the equivalent compliance of grain contact and fabric discontinuity (see Sayers, 1999; Verdon et al., 2008, etc) or synthetic plate contact (see Hsu and Schoenberg, 1993; Far et al., 2014). The measured Z_N/Z_T are well predicted by theoretical modeling, within the range of $0 \sim 1$. However, the observations of Z_N/Z_T slightly larger than 1 or up to 2 do exist, which means that the theoretical model may not cover all possible realistic cases. As the two extreme cases indicate, all the wet samples display much lower Z_N/Z_T than the coupled dry samples due to the presence of fluid within the discontinuities of media.

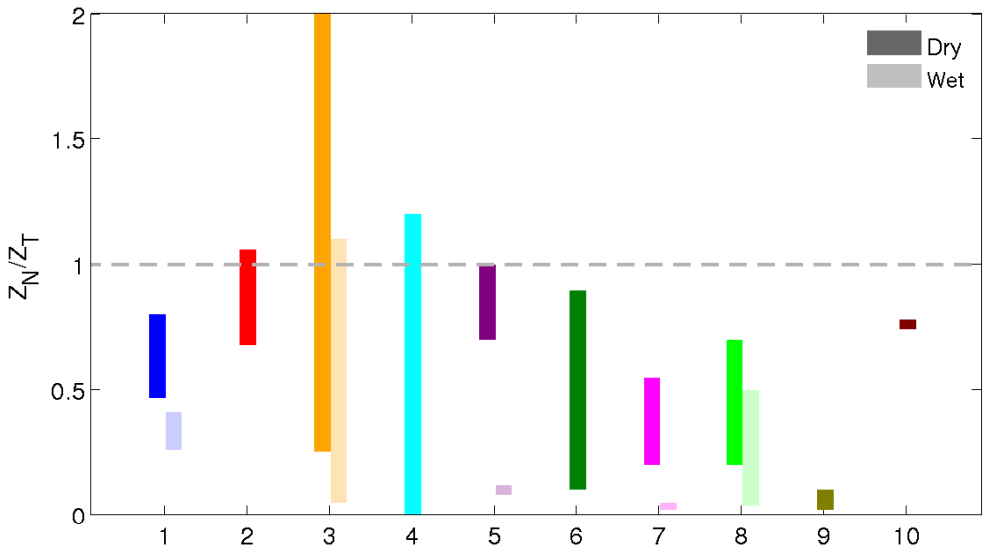

Figure 4.5: Typical published laboratory and field measurements of Z_N/Z_T. For each group of measurements, dark bars represent the dry samples and shallow bars represent the coupled wet samples. Group index is the same as Table 4.1. Modified from Verdon and Wuestefeld (2013).

Table 4.1: Typical published laboratory and field measurements of Z_N/Z_T.

No.	Reference	Frequancy	Sample	Crack or Fracture	Saturation	ZN/ZT
1	Sayers (1999)	Ultrasonic	Shales	Contacts between clay particles	Dry	0.47-0.80
					Water	0.26-0.41
2	Verdon et al. (2008)	Ultrasonic	Sandstone	Contacts between mica fabrics	Dry	0.68-1.06
3	Sayers & Han (2002)	Ultrasonic	Sandstone	Grain-boundary contacts	Dry	0.25-2.00
					Water	0.05-1.10
4	MacBeth and Schuett (2007)	Ultrasonic	Tight sandstone	Grain-boundary contacts	Dry	0-1.20
5	Hsu & Schoenberg (1993)	Ultrasonic	Synthetic media	Contacts between Lucite plates	Dry	0.70-1.0
					Honey	0.10
6	Far et al. (2014)	Ultrasonic	Synthetic media	Contacts between Plexiglass plates	Dry	0.10-0.90
7	Lubbe et al. (2008)	Ultrasonic	Limestone	Artificial fracture by resembling two cuts	Dry	0.20-0.55
					Honey	0.02-0.05
8	Pyrak-Nolte et al. (1990)	Ultrasonic	Quartz monzonite	Natural fracture in core scale	Dry	0.20-0.70
					Water	0.04-0.50
9	Hobday & Worthington (2012)	Seismic	Sandstone outcrop	Natural fracture in meter scale	Water	<0.10
10	Verdon et al. (2013)	Microseismic	Tight sandstone	Natural or induced fracture in meter scale	Gas	0.74-0.78

4.4.2 Magnitude of fracture compliance

As presented in Sayers and Kachanov (1995) and Liu et al. (2000), the expressions of fracture compliance Z_N and Z_T both have positive terms of fracture radius in the numerator part. In principle, the magnitude of fracture compliance should increase with the fracture scale.

Worthington (2008) compared the magnitude of fracture compliance measured in various scale. To extend his analysis, more published data are collected from ultrasonic experiments and field measurements of microseismic and outcrop-seismic scale (see Figure 4.6). We can see that the value of fracture compliance range over several orders of magnitude for different fracture scales. Although no quantitative relationship can be extracted, the increasing order of magnitude of fracture compliance along with the fracture size scale is clearly observed.

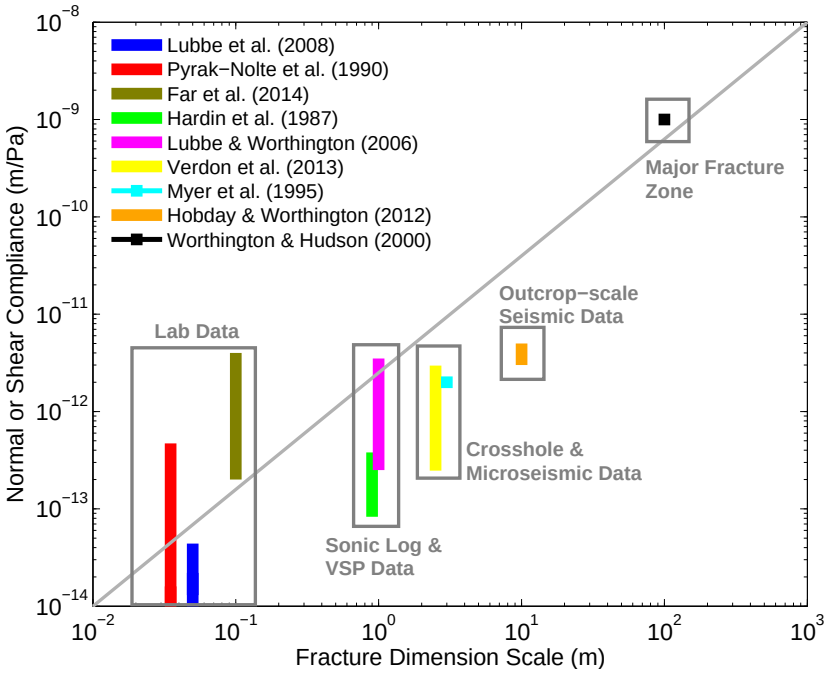

Figure 4.6: Measurements of the fracture compliance in different scales. Modified from Worthington (2008).

The vertical axis in Figure 4.6 is the compliance of an individual fracture with the physical unit of mPa^{-1}. The fracture compliance measured in this study and most field experiments is the overall effective compliance of a set of parallel fractures embedded in the host rock, which has the physical unit of Pa^{-1}. The effective fracture compliance Z can be converted into the individual fracture compliance B according to the relationship (Hobday and Worthington, 2012)

$$B = Zh \tag{4.8}$$

where h is the average spacing of the fractures and has the unit of meter.

4.5 Methodology

Based on the geological analysis in Section 4.2, the fractures in Horn River shale only occur within the quartz-rich shale formation of high brittleness, rather than the neighboring clay-rich shale formations. The shale formation containing fractures is represented by the vertical fractured TI model (see Figure 4.4). According to Schoenberg's theory, the VFTI model is decomposed into the background VTI model and the vertical fractures, the former of which representing the fabric anisotropy of shale has been obtained in the previous chapter (see Figure 3.11). The elastic properties of fractures are effectively described by the normal and tangential fracture compliance (see Section 4.3). Considering the limited resolution of microseismic data, the effective fracture compliance within the layer is assumed to be homogeneous. Then, only two parameters (Z_N and Z_T) remain unknown for the quartz-rich shale formation. By taking the optimal VTI model from Figure 3.11 in the previous chapter, an integrated anisotropic velocity model for Horn River shales is presented in Figure 4.7. The anisotropic ray tracing is performed in this model to calculate the synthesized arrival-times which are compared with the observed arrival-times to find the optimal fracture compliance.

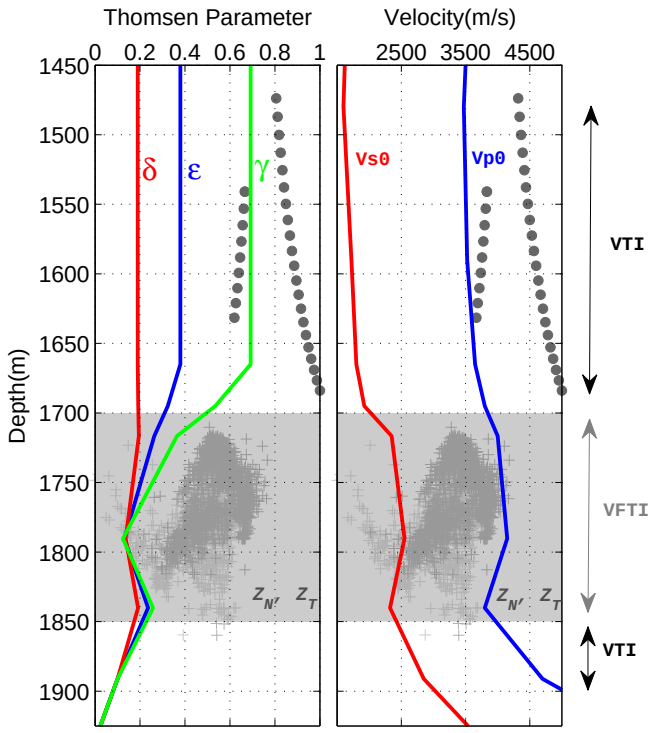

Figure 4.7: The integrated anisotropic velocity model consisting of the optimal VTI model from Chapter 3 and the homogeneous distributions of fracture compliance Z_N and Z_T within the quartz-rich shale formation of high brittleness. Receiver arrays and event clouds are projected on the depth axis with compressed lateral scale.

Since there are only two unknowns for one fracture set, it is possible to perform a global search for the optimal fracture compliance Z_N and Z_T which produce the minimum time misfits. As the searching space is very limited, a simple grid search is adequate for the computation. Theoretical modeling and experimental measurements of fracture compliance provide the physical constraints for the search. The magnitude of fracture compliance summarized in Figure 4.6 is used to define the searching range. In this study, the range is defined from $1.0\times10^{-13}mPa^{-1}$ to $1.0\times10^{-11}mPa^{-1}$, which cover the crosshole and microseismic scales in Figure 4.6. To connect the individual fracture compliance in Figure 4.6 and the effective fracture compliance measured in this study, the average fracture spacing in Equation 4.8 is assumed to be 1 meter, as the core and image logs of the target formations are not available to us. The normal to tangential fracture compliance ratio Z_N/Z_T is used as a quality control. As discussed in Section 4.4.1, the Z_N/Z_T ratio should be less than or slightly larger than 1. Any solutions of Z_N and Z_T with $Z_N/Z_T \gg 1$ should be dismissed. After the optimization of Z_N and Z_T, if the travel-time misfit is reduced significantly, the locations of microseismic events should be updated using the new velocity model and an iterative search for Z_N and Z_T should be performed.

4.6 Microseismic dataset

The microseismic dataset used in this chapter is the same as in the previous chapter, which is recorded by two the downhole arrays in Horn River Basin, Northeast BC, Canada (see Figure 3.8). To minimizing the uncertainties, the selected events of high signal-to-noise ratio and three perforation shots are used for the optimization of fracture-induced anisotropy within the specified layer of high brittleness as indicated.

Since the strongest seismic response of an aligned vertical fracture set is the azimuthal anisotropy in the horizontal symmetry plane, a perfect way of measuring the fracture-induced anisotropy in VFTI model is to deploy the receiver arrays in different azimuth at the same depth with the fracture set. However, as shown in Figure 3.8, two downhole arrays in the monitoring system of this study are both deployed above the target formation. In such situation, seismic responses of the vertical fracture set can become weaker than the response of the horizontal fabric laminations. The polarization analyses also show that the dominant polarizations of SH-wave are within a near horizontal plane, while the polarizations of P- and SV-waves are within a near vertical plane (see Figure 3.10). Recalling the seismic responses of transversely isotropic model and orthorhombic model described in Section 1.2, the polarization analyses further indicate the fact that seismic responses in the monitoring system of this study are dominated by the vertical transverse isotropy rather than by the fracture-induced anisotropy. The time misfits and event locations are probably not sensitive to the fracture-induced anisotropy defined only within the quartz-rich reservoir.

As the optimal vertical transverse isotropy has been obtained in Chapter 3, the fracture-induced anisotropy (i.e., the fracture compliance) will be extracted from the remaining data residual. The imperfect configuration may introduce uncertainties into the estimation of the fracture compliance.

4.7 Results and discussion

Figure 4.8 maps the calculated time misfits for each Z_N and Z_T within the searching range in logarithmic coordinates. The overlapped gray lines are the contours of Z_N/Z_T. The blank squares represent the dismissed solutions of Z_N and Z_T due to too large Z_N/Z_T. We can see that a minimum point of time misfit does exist within the defined searching range, which corresponds to $Z_N \approx 2.5 \times 10^{-12} mPa^{-1}$ and $Z_T \approx 1 \times 10^{-12} mPa^{-1}$. The optimal Z_N and Z_T have the same order of magnitude as other measurements in the crosshole and microseismic scale (see Figure 4.9). However, as the fracture size is unknown, we cannot figure out the x-coordinate to plot the bar like other studies. The normal to tangential compliance ratio Z_N/Z_T corresponding to the minimum point is about 2.5, which is a bit larger than the theoretical modeling and experimental measurements. Given that the target is gas-bearing shale, the Z_N/Z_T ratio corresponds to the extreme case of dry or gas saturated fractures.

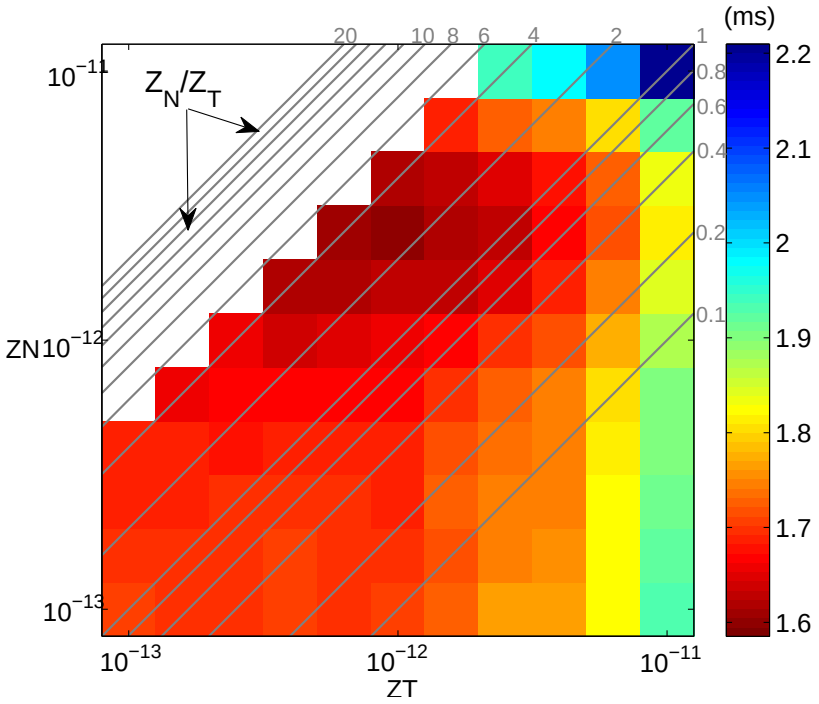

Figure 4.8: Grid searching for the optimal ZN and ZT. The overlapped gray lines are Z_N/Z_T contours.

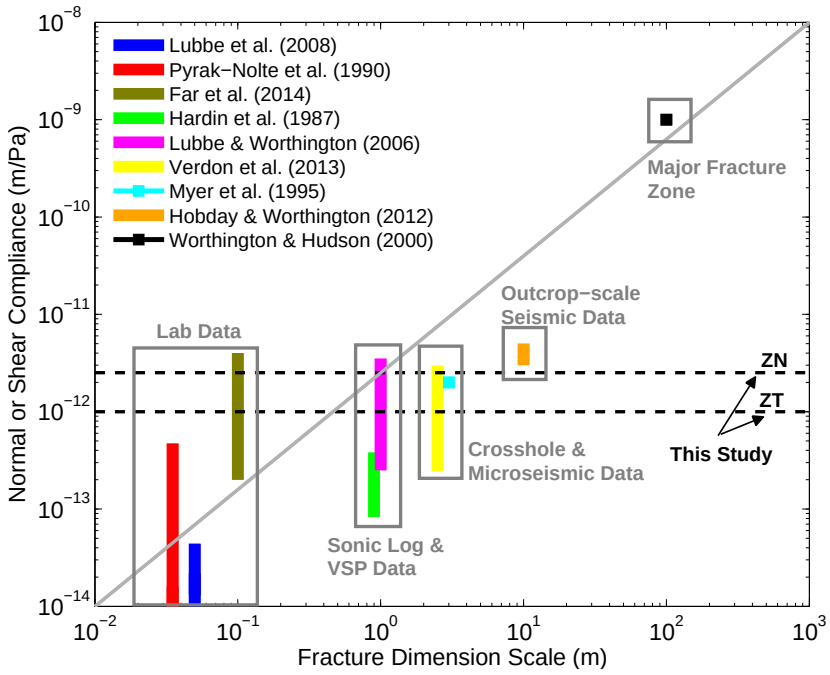

Figure 4.9: Comparison of the fracture compliance measured in different scales.

In Figure 4.8, the bottom-left corner corresponds to the case of extremely low fracture compliance which means few fractures in the media. We can see that the time misfits descend from the bottom-left corner to the minimum point in an extremely slow rate and the total decrease of time misfit from the fracture-free point to the optimal-fracture point is less than 0.1ms. The event locations are also updated using the optimal Z_N and Z_T and the improvement is extremely small compared with the locations using the optimal VTI model obtained in the previous chapter. As discussed in Section 4.6, the time misfits and event locations are not sensitive to the fracture-induced anisotropy because, in the downhole monitoring system of this study, seismic responses of the vertical fracture set in the VFTI model are much weaker than the responses of horizontal fabric laminations. The imperfect configuration introduces uncertainties into the optimization of Z_N and Z_T as shown in Figure 4.8.

Another thing to be concerned about is that the theoretical expressions of Z_N/Z_T (Equation 4.3$\sim$4.4) are based on the isotropic background media. Shale intrinsically exhibits transverse isotropy and shows different mechanical properties in the vertical and horizontal directions. Although most of the experimental measurements of the fracture compliance in shale samples are consistent with the theoretical modeling using the isotropic background media, the theoretical expressions of Z_N and Z_T for the fractures in the TI background media might be different. Two tangential fracture compliances in the horizontal and vertical directions (Z_H and Z_V) are probably no longer equal with each other and should be estimated respectively.

4.8 Conclusion

In this chapter, the geology- and rock physics-oriented approach is further applied to the same downhole microseismic dataset to investigate the fracture-induced anisotropy in Horn River shale. The occurrence of fractures in Horn River shale is controlled by the mechanical stratigraphy resulting from different mineral compositions of shales. The fractures mainly exist within the quartz-rich shale formation rather than the neighboring clay-rich shale formations. The fracture planes are assumed to be perpendicular to the bedding-parallel lamination according to the general mechanical analysis and an extensive observations of shale samples from different plays. The dominant fracture set is NE-SW trending, which is parallel to the current maximum horizontal stress in Horn River Basin. The shale formation containing vertical fractures is represented by the vertical fractured TI (VFTI) model. According to Schoenberg's theory, the VFTI media is decomposed into the background TI media and the vertical fractures, the former of which representing the fabric anisotropy of shale has been obtained in the previous chapter. The effective elastic properties of fractures are described by the normal and tangential fracture compliance without considering the physical details of fractures.

The fracture compliance directly reflects the mechanical weakness of the fracture being as a discontinuity in rock, regardless of the shape, architecture and fluid fills of fracture. It can be used conveniently to construct the effective fractured media in the velocity model inversion. With clear physical meaning and physical dimension, the fracture compliance can be modeled theoretically and measured in laboratory or field, which provide the prior knowledge and physical constraints for the optimization. The magnitude of fracture compliance generally increases with the fracture scale. The normal to tangential fracture compliance ratio (Z_N/Z_T) is sensitive to the fluid fills and ranges approximately from 0 to a value equaling or slightly larger than 1.

A grid searching optimization is implemented to find the optimal Z_N and Z_T which produce the minimum time misfit. The magnitudes of Z_N and Z_T define the possible searching range and the Z_N/Z_T ratio is used as a quality control. The optimized Z_N and Z_T have the same order of magnitude as other measurements in the crosshole and microseismic scale. The Z_N/Z_T ratio corresponds to the extreme cases of dry or gas saturated fractures. The improvements of time misfit and event locations are extremely small compared with the results using the optimal VTI model obtained in the previous chapter. This indicates that, in the downhole monitoring system of this study, seismic responses of the vertical fracture set are much weaker than the responses of horizontal fabric laminations. The imperfect configuration introduces uncertainties into the optimization of Z_N and Z_T.

Chapter 5

Conclusions and outlook

The aim of this thesis was to develop a practical approach to constructing anisotropic velocity model for unconventional reservoirs using downhole microseismic datasets. This approach was designed to be geology- and rock physics-oriented. The working procedure of the approach started by addressing the geological mechanisms of anisotropy. A priori knowledge of anisotropy was obtained by integrating the geological information and rock physics studies, which served as constraints on microseismic inversion. The anisotropic velocity model obtained by this approach reflected the heterogeneity of anisotropic parameters and covered the common anisotropic symmetries of most importance in seismic exploration and reservoir characterization. The optimal anisotropic velocity model not only minimized the data misfit, but also was reasonable from the perspectives of geology and rock physics. The results derived from downhole microseismic dataset were comparable with laboratory experiments, which demonstrated the possible contributions of downhole microseismic monitoring, as a quasi in-situ experiment, to a better understanding of subsurface anisotropy beyond the laboratory.

Considering a limited spatial scale of microseismic monitoring and the sedimentary background of unconventional reservoirs, a layered velocity model was used to reduce the complexity of the inversion problem. Transverse isotropy caused by the bedding-parallel fabric was defined by Thomsen parameters in each layer. The lateral heterogeneities within the layers were dismissed, while the vertical gradients of transverse isotropic parameters were taking into account. The fracture-induced anisotropy was only defined in a specific layer of high brittleness and was characterized by the normal and tangential fracture compliance. Since the approach used the arrival-time of seismic waves recorded by sensor arrays, an anisotropic ray-tracing algorithm was modified to calculate the synthesized travel-time. Parallel computing was employed to accelerate the ray-tracing program. The inherent singularity problems in the ray-tracing method were probed and illustrated. Numerical strategies were proposed to fix these problems. Two nonlinear inversion methods were involved in this approach to determine different components of anisotropy velocity model. The multi-layer TI

media was inverted by an iterative gradient-based optimization (the Gauss-Newton method). The fracture-induced anisotropy characterized only by two parameters was obtained by a global search method. Besides, the issues of computing triggering time (T_0) was analyzed theoretically and illustrated with examples. When the configuration of microseismic monitoring system has limited aperture or multi-waves are used to optimize the velocity model, the conventional way of computing T_0 is a possible source of uncertainties in the velocity model inversion and event locations. The approach developed in this study was partially applied to a completed project of microseismic monitoring in a coalbed methane reservoir to verify the capability of the iterative gradient-based inversion for anisotropic velocity model and to illustrate the T_0 issue in the configuration of limited aperture. Then, the approach was fully applied to the downhole microseismic dataset from Horn River Basin in Canada to investigate the fabric anisotropy and fracture-induced anisotropy of shale.

The fabric anisotropy of shale is caused by the alignment and lamination of the low-aspect-ratio and compliant particles, such as clay and kerogen, and is usually represented by a transversely isotropic model. Laboratory experiments show that, at the core scale, the degree of fabric anisotropy strongly depends on the contents of clay and kerogen. The existence of quartz can prevent and interrupt the alignment and lamination of fabric and consequently weaken the fabric anisotropy of shale. In Horn River basin, the geological analyses show that the mineral compositions of gas-bearing shale is dominated by quartz content (up to 87%), while the overlying shale serving as the fracture barrier is clay-rich (average 70%). By integrating the geological information and experimental studies, the fabric anisotropy can be initially estimated for Horn River shale. This preliminary model completely extracted from a priori knowledge is used as the initial model in further optimization. The fabric anisotropy of shale derived from downhole microseismic dataset is consistent with laboratory measurements. As expected, the quartz-rich shale gas reservoir exhibits much weaker transverse isotropy than the overlying clay-rich shale. The derived Thomsen parameters ε and γ are well correlated with each other, but not with δ. The optimized VTI model reduces the time misfit remarkably by about 65% compared to the originally provided VTI model. Microseismic events clouds located by the optimized VTI velocity model are shifted to more reasonable positions.

A preferred-oriented fracture set is another important source of shale anisotropy. The occurrence of fractures in Horn River shale is controlled by the mechanical stratigraphy resulting from different mineral compositions. Mechanical analyses show that the fractures in Horn River shales mainly occur in the quartz-rich formation of high brittleness. According to the core analyses and mechanism of fracture growth, the fracture planes are commonly perpendicular to the bedding fabric of shale. The dominant fracture set is NE-SW trending, which is parallel to the current maximum horizontal stress. The elastic behavior of fracture is effectively described by the normal and tangential fracture compliance (i.e., Z_N and Z_T) regardless of physical details.

Theoretical modeling and measurements show, the magnitudes of Z_N and Z_T increase with the fracture dimension scale, and the Z_N/Z_T ratio is sensitive to the fluid fills and has the value less than or slightly larger than 1. These facts were used as physical constraints when estimating the fracture compliance. The magnitudes of Z_N and Z_T defined the possible searching range and the Z_N/Z_T ratio was used as a quality control. A grid searching method was implemented to find the optimal normal and tangential fracture compliance which produced the minimum travel time misfit. The optimized Z_N and Z_T have the same order of magnitude as other measurements in the crosshole and microseismic scale. The Z_N/Z_T ratio corresponds to the extreme cases of dry or gas saturated fractures. The improvements of time misfit and event locations are really small compared with the results using the optimal VTI model. This indicates the fact that, in the downhole monitoring system of this study, seismic responses of the vertical fracture set are much weaker than the responses of horizontal fabric laminations. The imperfect configuration may introduces uncertainties into the optimization of Z_N and Z_T.

Outlook

The application examples in this study have shown the feasibility and validity of geology- and rock physics-oriented approach to constructing the anisotropic velocity model in unconventional reservoirs, and also the potential of downhole microseismic monitoring being as a quasi in-situ experiment to provide new insights into the anisotropy of crustal rock. Nevertheless, there are still some limitations and unaccomplished work in this study.

This approach is initially designed for unconventional oil/gas reservoirs which usually have simple structure and sedimentary background. Thus, a layered model without considering the lateral heterogeneity is used in this study. For microseismic monitoring in complex geological setting, such as in Enhanced Geothermal System, the tilted layers or the presences of faults are possible, and the lateral heterogeneity can be very strong. Then the blocked model or grid-node model might be the better options. This approach only considers the anisotropy caused by the horizontal fabric laminations and a vertical fracture set in Horn River shale formations. In more general geological background, the geometry of fracture set can be much complex, which may result in lower symmetry class of anisotropy. For those situations, the inversion scheme needs to be improved to handle more parameters and complex model geometry.

Basically, this approaches are travel-time based inversion, and a ray-tracing algorithm is used to calculate the synthesized travel-time. In this decade, the waveform-based inversion are more and more developed for reflection seismic or microseismic applications to construct the velocity model, locate the events and derive the source mechanisms. Since the waveform data contains more seismic responses of media prop-

erties, more accurate results are expected. This is of course accompanied by much higher computation costs and more ill-posed inversion problems. For the waveform inversion, an accurate starting model is of crucial important for obtaining a reasonable result. The geological and rock physics constraints can help construct the initial anisotropic model as proposed in this study.

In this study, shale anisotropy derived from the downhole microseismic dataset is qualitatively compared with laboratory or field experiments and theoretical modeling. Unfortunately, no more quantitative analyses are implemented. One of the reasons is that the first-hand geological data around the operating site, such as core data, image logs and stratigraphic setting, are not available to us. Most of the geological analyses in this study are based on the data collected from publications or open documents. Geological input with high uncertainties is not suitable for rock physics modeling. If there are any opportunities, one could conduct an integral study by integrating the downhole microseismic dataset, the first-hand geological data and laboratory measurements of core samples from the same site.

Appendix A

Derivatives of phase velocity with respect to Thomsen parameters and stiffness constants

The derivatives of phase velocities with respect to Thomsen parameters and stiffness constants are derived from the analytical forms of phase velocities as shown by Equation 2.1~2.4.

$$\frac{\partial V_{p,sv}}{\partial V_{p0}} = \frac{1}{2V_{p,sv}F}\left\{V_{p0}F\left(1+2\varepsilon\sin^2\theta\right)\right. \\ \left.\pm\left[V_{p0}\left(V_{p0}^2-V_{s0}^2\right)+\left(4V_{p0}^3-2V_{p0}V_{s0}^2\right)\sin^2\theta\left(2\delta\cos^2\theta-\varepsilon\cos 2\theta\right)+4V_{p0}^3\varepsilon^2\sin^4\theta\right]\right\} \tag{A.1}$$

$$\frac{\partial V_{p,sv}}{\partial V_{s0}} = \frac{V_{s0}F\pm\left[V_{s0}\left(V_{s0}^2-V_{p0}^2\right)-2V_{s0}V_{p0}^2\sin^2\theta\left(2\delta\cos^2\theta-\varepsilon\cos 2\theta\right)\right]}{2V_{p,sv}F} \tag{A.2}$$

$$\frac{\partial V_{sh}}{\partial V_{s0}} = \frac{V_{s0}\left(1+2\gamma\sin^2\theta\right)}{V_{sh}} \tag{A.3}$$

$$\frac{\partial V_{p,sv}}{\partial \varepsilon} = \frac{V_{p0}^2F\sin^2\theta\pm\left[\left(V_{p0}^2V_{s0}^2-V_{p0}^4\right)\sin^2\theta\cos 2\theta+2V_{p0}^4\varepsilon\sin^4\theta\right]}{2V_{p,sv}F} \tag{A.4}$$

$$\frac{\partial V_{p,sv}}{\partial \delta} = \pm\frac{\left(V_{p0}^4-V_{p0}^2V_{s0}^2\right)\sin^2\theta\cos^2\theta}{V_{p,sv}F} \tag{A.5}$$

$$\frac{\partial V_{sh}}{\partial \gamma} = \frac{V_{s0}^2\sin^2\theta}{V_{sh}} \tag{A.6}$$

where

$$F = \sqrt{\left(V_{p0}^2 - V_{s0}^2\right)^2 + 4\left(V_{p0}^4 - V_{p0}^2 V_{s0}^2\right)\sin^2\theta\left(2\delta\cos^2\theta - \varepsilon\cos 2\theta\right) + 4V_{p0}^4\varepsilon^2\sin^4\theta} \tag{A.7}$$

V_p, V_{sv}, V_{sh} are calculated by Equation 2.3~2.4, and θ is the angle between wavefront normal and the vertical symmetry axis.

$$\frac{\partial V_{p,sv}}{\partial c_{33}} = \frac{F\cos^2\theta \mp \left[\left(c_{11} - c_{55}\right)\sin^2\theta\cos^2\theta - \left(c_{33} - c_{55}\right)\cos^4\theta\right]}{4V_{p,sv}\rho F} \tag{A.8}$$

$$\frac{\partial V_{p,sv}}{\partial c_{55}} = \frac{F \pm \left[\left(c_{11} - c_{55}\right)\sin^2\theta\cos 2\theta - \left(c_{33} - c_{55}\right)\cos^2\theta\cos 2\theta + 4\left(c_{13} + c_{55}\right)\sin^2\theta\cos^2\theta\right]}{4V_{p,sv}\rho F} \tag{A.9}$$

$$\frac{\partial V_{p,sv}}{\partial c_{11}} = \frac{F\sin^2\theta \pm \left[\left(c_{11} - c_{55}\right)\sin^4\theta - \left(c_{33} - c_{55}\right)\sin^2\theta\cos^2\theta\right]}{4V_{p,sv}\rho F} \tag{A.10}$$

$$\frac{\partial V_{p,sv}}{\partial c_{13}} = \pm\frac{\left(c_{13} + c_{55}\right)\sin^2\theta\cos^2\theta}{V_{p,sv}\rho F} \tag{A.11}$$

$$\frac{\partial V_{sh}}{\partial c_{66}} = \frac{\sin^2\theta}{2V_{sh}\rho} \tag{A.12}$$

$$\frac{\partial V_{sh}}{\partial c_{55}} = \frac{\cos^2\theta}{2V_{sh}\rho} \tag{A.13}$$

where

$$F = \sqrt{\left[\left(c_{11} - c_{55}\right)\sin^2\theta - \left(c_{33} - c_{55}\right)\cos^2\theta\right]^2 + 4\left(c_{13} + c_{55}\right)^2\sin^2\theta\cos^2\theta} \tag{A.14}$$

V_p, V_{sv}, V_{sh} are calculated by Equation 2.1~2.2, ρ is the density, and θ is the angle between wavefront normal and the vertical symmetry axis.

References

Aki, K. and Richards, P. G. (2002). *Quantitative seismology (2nd Edition)*, volume 1. University Science Books, Sausalito.

BC Ministry of Energy and Mines (2005). Gas shale potential of devonian strata, northeastern british columbia. BC Ministry of Energy and Mines, Oil & Gas Report.

Bleistein, N. (1984). *Mathematical methods for wave phenomena*. Academic Press, Orlando.

Boggs, S. (2011). *Principles of Sedimentology and Stratigraphy (5th Edition)*. Prentice Hall, Upper Saddle River.

Chalmers, G., Ross, D., and Bustin, R. M. (2012). Geological controls on matrix permeability of devonian gas shales in the horn river and liard basins, northeastern british columbia, canada. *International Journal of Coal Geology*, 103(0):120 – 131.

Chapman, C. and Leaney, W. (2012). A new moment-tensor decomposition for seismic events in anisotropic media. *Geophysical Journal International*, 188(1):343–370.

Cosgrove, J. (1998). The role of structural geology in reservoir characterization. *Geological Society, London, Special Publications*, 127(1):1–13.

Crampin, S. and Atkinson, B. K. (1985). Microcracks in the earth's crust. *First Break*, 3(3).

Curtis, C. D., Lipshie, S. R., Oertel, G., and Pearson, M. J. (1980). Clay orientation in some upper carboniferous mudrocks, its relationship to quartz content and some inferences about fissility, porosity and compactional history. *Sedimentology*, 27(3):333–339.

Dahi-Taleghani, A., Olson, J. E., et al. (2011). Numerical modeling of multistranded-hydraulic-fracture propagation: Accounting for the interaction between induced and natural fractures. *SPE journal*, 16(03):575–581.

Duncan, P. M. and Eisner, L. (2010). Reservoir characterization using surface microseismic monitoring. *GEOPHYSICS*, 75(5):75A139–75A146.

Dunphy, R. and Campagna, D. J. (2011). Fractures, elastic moduli & stress: Geological controls on hydraulic fracture geometry in the horn river basin. Expanded abstracts, CSEG CSPG CWLS Convention.

Far, M. E., de Figueiredo, J. J. S., Stewart, R. R., Castagna, J. P., Han, D.-H., and Dyaur, N. (2014). Measurements of seismic anisotropy and fracture compliances in synthetic fractured media. *Geophysical Journal International*.

Fisher, M., Heinze, J., Harris, C., Davidson, B., Wright, C., Dunn, K., et al. (2004). Optimizing horizontal completion techniques in the barnett shale using microseismic fracture mapping. In *SPE Annual Technical Conference and Exhibition*.

Gajewski, D. and Pšencík, I. (1987). Computation of high-frequency seismic wavefields in 3-d laterally inhomogeneous anisotropic media. *Geophysical Journal of the Royal Astronomical Society*, 91(2):383–411.

Gale, J. F., Laubach, S. E., Olson, J. E., Eichhubl, P., and Fall, A. (2014). Natural fractures in shale: A review and new observations. *AAPG Bulletin*, 98(11):2165–2216.

Gale, J. F., Reed, R. M., and Holder, J. (2007). Natural fractures in the barnett shale and their importance for hydraulic fracture treatments. *AAPG bulletin*, 91(4):603–622.

Grechka, V. (2009). *Applications of Seismic Anisotropy in the OIl and Gas Industry*. EAGE Publications.

Grechka, V., Singh, P., and Das, I. (2011). Estimation of effective anisotropy simultaneously with locations of microseismic events. *Geophysics*, 76(6):WC143–WC155.

Grechka, V. and Yaskevich, S. (2013). Inversion of microseismic data for triclinic velocity models. *Geophysical Prospecting*, 61(6):1159–1170.

Grechka, V. and Yaskevich, S. (2014). Azimuthal anisotropy in microseismic monitoring: A bakken case study. *Geophysics*, 79(1):KS1–KS12.

Hall, C. (2000). A comparison of gas shale reservoir properities - haynesville, marcellus, barnett, eagle ford, montney and muskwa. Technical report, 4th Unconventional Gas Technical Forum, BC Ministry of Energy and Mines.

Harris, N. B. and Dong, T. (2013). Characterizing porosity in the horn river shale, northeastern british columbia. Bc ministry of energy and mines, oil & gas report.

Heidbach, O., Tingay, M., Barth, A., Reinecker, J., Kurfeß, D., and Müller, B. (2008). The world stress map database release 2008. *doi:10.1594/GFZ.WSM.Rel2008*.

Helbig, K. (1983). Elliptical anisotropy-its significance and meaning. *Geophysics*, 48(7):825–832.

Hobday, C. and Worthington, M. (2012). Field measurements of normal and shear fracture compliance. *Geophysical Prospecting*, 60(3):488–499.

Hornby, B. E., Schwartz, L. M., and Hudson, J. A. (1994). Anisotropic effective-medium modeling of the elastic properties of shales. *Geophysics*, 59(10):1570–1583.

Hsu, C.-J. and Schoenberg, M. (1993). Elastic waves through a simulated fractured medium. *Geophysics*, 58(7):964–977.

Hudson, J. (1981). Wave speeds and attenuation of elastic waves in material containing cracks. *Geophysical Journal of the Royal Astronomical Society*, 64(1):133–150.

Hummel, N. and Shapiro, S. A. (2012). A hydraulic fracturing case study (i): Estimates of reservoir parameters from hydraulic fracturing induced seismicity. *7^{th} Annual PHASE Report*, pages 155–164.

Johnston, J. E. and Christensen, N. I. (1995). Seismic anisotropy of shales. *Journal of Geophysical Research*, 100(B4):5991–6003.

Jurkevics, A. (1988). Polarization analysis of three-component array data. *Bulletin of the Seismological Society of America*, 78(5):1725–1743.

Laubach, S. E., Olson, J. E., and Gross, M. R. (2009). Mechanical and fracture stratigraphy. *AAPG bulletin*, 93(11):1413–1426.

Li, J., Zhang, H., Rodi, W. L., and Toksoz, M. N. (2013). Joint microseismic location and anisotropic tomography using differential arrival times and differential backazimuths. *Geophysical Journal International*, 195(3):1917–1931.

Liu, E., Hudson, J. A., and Pointer, T. (2000). Equivalent medium representation of fractured rock. *Journal of Geophysical Research*, 105(B2):2981–3000.

Lubbe, R., Sothcott, J., Worthington, M., and McCann, C. (2008). Laboratory estimates of normal and shear fracture compliance. *Geophysical Prospecting*, 56(2):239–247.

MacBeth, C. and Schuett, H. (2007). Stress dependent elastic properties of thermally induced microfractures in aeolian rotliegend sandstone. *Geophysical Prospecting*, 55(3):323–332.

Marquardt, D. W. (1963). An algorithm for least-squares estimation of nonlinear parameters. *Journal of the society for Industrial and Applied Mathematics*, 11(2):431–441.

Mavko, G., Mukerji, T., and Dvorkin, J. (2009). *The rock physics handbook: Tools for seismic analysis of porous media*. Cambridge university press.

Michel, O. J. and Tsvankin, I. (2014). Gradient calculation for waveform inversion of microseismic data in vti media. *Journal of Seismic Exploration*, 23(3):201–217.

Michel, O. J. and Tsvankin, I. (2015). Estimation of microseismic source parameters by 2d anisotropic waveform inversion. *Journal of Seismic Exploration*, 24(4):379–400.

Ness, S., Benteau, R., and Leggitt, S. (2010). Horn River Shales ... Boring and Black? ... or ... Beatifully Complex? Abstracts, GeoCanada - Working with the Earth.

Nicolas, A., Boudier, F., and Boullier, A. (1973). Mechanisms of flow in naturally and experimentally deformed peridotites. *Am. J. Sci*, 273(10):853–876.

Peng, Z. and Ben-Zion, Y. (2004). Systematic analysis of crustal anisotropy along the karadere—düzce branch of the north anatolian fault. *Geophysical Journal International*, 159(1):253–274.

Pyrak-Nolte, L. J., Myer, L. R., and Cook, N. G. (1990). Transmission of seismic waves across single natural fractures. *Journal of Geophysical Research: Solid Earth*, 95(B6):8617–8638.

Reshetnikov, A., Hummel, N., and Shapiro, S. A. (2012a). A hydraulic fracturing case study (iii): Interpretation of new locations and comparative analysis of fracture geometry and fluid transport properties. *7^{th} Annual PHASE Report*, pages 181–188.

Reshetnikov, A., Kummerow, J., and Shapiro, S. A. (2012b). A hydraulic fracturing case study (ii): Location of induced microseismic events using single vertical borehole array. *7^{th} Annual PHASE Report*, pages 165–180.

Rogers, S., Elmo, D., Dunphy, R., Bearinger, D., et al. (2010). Understanding hydraulic fracture geometry and interactions in the horn river basin through dfn and numerical modeling. In *Canadian Unconventional Resources and International Petroleum Conference*.

Ross, D. and Bustin, R. M. (2008). Characterizing the shale gas resource potential of devonian–mississippian strata in the western canada sedimentary basin: Application of an integrated formation evaluation. 92(1):87–125.

Rüger, A. (1998). Variation of p-wave reflectivity with offset and azimuth in anisotropic media. *Geophysics*, 63(3):935–947.

Sayers, C. M. (1999). Stress-dependent seismic anisotropy of shales. *Geophysics*, 64(1):93–98.

Sayers, C. M. (2005). Seismic anisotropy of shales. *Geophysical Prospecting*, 53(5):667–676.

Sayers, C. M. (2013). The effect of kerogen on the elastic anisotropy of organic-rich shales. *Geophysics*, 78(2):D65–D74.

Sayers, C. M. and Han, D.-H. (2002). The effect of pore fluid on the stress-dependent elastic wave velocities in sandstones. *SEG Technical Program Expanded Abstracts 2002*.

Sayers, C. M. and Kachanov, M. (1995). Microcrack-induced elastic wave anisotropy of brittle rocks. *Journal of Geophysical Research*, 100(B3):4149–4156.

Schoenberg, M. (1980). Elastic wave behavior across linear slip interfaces. *The Journal of the Acoustical Society of America*, 68(5):1516–1521.

Schoenberg, M. and Helbig, K. (1997). Orthorhombic media: Modeling elastic wave behavior in a vertically fractured earth. *Geophysics*, 62(6):1954–1974.

Schoenberg, M. and Sayers, C. (1995). Seismic anisotropy of fractured rock. *Geophysics*, 60(1):204–211.

Shapiro, S. A. and Kaselow, A. (2005). Porosity and elastic anisotropy of rocks under tectonic stress and pore-pressure changes. *Geophysics*, 70(5):N27–N38.

Sondergeld, C., Rai, C., Margesson, R., and Whidden, K. (2000). Ultrasonic measurement of anisotropy on the kimmeridge shale. *SEG Technical Program Expanded Abstracts 2000*, pages 1858–1861.

Sone, H. and Zoback, M. D. (2013a). Mechanical properties of shale-gas reservoir rock-part 1: Static and dynamic elastic properties and anisotropy. *Geophysics*, 78(5):D381–D392.

Sone, H. and Zoback, M. D. (2013b). Mechanical properties of shale-gas reservoir rocks—part 2: Ductile creep, brittle strength, and their relation to the elastic modulus. *Geophysics*, 78(5):D393–D402.

Thomsen, L. (1986). Weak elastic anisotropy. *Geophysics*, 51(10):1954–1966.

Thurber, C. H. (1993). *Local earthquake tomography: velocity and Vp/Vs-theroy, in Seismic tomography, Theory and practice: Iyer, H. M. and Hirahara K.* Chapman and Hall, London.

Tsvankin, I. (1997). Anisotropic parameters and p-wave velocity for orthorhombic media. *Geophysics*, 62(4):1292–1309.

Vavryčuk, V. (2001). Ray tracing in anisotropic media with singularities. *Geophysical Journal International*, 145(1):265–276.

Vavryčuk, V. (2003). Generation of triplications in transversely isotropic media. *Physical Review B*, 68(5):054107.

Vavryčuk, V. (2005). Focal mechanisms in anisotropic media. *Geophysical Journal International*, 161(2):334–346.

Vavryčuk, V., Bohnhoff, M., Jechumtálová, Z., Kolář, P., and Šílenỳ, J. (2008). Non-double-couple mechanisms of microearthquakes induced during the 2000 injection experiment at the ktb site, germany: A result of tensile faulting or anisotropy of a rock? *Tectonophysics*, 456(1):74–93.

Červený, V. (2001). *Seismic Ray Theory*. Cambridge University Press, Cambridge.

Verdon, J. P., Angus, D. A., Michael Kendall, J., and Hall, S. A. (2008). The effect of microstructure and nonlinear stress on anisotropic seismic velocities. *Geophysics*, 73(4):D41–D51.

Verdon, J. P. and Kendall, J. (2011). Detection of multiple fracture sets using observations of shear-wave splitting in microseismic data. *Geophysical Prospecting*, 59(4):593–608.

Verdon, J. P., Kendall, J., and Wuestefeld, A. (2009). Imaging fractures and sedimentary fabrics using shear wave splitting measurements made on passive seismic data. *Geophysical Journal International*, 179(2):1245–1254.

Verdon, J. P. and Wuestefeld, A. (2013). Measurement of the normal/tangential fracture compliance ratio (zn/zt) during hydraulic fracture stimulation using s-wave splitting data. *Geophysical Prospecting*, 61:461–475.

Vernik, L. (1994). Hydrocarbon-generation-induced microcracking of source rocks. *Geophysics*, 59(4):555–563.

Vernik, L. and Landis, C. (1996). Elastic anisotropy of source rocks: Implications for hydrocarbon generation and primary migration. *AAPG bulletin*, 80(4):531–544.

Vernik, L. and Liu, X. (1997). Velocity anisotropy in shales: A petrophysical study. *Geophysics*, 62(2):521–532.

Vernik, L. and Nur, A. (1992). Ultrasonic velocity and anisotropy of hydrocarbon source rocks. *Geophysics*, 57(5):727–735.

Wang, Z. (2002). Seismic anisotropy in sedimentary rocks, part 2: Laboratory data. *Geophysics*, 67(5):1423–1440.

Worthington, M. (2008). Interpreting seismic anisotropy in fractured reservoirs. *First Break*, 26(7).

Wuestefeld, A., Kendall, J. M., Verdon, J. P., and van As, A. (2011). In situ monitoring of rock fracturing using shear wave splitting analysis: an example from a mining setting. *Geophysical Journal International*, 187(2):848–860.

Zhang, S. and Karato, S. (1995). Lattice preferred orientation of olivine aggregates deformed in simple shear. *Nature*, 375(6534):774–777.

List of Figures

List of Tables

Curriculum Vitae

For privacy reasons, the CV is not included in the digital version.

Publications

Journal Publications

[1] Yu, C. P. and Shapiro, S. A. (2016). Estimation of shale anisotropy using downhole microseismic dataset: fabric anisotropy. Geophysics. (Submitted)

[2] Yu, C. P. and Shapiro, S. A. (2016). Estimation of shale anisotropy using downhole microseismic dataset: fracture-induced anisotropy. Geophysics. (Submitted)

Expanded Abstracts

[1] Yu, C. P. and Shapiro, S. A. (2015). Rock physics constrained estimation of shale anisotropy for microseismic processing - from VTI to orthorhombic. *Expanded abstracts, EAGE 77th annual meeting and technical exhibition, Madrid.* DOI: 10.3997/2214-4609.201413114

[2] Yu, C. P. and Shapiro, S. A. (2014). Seismic anisotropy of shale: inversion of microseismic data. *SEG Technical Program Expanded Abstracts 2014:2324-2329.* DOI:10.1190/segam2014-1251.1

[3] Yu, C. P., Reshetnikov, A., and Shapiro, S. A. (2013). Simultaneous inversion of anisotropic velocity model and microseismic event location: synthetic and real data examples. *Expanded abstracts, EAGE 75th annual meeting and technical exhibition, London.* DOI: 10.3997/2214-4609.20130407

[4] Yu, C. P., Yu, W. H. and Qu, Z. (2009). Methodology of 3D velocity-variant depth mapping in complex fault-block area. *Expanded abstracts, CPS/SEG International Geophysical Conference and Exposition, Beijing.* DOI:10.1190/1.3603679

Abstracts

[1] Yu, C. P. and Shapiro, S. A. (2014). Orthorhombic velocity model building for microseismic processing with constraints of rock physics and geological setting. *Abstracts, 5th EAGE Passive Seismic Workshop, Lisbon.* DOI: 10.3997/2214-4609.20142175

[2] Yu, C. P., Yu, W. H. and Qu, Z. (2010). Preliminary investigation of integrated inversion of quality factor and interval velocity. *International Workshop on Multiple-scale Geodynamics of Continental Interiors, Wuhan.*

Acknowledgements

Firstly, I would like to express my sincere gratitude to my supervisor Prof. Dr. Serge A. Shapiro for offering me the opportunity to work in Freie Universität Berlin. I greatly appreciate the freedom he has given to me to conduct my research without interference, the encouragement he has always not spared and the constructive suggestions for my work during all the years.

I would like to thank Dr. Anton Reshetnikov for helping me to start the research on the new topic and sharing his knowledge in our collaboration. I would also like to thank Malgorzata Grunenberg and Jonas Folesky for their kind help when I came to this group as a new member. Further I would like to thank Dr. Nicolas Hummel and Dr. Stine Gutjahr for help me formatting and submitting the thesis. Especially, I thank Aurelian Röser for helping me to translate the summary of this thesis. I thank all other colleagues, Jörn Kummerow, Carsten Dinske, Oliver Krüeger, Antonia Oelke, Wasja Bloch and Naoyuki Shimoda for any help in the life and work during all the years.

In addition, I would like to express my appreciation to Prof. Dr. Marco Bohnhoff for reviewing my thesis and to Prof. Dr. Oliver Ritter, Prof. Dr. Timm John and Dr. Anton Reshetnikov for serving on my dissertation committee.

I gratefully acknowledge the Chinese Scholarship Council (CSC) for granting me a four-year scholarship and the PHASE project for funding my research.

Finally, I would like to thank my parents and brother for their support from eight thousands kilometers away and for their understanding of my absence on many important days. A heartfelt thanks is reserved for my wife Yaling Zhu. I would no have been able to complete this work without her company and encouragement during the last four years.